UNIVERSITA' DEGLI STUDI DI PARMA

Dottorato di ricerca

in

Scienza e Tecnologia dei Materiali Innovativi

Ciclo XXVIII

Non linear light-matter interactions and new coupling techniques in silica WGM optical resonators

Coordinatore : Chiar.mo Prof. Enrico Dalcanale

Tutor : Dr. Gualtiero Nunzi Conti

Dottorando : Daniele Farnesi

Aknowledgments

I don't like the fact that only my name appears on the first page of this dissertation. Not one work I have completed during the last years could be possible without the help of the people close to me. I would first like to thank Professor Giancarlo Righini who has supported me during these years and has given me the opportunity to be part of his research group and to live wonderful experiences that have made me grow not only as researcher. I am very grateful to my advisor, Dr. Gualtiero Nunzi Conti, who has been a great mentor and friend to me since we began working together. I have truly learned a lot even beyond the science itself. I would like to send my sincere thanks also to the team, Dr. Silvia Soria, Mr. Franco Cosi and Dr. Andrea Barucci. I have really enjoyed working with them. I would like to express my gratitude to all the other people who have collaborated with me, in particular Dr.Stefano Pelli and Dr.Francesco Chiavaioli. I mustn't forget to thank, Prof.Enrico Dalcanale and Prof.Anna Painelli of University of Parma, for their support especially during my experience at the University of Central Florida. Thanks to Prof. Eric Van Stryland and Prof. David Hagan of CREOL-UCF for have given me the opportunity to work in their wonderful group. Finally, I want to thank my unique family for their support, sacrifice and love. My parents, Oriana and Mario and my brother Edoardo have always give me the encouragement to move forward. I am really lucky to have such a family.

Contents

List of Figures

Chapter 1

Introduction

The study of the effects and phenomena related to the interaction of intense coherent light with matter is the main subject of nonlinear optics. This revolutionary extension of the conventional linear optics was favored by the discovery of laser in 1960 by Maiman. He suceeded in inducing the first stimulated optical output in Ruby crystals [1] and in short time a multitude of gain media was subsequently used, which included helium-neon [2], semiconductor [3], carbon dioxide [4], dyes [5, 6], and excimers [7].

After the birth of the laser, the demonstration of optical second-harmonic generation (1961) [8] was recognized as the first milestone of nonlinear optics. Several other optical frequency mixing effects were sequentially demonstrated within few years. The optical sum-frequency generation [9] and third-harmonic generation in 1962 [10], optical difference-frequency generation in 1963 [11] and optical parametric amplification and oscillation in 1965 [12, 13]. These experimental demonstrations not only verified the validity of nonlinear polarization theories but also opened the door for an alternative approach to generate coherent radiation. The key role of the laser in nonlinear optics can be understood considering the case of Stimulated Raman scattering (SRS). It was discovered 34 years after the papers on spontaneous Raman scattering of Raman [14, 15] and the less famous of Mandelstam [16]. In 1962, SRS

Figure 1.1: Children trying out the Whispering Gallery at St Paul's Cathedral.

was observed, rather accidentlly, by Woodbury and Ng [17] and described by Eckhardt et al.[18]. The properties of SRS have been then reviewed sequentially by Bloembergen in 1967 [19],Kaiser and Maier in 1972 [20], Penzkofer in 1979 [21], and Raymer in 1990 [22].

Since the early days of Maiman's discovery, great attention has been invested in exploiting different kind of optical cavities for laser emission. In 1961, Whispering-gallery-mode (WGM) lasers have been demonstrated by Garret, using a CaF2:Sm(single crystals) sphere with a diameter in the millimeter range [23]. The term "WGM" comes from the Lord Rayleigh's famous paper in which, fifty years early, he detailed the acoustic property of the dome of Saint Paul Cathedral in London, where a whisper at one side can be clearly heard at any place along the gallery (Fig.1.1).

The effect is due to the smooth and curved walls guiding the sound around the periphery of the room with great efficiency. Sound waves taking any other path are dissipated or scattered. A similar effect can lead to the analogous optical behavior in circular shaped dielectrics. When light propagating in a medium of higher refractive index meets the interface with a medium of lower refractive index at an angle of incidence that equals the critical angle,

it will undergo total internal reflection. At the right angle it constructively interferes after a round trip, the light can be trapped and builds up inside the resonator. Due to the total internal reflection there is an evanescent field outside of the medium [24] which can be used to couple the light into/out to the structure. Since the late of 19th century and early 20th century, the theoretical studies were carried out on spherical particles independently by several physicists, including Ludvig Lorenz (1890) [25], Gustav Mie [26] and Peter Debye [27]. Gustav Mie was investigating solutions within colloidal structures and noticed sharp resonances when light passed through them. Debye was making the same with light scattering from sphere. A new field of study was emerging [28, 29, 30]. At the beginning the term morphological dependent resonance (MDR) was used, but shortly after, WGM had taken hold. In the last decades, the scientific community shown a great interest for the potentiality of WGM resonators. Current researches include biological sensing [31], optomechanics [32, 33], cavity quantum electrodynamics [34]], optical switching [35], frequency comb generation [36], and ultra-narrow filtering techniques [37] and, last but not least, microcavity lasers [38, 39, 40]. The high quality factors and small mode volumes lead to very high field density inside the WGM cavity, which can be exploited for nonlinear interaction of various kind [41]. Even if the resonator is fabricated from trasparent material with low nonlinearity, the WGMs provide the opportunity to achieve a high nonlinear response. On the other hand, WGM sensors have shown unprecedented sensitivity for the detection of label-free biomolecules. WGM based sensing devices are among the most sensitive in comparison with other label-free technologies that can be integrated on microchips such as nanoplasmonic systems, FET nanowires, nanomechanical cantilever and nanopores. Improvements in the engineering and integration of more robust WGM platforms can bring to a multitude of applications in life science, bioengineering and enviromental monitoring. Studies are alredy underway to

get multiplexed and portable lab-on-chip devices. The use of prism coupler or integrated waveguides for evanescent coupling were the first step toward that direction [42].

1.1 Thesis outline

This thesis investigates how such structures, in particular silica microspheres and microbubbles, can be used to study non linear phenomena and can operate as frequency converters and laser sources. It is possible to easily get SRS assisted broadband visible light generation. The cascaded SRS signals allow to have a very broad spectrum in the IR range. The emissions at the visible wavelength are due to the THG and SFG of the cascaded SRS signals. Thanks to broad bandwidth light at the IR wavelength, a visible light with a broad bandwidth can be obtained.

Much attention has been focused also on the coupling tecniques which is a critical point for practical applications of WGM based devices. A new LPGs based coupler has been developed in order to improve the robustness of the WGM device for sensing applications.

Each chapter of this thesis is organized to combine the needed theory followed by our experimental works. It is divided into four chapters.

Chapter 2 reviews the features of the WGM spherical microresonators: free-spectral range, quality factor, mode volume and field distribution. Then the coupling features of the tapered fiber, the nonlinearity in WGM resonators and few sensing applications are introduced.

Chapter 3, after an introduction on Raman scattering and Four Wave Mixing interaction, describes how efficient stimulated anti-Stokes Raman scattering has been observed in silica microspherical resonators pumped by CW laser. This process is observed in the normal dispersion regime. The lack of correlation between stimulated antiStokes and Stokes scattering spec-

tra indicates that the signal has to be resonant with the cavity. Cavity resonant enhanced stimulated Raman scattering (SRS), four-wave mixing, and broadband hyper-parametric oscillation in silica microbubble whispering gallery mode resonators (WGMR) in forward and backward directions are reported. After that we have shown that microbubbles can operate not only in a highly ideal two-photon emission regime, but also generate combs, both natively and multimode spaced. The nonlinear process is phase matched because of the interaction of different mode families of the resonator. The two last paragraphs of this chapter have appeared in two articles published in Optics Letters and the related experiments can be seen in a publication on the Journal of Visualized Experiments [43].

Chapter 4 focuses on optical frequency conversion. We analyze, experimentally and theoretically, a variety of $\chi^{(3)}$ nonlinear interactions in silica microspheres, consisting of third harmonic generation and Raman assisted third order sum-frequency generation in the visible. A tunable, room temperature, cw multicolor emission in silica microspherical whispering-gallery-mode microresonators has been achieved by controlling the cavity mode dispersion and exciting nonequatorial modes for efficient frequency conversion.

This work has been published in Physical Review Letters.

Chapter 4 presents a new method for coupling light to high-Q silica whispering gallery mode resonators (WGMs) that is based on long period fiber gratings (LPGs) written in silica fibers. An LPG allows selective excitation of high-order azimuthally symmetric cladding modes in a fiber. Coupling of these cladding modes to WGMs in silica resonators is possible when partial tapering of the fiber is also implemented in order to reduce the optical field size and increase its external evanescent portion. Importantly, the taper size is about one order of magnitude larger than that of a standard fiber taper coupler. The suggested approach is therefore much more robust and useful especially for practical applications. We demonstrate coupling to

high-Q silica microspheres and microbubbles detecting the transmission dip at the fiber output when crossing a resonance. An additional feature of this approach is that by cascading LPGs with different periods, a wavelength selective addressing of different resonators along the same fiber is also possible. The proposed coupling structure is robust and can be replicated many times along the same fiber simply cascading LPGs with different bands. Typical Q-factors of the order of 10^8 and total coupling efficiency up to 60% were measured collecting the resonances of microspheres or microbubbles at the fiber end. This approach uniquely allows quasi-distributed and wavelength selective addressing of different micro-resonators along the same fiber. Works in this chapter have appeared in Optics Letters and Optics Express.

1.1.1 List of selected publications

1. D. Farnesi, Franco Cosi, Cosimo Trono, Giancarlo C. Righini, Gualtiero Nunzi Conti, and Silvia Soria, "Stimulated anti-Stokes Raman scattering resonantly enhanced in silica microspheres" Optics Letters, Vol. 39, Issue 20, pp. 5993-5996 (2014).

2. D. Farnesi, A.Barucci, G.C.Righini, G. Nunzi Conti and Silvia Soria, "Generation of hyper-parametric oscillations in silica microbubbles" Optics Letters, Vol. 40, No.19 (2015).

3. D.Farnesi, A.Barucci, G. Righini, S. Berneschi, S. Soria, and G. Nunzi Conti "Optical Frequency Conversion in Silica-Whispering-Gallery-Mode Microspherical Resonators", Physics Review Letters 112, 093901 (2014).

4. D. Farnesi, F. Chiavaioli, G. C. Righini, S. Soria, C. Trono, P. Jorge, and G. Nunzi Conti, "Long period grating-based fiber coupler to whispering gallery mode resonators" Optics Letters, Vol. 39, Issue 22, pp. 6525-6528 (2014)

5. D. Farnesi, F. Chiavaioli, F. Baldini, G. C. Righini, S. Soria, C. Trono, and G. Nunzi Conti, "Quasi-distributed and wavelength selective addressing of optical micro-resonators based on long period fiber gratings" Optics Express, Vol. 23, N.16 (2015).

6. D.Farnesi, S. Berneschi, F.Cosi, G.C.Righini, S. Soria and G. Nunzi Conti, "Stimulated Stokes and Antistokes Raman Scattering in microspherical whispering gallery mode resonators" J. Vis. Exp., Issue 110 (2016); doi: 10.3791/53938.

Chapter 2

Spherical WGM resonators

2.1 General properties

A WGM resonator (WGM) can be considered as a Gires-Tournois cavity (a Fabry-Perot cavity with one mirror reflecting 100%).

The free spectral ranges (FSR) are determinated by frequency separation between the successive modes with the same transverse structure [47]. For a azimutally-simmetric resonator the FSR is

$$\Delta\nu_{FSR} = \frac{c}{2\pi nR} \tag{2.1}$$

where c is the light speed, n the refractive index of the host material and R the radius of the circular wall. The resonators are characterized by two dependent values: the finesse ($\mathcal{F}$) and the quality factor Q. For a FP resonator, the finesse depends on the quality of its mirrors

$$\mathcal{F} = \frac{\pi\Re^{1/2}}{1-\Re} \tag{2.2}$$

where $\Re$ is the reflectance of the mirrors.Whispering gallery mode (WGM) resonators allow of achieving larger finesse compared to FP resonators.

The finesse $\mathcal{F}$ can be measured, for all kinds of resonator, by the ratio of the FSR and the full width at the half maximum (FWHM):

$$\mathcal{F} = \frac{\Delta\nu_{FSR}}{FWHM} \tag{2.3}$$

Otherwise, the quality factor(Q) is defined as the ratio of the energy storage to the energy lost per round trip and it can be usefull to expressed the cavity losses:

$$Q = \frac{2\pi \times energy\ stored}{energy\ lost}. \tag{2.4}$$

That ratios can be expressed as the light frequency ν times the photon lifetime in the cavity τ [44]

$$Q = 2\pi\nu\tau \tag{2.5}$$

here τ is related to the linewidth of the resonance $\Delta\lambda$ (or FWHM) by

$$\tau = \frac{1}{2\pi\Delta\lambda} \tag{2.6}$$

Finally, the quality factor can be obtained experimentally by measuring $\Delta\lambda$

$$Q = \frac{\lambda}{\Delta\lambda} \tag{2.7}$$

The overall Q can be decomposed into different loss contributions:

$$\frac{1}{Q_{tot}} = \frac{1}{Q_{mat}} + \frac{1}{Q_{WGM}} + \frac{1}{Q_{ss}} + \frac{1}{Q_{coup}} \tag{2.8}$$

where

- Q_{mat} is due to the material loss;
- Q_{WGM} is given by radiation loss present in a curved dieletric cavity

- Q_{ss} is due to the scattering from surface

- Q_{coup} represents the loss due to the coupling.

The quality factor is simply related to the finesse by

$$Q = \frac{2\pi Rn}{\lambda}\mathcal{F} = m\mathcal{F} \tag{2.9}$$

where m is azimutal number (or the number of optical wavelengths per ring circumference)[45].

The circulating power build-up factor can be expressed by

$$\frac{P_{cav}}{P_{in}} = \frac{\lambda}{\pi^2 nR}\frac{K}{(K+1)^2}Q_{intr} \tag{2.10}$$

where K is the ratio of the intrinsic quality factor Q_{intr} to the coupling one Q_{coupl}. The long cavity lifetime in high-Q microcavities allows to easily reach circulating power of hundreds of watts with low input power (1 mW).

In addiction to the temporal confinement, WGM resonators allow to spatially confine the light. In literature we can find several definitions of mode volume. The most common is related to the energy density of the mode and it is defined as the equivalent volume, the mode occupies, if the energy density was distributed homogeneously throughout the mode at the peak value:

$$V_{mod} = \frac{\int \epsilon(r) \mid E(r) \mid^2 \, d^3r}{max(\epsilon(r) \mid E(r) \mid^2)} \tag{2.11}$$

the integral is over all space, including even the regions where the field is evanescent. The strong spatial confinement, due to the small dimensions of WGM microresoantors, can allow reaching power densities of the order of GW/cm^2.

2.2 Mode structure

The mathematical expression for WGMs in a spherical resonator starts from the Helmholtz equation for the propagation waves $\nabla^2 E + k^2 E = 0$ where E is the transverse electric (TE) or magnetic (TM) component of the field. The modes propagating in a dielectric cavity could be obtained by considering that equation in spherical coordinates:

$$\frac{1}{r^2}\frac{\partial^2}{\partial r^2}(r\psi) + \frac{1}{rsin(\theta)}\frac{\partial}{\partial r}\left(sin(\theta)\frac{\partial}{\partial\theta}\psi\right) + \frac{1}{r^2 sin^2(\theta)}\frac{\partial^2}{\partial\phi^2}\psi - n^2k^2\psi = 0 \quad (2.12)$$

It can be separated into its contribution for each direction $E(r,\theta,\phi) = \psi_r(r)\psi_\theta(\theta)\psi_\phi(\phi)$.

For a sphere of radius R and refractive index n, the optical fields are given by:

$$E(r,\theta,\phi) = \begin{cases} j_l(kr)X_{lm}(\theta,\phi) & r < R \\ j_l(kR)h_l^1(kr)/h_l^1(kR)X_{lm}(\theta,\phi) & r \geq R \end{cases} \quad (2.13)$$

where $X_{lm} = [(l(l+1))]^{-1/2}Y_{lm}$ represent the spherical harmonics and j_l and h_l^1 denote the spherical Bessel and the Hankel functions, respectively.

The total internal reflections of the field inside the cavity result in an evanescent field tail (Fig.2.1) as shown by the variation of the radial component ψ_r with radius according to

$$\psi_r(r) = \begin{cases} Aj_l(kr) & r < R \\ Be^{-\alpha_{ev}(r-R)} & r \geq R \end{cases} \quad (2.14)$$

where α_{ev} is the field decay constant.

The characteric equation, obtained by imposing the bondary condiction and so matching Bessel and Hankel functions, allows to get the resonance positions:

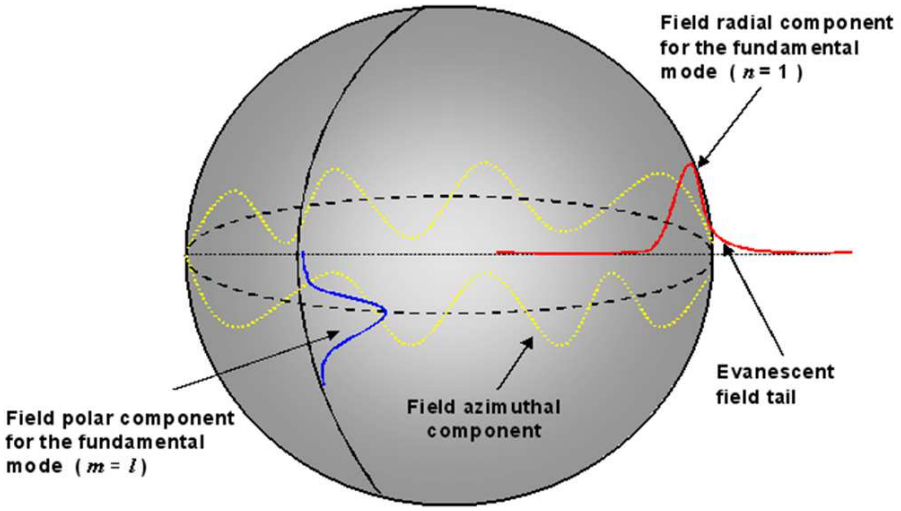

Figure 2.1: Spherical mode fields for the fundamental (n = 1) WGM [46].

$$\frac{j_l'(kr)}{j_l(kr)} = \frac{h_l'(kr)}{h_l(kr)} \tag{2.15}$$

The solution of this equation results in a wavenumber which determines the resonance wavelenght ($\lambda = 2\pi/k$).

The modes can be identified by four mode numbers, which are the radial n, the polar l, the azimuthal mode number m, and also the polarization number p. n is extracted from the Bessel function and denotes the number of field maxima along the radial direction within the sphere. l and n are from the spherical harmonics. l could be regarded as the number of wavelength enclosed along the equator of the sphere. m classifies different components of the spherical harmonics with the same l and $\mid m \mid \leq l$. m denotes the number of field maxima in the azimuthal path around the equator, and $l - m + 1$ is the number of field maxima in the polar direction. For an ideal spherical shape, the frequencies for modes $m \neq l$ are degenerate. Otherwise, for a more realistic condiction in which the resonator deviates from shape of a perfect sphere, the degeneracy is broken giving rise to a multitude of resonant frequencies for each m [48, 49].

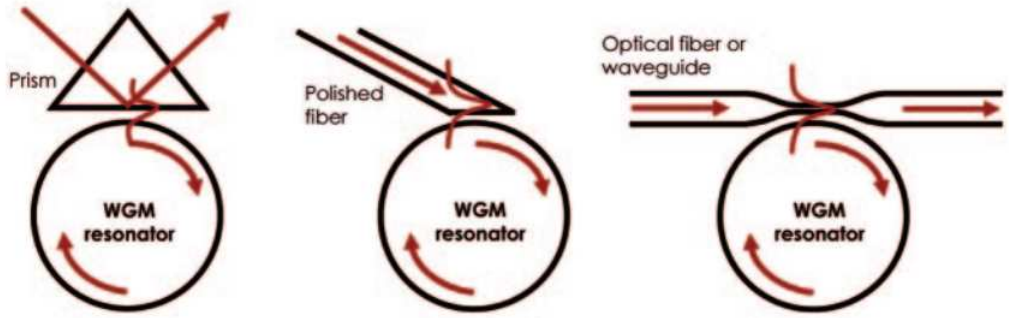

Figure 2.2: Prism coupling using frustrated total internal reflection, Slant-cut optical fiber coupling and tapered fiber coupling [47].

2.3 Optical Coupling

The prerequisite for our experimentsion WGM resonators is based on the tapered optical fiber coupling technique. The tapered fiber allows to efficiently excitate the modes. Otherwise, in the case of free-space excitation, the coupling results to be extremely inefficient due to different phase velocities in air and in the material (i.e. silica). The excitation can be achieved using the tunneling of the evanescent field components with phase matched wavevectors. Other devices most commonly used to inject light in the cavities are either prisms, waveguides and polished fibers (Fig.2.2).

The tapered fibers have multiple benefits. They can be made with low-loss and allow efficient excitation with neglegible parasitically induced losses (such as scattering). They allow not only to excite but also to extract the cavity fields through the same taper. Finally, they have small dimension and high flexibility in comparison to the other tools.

The optical fiber, from which tapers are obtained, were introduced for the first time around 1950 in the medical field [50], but only during the early 1970's, the Corning scientists were able to create a low loss optical fiber (20dB/km) capable of carrying light over a long distance. Nowadays, their losses are less than 0.2 dB/km at 1.55μm and the comunication rate is

around 10Gbit/s [51]. An optical fiber generally consists of a core, surrounded by cladding which has a lower RI and outside a jacket which protects the fiber enhancing its robustness and strength. The radial dependence of the fundamental mode in a standard optical fiber, assuming linear polarization, takes the form [52, 53]

$$F_o(\rho) = N_f \begin{cases} J_0^{-1}(k_f a) J_0(k_f \rho), & \text{if } \rho \leq a \\ exp[-\gamma_f(\rho - a)] & \text{if } \rho \geq a \end{cases} \tag{2.16}$$

where the normalization constant is

$$N_f = \frac{\alpha_f J_0(k_f a)}{V_f \sqrt{\pi} J_1(k_f a)} \tag{2.17}$$

where $k_f = \sqrt{k^2 n_f^2 - \beta_f^2}$, $\alpha_f = \sqrt{\beta_f^2 - k^2 n_{cl}^2}$, the decay constant $\gamma_f = K_1(\alpha_f a)/K_0(\alpha_f a)$ and $V_f = ka\sqrt{n_f^2 - n_{cl}^2}$. The propagation constant β_f is given by the characteristic equation

$$k_f \frac{J_1(ak_f)}{J_0(ak_f)} = \alpha_f \frac{K_1(a\alpha_f)}{K_0(a\alpha_f)} \tag{2.18}$$

where J_0 and J_1 are the Bessel function of zero and first order, while K_0 and K_1 are the modified Hankel functions of zero and first order. In the untapered single mode fiber, the core guides the lowest-order HE_{11} mode. In the case of tapered fiber, the cladding and the core radii decrease maintaing constant the relative size. The decrease of the core radius leads to an increase of the spot size and causes the most of the power of HE_{11} mode propagates in the cladding. The transition point, at which there is the change from being a core-guided to a cladding-guided mode, occurs when the decrease in the core radius results in a normalized frequency $V_{core} = (2\pi\rho_{core}/\lambda)\sqrt{n_{core}^2 - n_{clad}^2} = 1$ [54].

In our adiabatic taper only the fundamental mode is kept along the tapered section of the fiber.

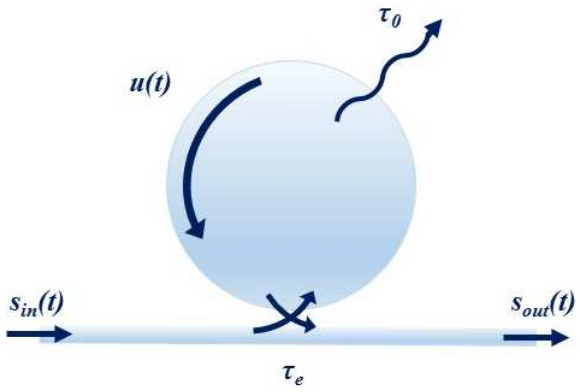

Figure 2.3: Optical resonator coupled to a taper. The input and the output field are s_{in} and s_{out}, u is the mode amplitude, τ_0 is the intrinsic photon lifetime and τ_e is the coupling photon lifetime.

If a microcavity is brought in proximity of the evanescent field tail of a tapered fiber, the coupling between the waveguide and the resonator can be described by the parameter $1/\tau_{ex}$. In other words the input signal s_{in} is coupled to the resonantor with a characteristic lifetime τ_{ex} while intrinsic losses are described by τ_0.

The lifetimes are related to the quality factor by $Q = \omega\tau/2$. The dynamic evolution of resonator-coupler system can be calculated, using the the coupled modes theory [55, 56] by integrating the equation

$$\frac{du}{dt} = \left(j\omega_0 - \frac{1}{\tau}\right) u(t) + \sqrt{\frac{2}{\tau_{ex}}} s_{in}(t) \tag{2.19}$$

The input and output fields can be written respectively as $s_{in}(t) = s_0 e^{j\omega t}$ and $s_{out}(t) = -s_{in}(t) + \sqrt{(2/\tau_e)u(t)}$. The mode amplitude is

$$u(t) = \frac{\sqrt{\frac{2}{\tau}} s_0 e^{j\omega t}}{j(\omega - \omega_0) + \frac{1}{\tau}} \tag{2.20}$$

The transfer function of the resonator-coupler system can be defined as

$$x(t) = \frac{s_{out}(t)}{s_{in}(t)} = \sqrt{T}e^{j\phi} \tag{2.21}$$

where T is the transfer function and ϕ is the phase shift. Therefore, the transmission $T = |x|^2$ can be written as

$$T = \frac{(1/\tau_{ex} - 1/\tau_0)^2 4\pi^2\delta^2}{(1/\tau_{ex} + 1/\tau_0)^2 4\pi^2\delta^2} \tag{2.22}$$

where $\delta = (\omega - \omega_0)/2\pi$. The values of τ_0 and τ_{ex} determine the coupling regime [57]:

- $\tau_0^{-1} = \tau_{ex}^{-1}$ the losses are equal to the coupling rate and the resonator is critically coupled. The trasfered power to the resonator is maximal;
- $\tau_{ex}^{-1} < \tau_0^{-1}$ the resonator is undercoupled, the coupling is weak;
- $\tau_{ex}^{-1} > \tau_0^{-1}$ the resonator is overcoupled.

2.4 Materials and Nonlinearity

Whispering gallery mode resonators have been made from different materials: amorphous material (fused silica), isotropic crystals (CaF_2 and MgF_2), nonlinear crystals ($LiNbO_3$ and beta barium borate - BBO) and polymers (polymethyl methacrylate - PMMA). Silica is usually used because of low losses. The missing oxygen defects in the atomic structure of silica can induce absorption but the main causes of losses are the metal impurities (iron, nickel and chromium) that can be introduced during the fabrication inducing absorption in the blue part of spectrum. The amount of water and the O-H bonds are critical because of their vibrational band near infrared. Other contributions to the intrinsic absorption of silica are due to the vibration of silicon-oxygen (Si-O) bonds on longer wavelenght and to the electronic transitions at UV wavelenghts. The presence of small density fluctuation and

defects can induce Rayleigh scattering. Only the portion irradiated out of the resonator contributes to the loss [58]. The minimum overall loss occurs at 1.55μm which is the operating wavelength for telecomunications.

For the study of nonlinear optical effects, one would not choose silica at first sight. It does not have a second order nonlinerity $\chi^{(2)}$ (due to its inversion symmetry) and the third order nonlinearity χ^3 is two orders of magnitude smaller than the majority of other materials. But despite a weak non linearity, silica has the hightest nonlinearity to attenuation ratio of any material system [59]. In general its nonlinear optical response is described by the expantioning of the polarization

$$P_i = \epsilon_0 \chi^{(1)}_{ij} E_j + \epsilon_0 \chi^{(3)}_{ijkl} E_j E_k E_l \tag{2.23}$$

So the NL effects are associated with the different products of the field operators $E_j E_k E_l$ and the silica susceptibility, which exhibit a real and imaginary part,

$$\chi^{(3)} = \chi^{(3)}_{Re} + i\chi^{(3)}_{Im} \tag{2.24}$$

This latter has an instantaneous and a time delayed response. The first one is determinated mainly by the far-off resonant electronic response and for a small part by the phonons [76]. The refractive index depends linearly on the intensity

$$n(I) = n_0 + n_2 I \tag{2.25}$$

where

$$n_2 = \frac{3}{8nc\epsilon_0}\chi^3 \tag{2.26}$$

Finally it is worth to notice that the two-photon absorption for silica, described by the imaginary part of n_2, can be neglected since the processes

occur at photon energies of ∼9eV.

2.5 Sensing Applications

The evanescent field tail, besides being able to be used for coupling light into the cavities, allows to exploit WGMRs for sensing purposes. Its lenght out of the cavity is of the order of hundreds of nanometers and any host medium refractive index changes or even the attachment of a molecule on the cavity wall will cause a resonance wavelength shift. The different geometries have all their unique advantages in sensing: microspheres, for instance, are extremely simple to fabricate, exhibit high Q-factor and were the first optical microresonator used in biosensing [60]. The microbubbles in capillaries, a kind of hollow optical ring resonator, combine the cavity with the microfluidics. In this way they are sensitive to the RI variation of the inner medium without disturbing the coupling system [61]. Therefore, these and the other avalaible geometries can be used for label-free biosensing on chip-scale devices making the microresonator technology particularly attractive for many reseach groups around the world. In order to take into account the intensity distribution when the evanescent field tail interact with material onto the surface, we can define an effective refractive index as

$$n_{eff} = \frac{\int n(\mathbf{r})E^2(\mathbf{r})d\mathbf{r}}{\int E^2(\mathbf{r})d\mathbf{r}} \tag{2.27}$$

and find the resonance criteria,

$$2\pi n_{eff} R \approx \lambda \tag{2.28}$$

Any change in the RI or in the radius R will result in a shift $\Delta\lambda$ (Fig.2.4). The relationship is express as

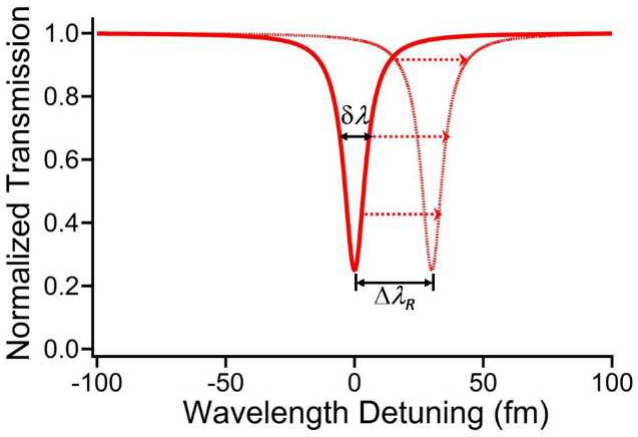

Figure 2.4: The transmission spectra depicting a resonance shifting $\Delta\lambda$ in responce to change of the refractive index.

$$\frac{\Delta\lambda}{\lambda} = \frac{\Delta n_{eff}}{n_{eff}} + \frac{\Delta R}{R} \tag{2.29}$$

The sensitivity of the resonance to the refractive index change of the host environment can be written as [62]

$$\frac{\partial x_n^{TE}}{\partial n_a} = -\frac{n_a}{(n_s^2 - n_a^2)^{3/2}} \left[1 - \frac{\zeta_l}{2^{1/3}} \frac{n_s^2}{n_s^2 - n_a^2} \nu^{-2/3}\right] \tag{2.30}$$

where $x_n = 2\pi a/\lambda_0$ is a dimensioless size parameter in which a is the radius of the cavity and λ_0 is the wavelength in vacuum. n_a and n_s denote respectively the refractive index of the sphere and surrounding medium. ζ_l is the l-th zero of the Airy function. The change in the linewidth of the resonance $\delta\lambda$, for instance induced by addictional absorption losses can also be used for sensoristic purpose [63]. A critical point is the comparison between the noise sorces present in the system and the magnitude of the induced sensing signal. A number of noise sources are fundamental and thus unavoidable. Considering a WGM sensor based on the resonance shifts and a shot noise limited resolution, the limit of detection is given by [64]

$$\frac{\partial\omega_{min}}{\omega_0} = \frac{1}{Q_0}\sqrt{\frac{\hbar\omega_0}{P\eta\beta\tau}} \tag{2.31}$$

where P is the coupled optical power, η denotes the photodetector's quatum efficiency, β is the transmission efficiency of the cavity and τ is the averaging time.

The presence of a high refractive index layer can enhance the microsphere sensitivity [65]. We have presented a study of the effect of a silicon coating on a silica sphere and we have found that it can increase its sensitivity by a large amount in particular from 5 nm/RIU to 145 nm/RIU for a $140\mu m$ sphere [66]. It was theoretically demonstrated how hollow core WGMRs have a sensing capability greater than those presented by the corresponding bulk microspheres [67]. The design of this kind of cavities represents the first and crucial step towards the optimization of their performances in term of sensitivity and limit of detection. We have proposed an analytical method for the design of optical microbubble resonators. The enhancement of the sensing performance due to a polymeric layer with a high refractive index, as coating of the inner wall of the bubble, is assessed and discussed. We have demonstrated that depositing 300 nm polymeric layers inside the silica OMBR is good compromise for having a constant RI sensitivity and a robust device (Fig.2.5).

Finally it was proven that a sub-wavelength wall thickness of the bubble does not always represent a requirement for the achivement of high device performance. This allows having mechanical robustness of the device without losing in sensitivity and limit of detection [68]. The methods for the microbubble's wall thickness evaluation and so for their robustness assessment were based only on a theoretical approach. We have demostrated that confocal reflectance can be used as a non-invasive and non-destructive method for the thickness measurement and a simple theoretical model for

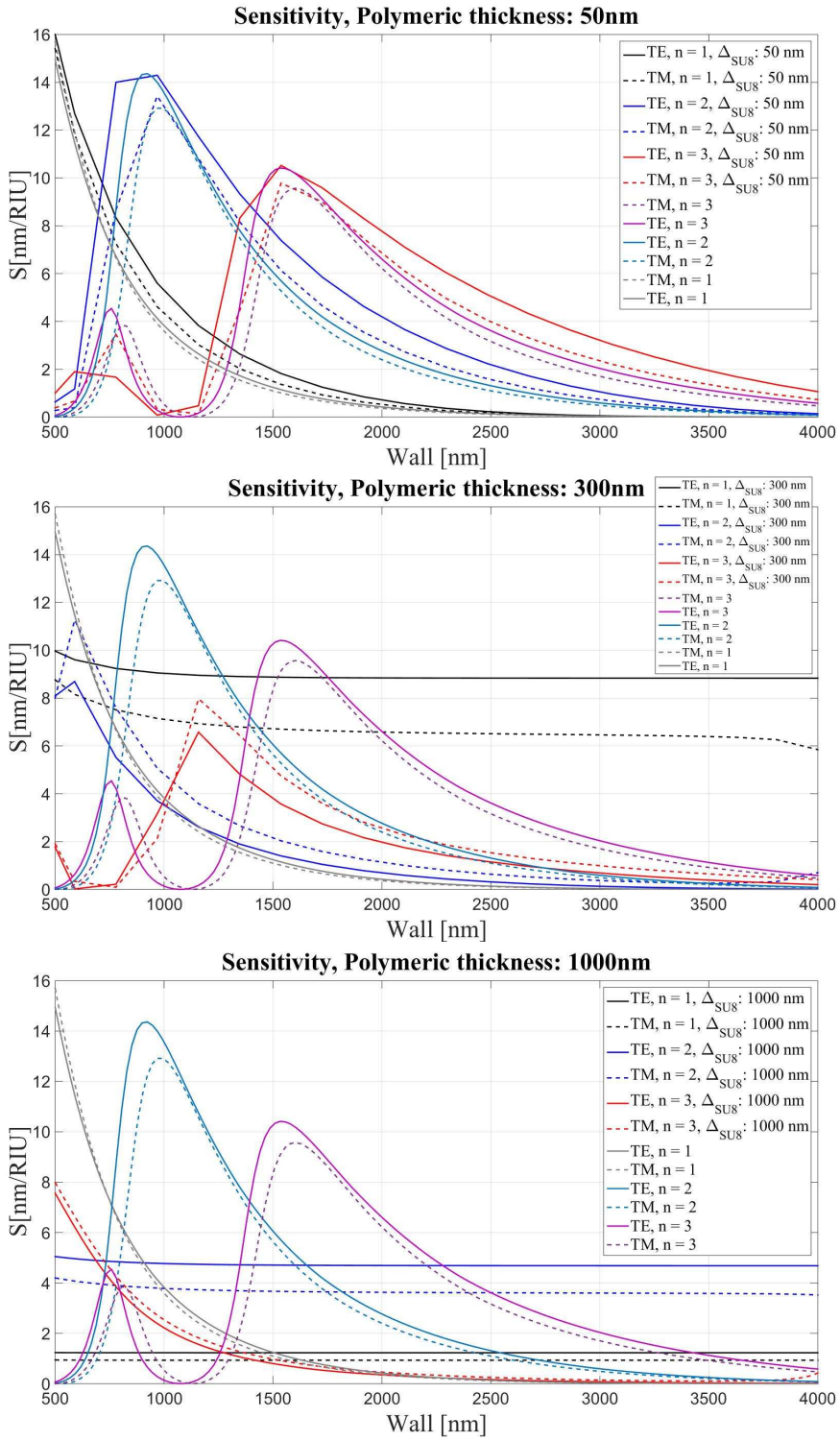

Figure 2.5: Sensitivity (nm/RIU) as a function of wall thickness for two different polarizations and 3 mode orders, corresponding to different thickness of polymeric layer: 50nm, 300nm and 1000 nm [68].

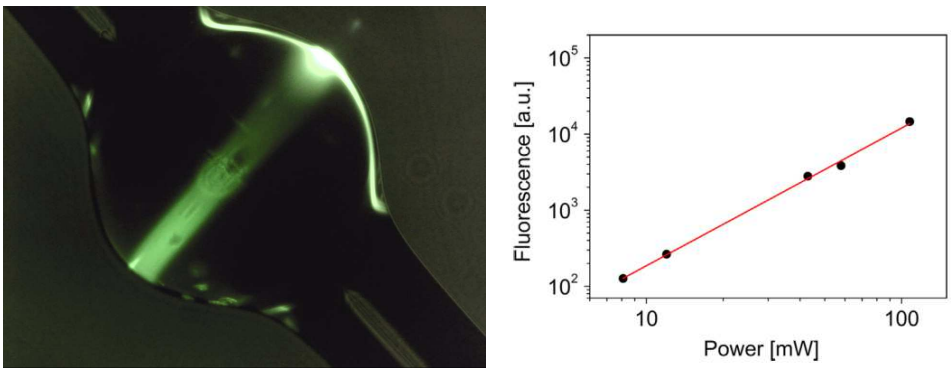

Figure 2.6: Fluorescence image of a microbubble filled with fluorescein solution, showing the TPF band. Logarithmic presentation of the TPEF signal from the MBR filled with 10^{-6} M Rhodamine 6G solution versus incident laser power in log-log scale.

thickness range value calculation was proposed [69]. Microresonator experiments, in particular with hollow cavities, are affected by thermo-mechanical fluctuations which interfere with the resonance position measurements. For example the thermal drift could overstimate the shift due to a the presence of a target molecule. We have proposed a PMMA surrounding box for the coupler-resonator system and we have demonstrated that it reduces the total fluctuations [70].

As example of WGM biosensors we have investigated the feasibility of immunosensors for the fast detection of immunoreactions. A crucial step for producing reliable biosensors is the surface functionalization to bind the recognition bio-element on it. This functionalization layer has to be very thin in order to preserve the high quality factor of the transducer and the interaction of the WGMs with the sensing layer. We tested the feasibility of one photon fluorescence (OPF) with spherical WGMR where antibodies against Staphyolococcus aureus cell wall, labeled with a near infrared dye, were immobilized on its surface. WGM resonators can be even exploited to get high photon flux densities needed for two photon fluorescence (TPF) mea-

surements which have a number of advantages over measurements with OPF. We have demonstrated the potential of microbubbles as nonlinear enhancement platform and verified the feasibility of exciting TPF in microresonators where labeled IgGs were covalently bound to its surface (Fig.2.6)[71].

Chapter 3

Raman scattering and four wave mixing in high-Q spherical microcavities

3.1 Stimulated Raman scattering

The inelastic scattering of a photon with an optical phonon, which originates from a finite response time of the third order nonlinear polarization of the material, is called the Raman scattering effect. Spontaneous Raman scattering occurs when a monochromatic light beam propagates in a material like silica. Some of the photons are transfered to new frequencies. The scattered photons may lose (Stokes shift) or gain energy (anti-Stokes shift).

In the first part of Fig.(3.1) the pump photon with energy E_p is destroyed and the molecule will be excited from the ground state (G) into a higher virtual energy state (V). The energy difference between the ground and the excited level is equal to pump photon. In a second step the molecule falls down into an inter level (I) which is generated by its own periodical oscillations or rotations. This decay is accompanied by a Stokes photon

emission. The destruction of the pump and the generation of the Stokes photon happens simultaneously baucause of the fact that V is a virtual state. The energy difference between the pump and the Stokes photon is equal to the difference between the energy levels I and G. The remaining energy is the vibrational energy delivered to the molecule.

In contrast to other kinds of nonlinear phenomena where the molecule returns to its ground level after the interaction, an energy transfer between photon and molecules takes place here. In right side of Fig.3.1 for the generation of anti-Stokes photon, the energy of the pump is equal to the energy difference between the virtual V and the inter I state. The pump photon is annihilated whereas, at the same time, an anti-Stokes photon is created. The molecule transfers a part of its motion energy to the scattered photon and increase its energy and frequency. Normally the intensity of Stokes wave is much bigger than the anti-Stokes intensity because, in the case of a thermal equilibrium, the allocation of inter state (I) is much smaller than the occupation of the ground state (G).

Raman scattering depends on particular material resonances. In crystalline media, these resonances show a very narrow bandwidth. On the other hand, in amorphous silica the molecular vibration mode are overlapped with each other and create a continuum [72]. Fig.3.2 shows the Raman gain g_R in silica versus the frequncy shift between pump and Stokes wave normalized to the maximum. g_R extends over a range up to 40 THz with a broad peak located near 13 THz.

If the intensity exceeds the threshold, stimulated scattering can occur. The transition between spontaneous and stimulated scattering can be described with the model of the harmonic oscillator. If at the input layer of the medium the pump hits a dipole oscillating with its resonance frequency, an additional Stokes wave will be generated. The Stokes field radiation by another dipole has different phase than the first one. Hence, no coherent

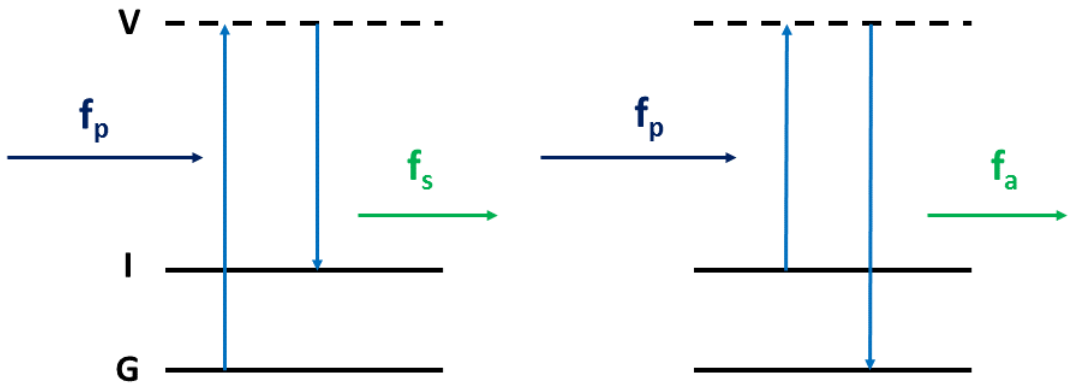

Figure 3.1: Schemeatic representation of the energy levels ofRaman Scattering representation.

superposition can occur. In conseguence, a weak wave is radiated into arbitrary directions. On the other hand, if the intensity of the pump is higher than the threshold, the wave scattered at the first dipole is relatively intense. Pump and emitted Stokes waves propagate through the material and the following dipole is driven by the difference between both of them to oscillate at their resonance frequency. In this case the phase of the excited dipole is determinated by the incident wave. The Stokes wave of the following dipole superimposes coherently in the forward direction with the Stokes wave of the first dipole. Therefore, the intensity grows and the next dipoles are driven stronger to oscillate at their resonance frequency.

Tipically spontaneous Raman scattering is a rather weak process. Even for condensed matter, the scattering cross section per unit volume is only $10^{-6}cm^{-1}$. Hence, for instance, only 1 part in 10^6 of the incident radiation will be scattered into the Stokes frequency after the propagation through 1 cm of the scattering medium. Contrary to spontaneous emission, SRS can trasform a large part of power into a new frequency-shifted wave and the intensity grows exponentially with the propagation distance in the nonlinear (NL)

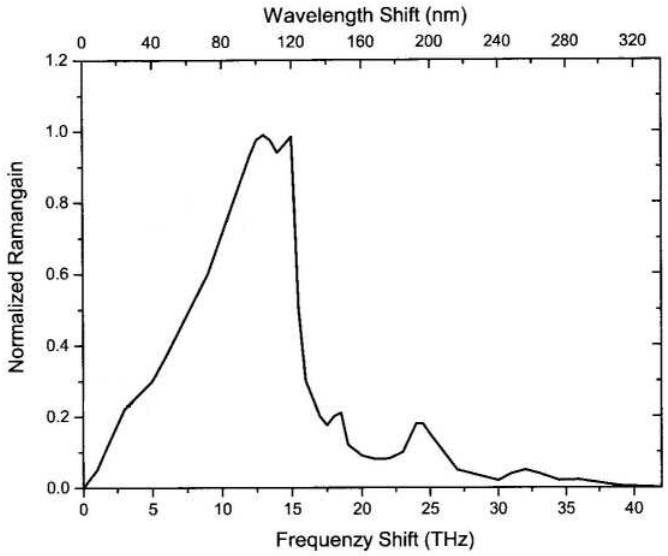

Figure 3.2: Normalized Raman gain vs the frequency shift between the pump and the Stokes wave [77].

material. Highly efficient scattering can occur as a result of the stimulated version under excitation by an intense laser beam. 10% or more of the energy of the incident laser beam can be converted.

Generally, in WGM resonators, the lasing threshold occurs when the cavity round-trip gain equals round-trip loss. The intra-cavity gain coefficient is related to the bulk Raman gain coefficient g_b (in silica the maximum is $6.5 \times 10^{14} m/W$ at 1550nm) through the equation

$$g_R = \frac{c^2}{C(\Gamma) 2 n^2 V_{eff}} g_b \tag{3.1}$$

where V_{eff} is the effective modal volume and $C(\Gamma)$ is the modal coupling. The threshold pump power can be derived by the gain coefficient and taking into account the power build-up factor in the resonator:

$$P_{th} = \frac{\pi^2 n^2 V_{eff}}{\lambda_p \lambda_R C(\Gamma) g_R Q^2} \tag{3.2}$$

it follows an inverse dependence on the squared of the quality factor Q

of the cavity. This shows how an increase in Q will cause a twofold benefit in terms of reducing cavity round trip losses as well as increasing the Raman gain, due to the Raman gain dependence on the pump intensity.

The Raman scattering can be seen as the coupling of the vibration waves and light waves via a molecular system can be properly discussed through classical description if there are many photons in the radiation field. In the coupled-wave problems, the classical description is even more appropriate since then the decay or amplification of the wave depends on the relative phases among them. In the quantum description, if the number of quanta is prescribed, the phase will be completely undetermined as require by the uncertainty principle [73].

Contrary to the parametric effects, Raman scattering is intrinsically phase-matched over the energy levels of the molecule. In other words it is a pure gain process. Infact, the Stoke absorption coefficient

$$\alpha_S = -3i\frac{\omega_S}{n_S}c\chi_R(\omega_S) \mid A_L \mid^2 \tag{3.3}$$

depends only on the modulus of the complex amplitude of the pump field A_L. The imaginary part of $\chi_R(\omega_S)$ is negative, implying that the real part of α_S is negative and so, as said above, the Stokes waves experiences an exponential growth. The spatial evolution of the Stokes field amplitude A_S is given, in the slowy varying amplitude approximation, by

$$\frac{dA_S}{dz} = -\alpha_S A_S \tag{3.4}$$

which is obtained starting from driven wave equation

$$-\nabla\tilde{E}^2 + \frac{\epsilon}{c^2}\frac{\partial^2\tilde{E}}{\partial t^2} = -\frac{1}{\epsilon_0 c^2}\frac{\partial^2\tilde{P}^{NL}}{\partial t^2} \tag{3.5}$$

where the nonlinear response of the medium acts as a source term.

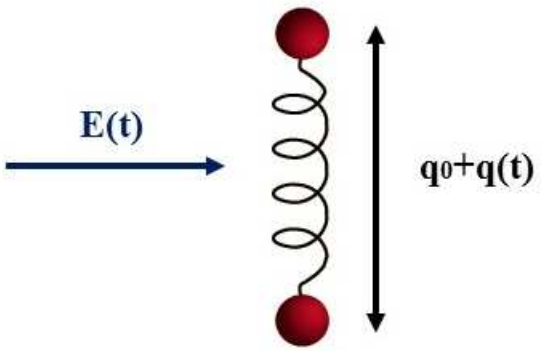

Figure 3.3: Molecular description of stimulated Raman scattering.

In order to derive the nonlinear polarization we start by two assumptions: first, the vibrational mode can be described as a harmonic oscillator; and second, the optical polarizability of the molecule is not constant but depends on the internuclear separation $\tilde{q}(t)$. The motion equation, for the molecule vibration, is

$$\frac{d^2\tilde{q}}{dt^2} + 2\gamma\frac{d\tilde{q}}{dt} + \omega_v^2\tilde{q} = \frac{\tilde{F}(t)}{m} \tag{3.6}$$

where ω_v and γ are the resonance frequency and the damping constant of the harmonic oscillator, respectively. $\tilde{q}$ represents the deviation of the internuclear distance from its equilibrium value q_0, $\tilde{F}(t)$ denotes any force on the vibrational mode and m is the reduced nuclear mass (Fig.3.3).

The polarizability can be defined as

$$\tilde{\alpha}(t) = \alpha_0 + \left(\frac{\partial\alpha}{\partial q}\right)_0 \tilde{q}(t) \tag{3.7}$$

where α_0 is the polarizability of the molecule at its equilibrium. When the molecules are set into oscillation, their polarizability will be modulated periodically in time, inducing the refractive index modulation

$$\tilde{n}(t) = \sqrt{\tilde{\epsilon}(t)} = [1 + N\tilde{\alpha}(t)]^{1/2} \tag{3.8}$$

The beam, passing through the medium, is modified by the temporal modulation of n. The trasmission will have two frequency sidebands separated by $\pm\omega_v$.

To deeply understand the interaction that give rise to SRS we need to start from how the molecular vibration can be coherently driven by an applied optical field. $\tilde{E}(z,t)$ will induce a dipole moment

$$\tilde{p}(z,t) = \epsilon_0 \alpha \tilde{E}(z,t) \tag{3.9}$$

to the molecule located in z. The time-varying applied force, at the beat frequency of the field components, is given by

$$\tilde{F} = \frac{dW}{dq} = \frac{\epsilon_0}{2}\left(\frac{d\alpha}{dq}\right)_0 \tilde{E}(z,t) \tag{3.10}$$

The SRS can be summarized in two parts: (1) the molecular vibrations modulate the refractive index of the medium at frequency ω_v and the frequency sidebands are induced in the laser field. (2) the Stokes field at frequency $\omega_S = \omega_L - \omega_v$ beats with the laser field to produce the modulation of the total intensity which excites the molecular oscillation at frequency $\omega_L - \omega_S = \omega_v$. In this way the two processes reinforce one another. In order to define the Raman suscetibility, we need to start by the time-varying part of Eq.(3.10):

$$\tilde{F}(z,t) = \epsilon_0 \left(\frac{\partial\alpha}{\partial q}\right)_0 \left[A_L A_s^* e^{i(Kz-\Omega t)} + c.c.\right] \tag{3.11}$$

assuming that the total optical field can be represented as

$$\tilde{E}(z,t) = A_L e^{i(k_L z - \omega_L t)} + A_S e^{i(k_S z - \omega_S t)} + c.c. \tag{3.12}$$

where $K = k_L - k_S$ and $\Omega = \omega_L - \omega_S$.

By solving the motion equation (3.6), we can get the amplitude of the molecular vibration

$$q(\Omega) = \frac{(\epsilon_0/m)(\partial\alpha/\partial q)_0 A_L A_S^*}{\omega_v^2 - \Omega^2 - 2i\Omega\gamma} \tag{3.13}$$

and by inserting Eq.(3.7) into Eq.(3.10), the polarization of the medium is

$$\tilde{P}(z,t) = N\tilde{p}(z,t) = \epsilon_0 N \left[\alpha_0 + \left(\frac{\partial\alpha}{\partial q}\right)_0 \tilde{q}(z,t)\right] \tilde{E}(z,t) \tag{3.14}$$

Its nonlinear part contains different frequency components:

$$\tilde{P}^{NL}(z,t) = \epsilon_0 N \left(\frac{\partial\alpha}{\partial q}\right)_0 \left[q(\Omega)e^{i(Kz-\Omega t)} + c.c.\right] \times \left[A_L e^{i(k_L z-\omega_L t)} + A_S e^{i(k_S z-\omega_S t)} + c.c.\right] \tag{3.15}$$

The part that oscillates at ω_S is the Stokes polarization

$$\tilde{P}^{NL}(z,t) = P(\omega_S)e^{-i\omega_S t} + c.c. \tag{3.16}$$

in which the complex amplitude is given by

$$P(\omega_S) = N\epsilon \left(\frac{\partial\alpha}{\partial q}\right)_0 q^*(\Omega) A_L e^{ik_S z} \tag{3.17}$$

by introducing Eq. (3.13) we find that

$$P(\omega_S) = \frac{(\epsilon_0^2 N/m)(\partial\alpha/\partial q)_0^2 \mid A_L \mid^2 A_S}{\omega_v^2 - \Omega^2 + 2i\Omega\gamma} e^{ik_S z} \tag{3.18}$$

From this formulation the Raman susceptibility can be defined as

$$\chi_R(\omega_S) = \frac{\epsilon_0 (N/6m)(\partial\alpha/\partial q)_0^2}{\omega_v^2 - (\omega_L - \omega_S)^2 + 2i(\omega_L - \omega_S)\gamma} \tag{3.19}$$

finally getting to the more common form for the Stoke polarization

$$P(\omega_S) = 6\epsilon_0 \chi_R(\omega_S) \mid A_L \mid^2 A_S e^{ik_s z} \tag{3.20}$$

The susceptibility for anti-Stokes can be deduce, in the same way, by replacing ω_S by ω_a

$$\chi_R(\omega_a) = \frac{\epsilon_0(N/6m)(\partial\alpha/\partial q)_0^2}{\omega_v^2 - (\omega_L - \omega_a)^2 + 2i(\omega_L - \omega_a)\gamma} \tag{3.21}$$

It is easy to see that the Stoke and Anti-Stokes Raman susceptibilities are related by

$$\chi_R(\omega_a) = \chi_R(\omega_S)^* \tag{3.22}$$

since $\omega_L - \omega_S = -(\omega_L - \omega_a)$ and it is worth to highlight that Stokes and anti-Stokes emission have an additional contribution beyond that described by the Raman susceptibility. The non linear part of the polarization Eq.(3.15) shows that Stokes and anti-Stokes polarization depend one on each other. For anti-Stokes, we can see that in

$$\tilde{P}_a^{NL}(z,t) = P(\omega_a)e^{-i\omega_a t} + c.c. \tag{3.23}$$

$P(\omega_a)$ depends on the Stokes amplitude

$$P(\omega_a) = N\epsilon_0 \left(\frac{\partial\alpha}{\partial q}\right)_0 q(\Omega)A_L = \frac{(N\epsilon_0^2/m)(\partial\alpha/\partial q)_0^2 A_L^2 A_S^*}{\omega_v^2 - \Omega^2 - 2i\Omega\gamma} e^{i(2k_L - k_S z)} \tag{3.24}$$

this contribution describes how SRS is affected by Four-Wave Mixing (FWM)[74]. In other words, Raman emission can be thought as down-conversion of a pump photon and a phonon associated with a vibrational mode of the molecule. Even an up-conversion process is possible but in this case the combination phonon-photon occurs rarely because it requires the presence of a photon of right energy and momentum. The anti-Stokes wave is generated together with the Stokes one. A FWM process in which two pump photons annihilate themselves to produce Stokes and anti-Stokes photon can occur $2\omega_L = \omega_a + \omega_s$, providing the total momentum conservation.

This leads to the phase-matching condition $\Delta k = 2k(\omega_L) - k(\omega_a) - k(\omega_s) = 0$ where $k(\omega)$ is the propagation constant.

We need a set of coupled equations to describe the evolution of the field amplitude. Introducing the coupling coefficients

$$\alpha_j = -\frac{4\pi i\omega_j}{n_j c}\chi_R(\omega_j) \mid A_L \mid^2 \tag{3.25}$$

and the nonlinear absoption coefficient

$$\kappa_j = \frac{6\pi i\omega_j}{2n_j c}\chi_F(\omega_j)A_L^2 \tag{3.26}$$

where $j = S, a$, we find that

$$\frac{dA_S}{dz} = -\alpha_S A_S + \kappa_S A_a^* e^{i\Delta kz} \tag{3.27}$$

$$\frac{dA_a}{dz} = -\alpha_a A_a + \kappa_a A_S^* e^{i\Delta kz} \tag{3.28}$$

These equations show how the Raman gain and loss term drive the Stokes and the anti-Stokes amplitudes. The FWM term results to be a driving term only when the wavevector mismatch Δk is small. In that case the two equation have to be solved simultaneously. Otherwise, if Δk is large the equations decouple, Stokes emission experiences gain and anti-Stokes experiences loss.

One can show that the various elements of the susceptibility are related by

$$\chi_F(\omega_s) = \chi_F(\omega_a)^* = 2\chi_R(\omega_S) = 2\chi_R(\omega_a^*) \tag{3.29}$$

the absoption and the coupling coefficient can be related to each other:

$$\alpha_a = -\alpha_S^* \left(\frac{n_S\omega_a}{n_a\omega S}\right) \tag{3.30}$$

$$\kappa_S = -\alpha_S e^{2i\phi_L} \tag{3.31}$$

$$\kappa_a = \alpha_S^* \left(\frac{n_S \omega_a}{n_a \omega_S}\right) e^{2i\phi_L} \tag{3.32}$$

where ϕ_L is the phase of the pump laser.

In solving the equations (3.27) and (3.28) we can introduce the coupled gain coefficient

$$g_\pm = -\frac{1}{2}(\alpha_1 + \alpha_2^*) \pm \frac{1}{2}\left[(\alpha_1 - \alpha_2^* + i\Delta k)^2 + 4\kappa_1 \kappa_2^*\right]^{1/2} \tag{3.33}$$

and by using the expressions (3.30),(3.31) and (3.33) we can get the dependence of $g_\pm$ on the phase mismatch:

$$g_\pm = \pm\left[i\alpha_S \Delta k - (\Delta k/2)^2\right]^{1/2} \tag{3.34}$$

The result shows that the gain vanishes in the limit of the perfect phase matching in which the anti-Stokes wave is so strongly coupled to the Stokes wave that it prevents the Stokes from growing, indicating that four-wave mixing can suppress SRS [75, 76].

The coupling between FWM and SRS can lead to the exponential amplification of the anti-Stokes wave, even under non-phase-matched conditions. All these phenomena can be understood by noting that the beat note between the pump wave and an anti-Stokes wave, generated by FWM, matches the frequency of the vibrational wave. In this way, the anti-Stokes wave is coupled to the material excitation, which in turn affects the dynamics of the SRS process. In that case the SRS can be described as a delayed contribution to nonlinearity [77] and the combined effect of FWM and SRS is given by a generalized nonlinear Schrödinger [78, 79]:

$$\frac{\partial A(z,t)}{\partial z} = -i\frac{\beta_2}{2}\frac{\partial^2 A(z,t)}{\partial t^2} + i\gamma\left[(1-f)\mid A(z,t)\mid^2 + f\int_{-\infty}^{t}\chi_R^{(3)}(t-t')\mid A(z,t')\mid^2 dt'\right]A(z,t) \quad (3.35)$$

where $A(z,t)$ is the envelope of the electric field, β_2 the dispersion and γ the nonlinearity coefficient. $\chi_R^3(t)$ is the delay Raman response function. The parameter f is the fractional contribution of the Raman susceptibility to the instantaneous Kerr effect, is estimated to be 0.18 for silica [80]. The coupled evolution of the Stoke and anti-Stokes waves can be investigated starting by:

$$A(z,t) = \left[\sqrt{P_p} + A_S(z)e^{i\Omega t} + A_a(z)e^{-i\Omega t}\right]e^{i\gamma P_p z} \quad (3.36)$$

here $A_\alpha(z) = \sqrt{P_\alpha(z)}e^{[i\phi_\alpha(z)]}$ $(\alpha = s, a)$ are the amplitudes with $\phi_\alpha(z)$ the phase of the two waves and $\Omega = \omega_p - \omega_s = \omega_a - \omega_p$ is the angular frequency shift between the pump and the Stokes/anti-Stoke emissions. We can neglect all direct coupling and consider only the first order terms in A_s and A_a. The evolution of Stokes and anti-Stokes field becomes a linear problem

$$\frac{d}{dz}\begin{bmatrix} A_S \\ A_a^* \end{bmatrix} = i\gamma P_p \begin{bmatrix} q-K & q \\ -q & -q+K \end{bmatrix}\begin{bmatrix} A_S \\ A_a^* \end{bmatrix} \quad (3.37)$$

where the complex variable q gives the strength of the real and imaginary parts of the $\chi^{(3)}$

$$q = q(\Omega) = 1 - f + f\tilde{\chi}_R^{(3)}(-\Omega) = 1 - f + f\tilde{\chi}_R^{(3)}(\Omega)^* \quad (3.38)$$

and K is the linear phase mismatch between the three waves, $K = -\Delta\beta_L/2\gamma P_p$, where $\Delta\beta_L = \beta_a + \beta_s - 2\beta_p$. Here $\beta_a = \beta(\omega_0 + \Omega)$,$\beta_s = \beta(\omega_0 - \Omega)$,$\beta_p = \beta(\omega_0)$. Because of the FWM (represented by the off-diagonal terms in the above equation), the mode is always partially anti-Stokes and then its amplitude scales inversely proportional to the linear phase-mismatch

$$\frac{A_a^*}{A_s} \approx \frac{-\gamma q P_p}{\Delta\beta_L} \tag{3.39}$$

This is valid both in normal and in the anomalous dispersion regime, as long as the phase mismatch is large. While SRS normally results in an absoption of the anti-Stokes wave, the coupling between SRS and FWM actually leads to the amplification of anti-Stokes emission with a gain close to the Stokes gain. The parametric coupling between the three waves is able to self-induce the phase matching so that anti-Stokes wave undergoes a positive parametric gain. In term of parametric anti-Stokes process the waves self-control their phase velocities to the appropriate values and self organize the phase matching condition [81].

3.2 Cascated Raman scattering

Cascated Raman scattering has always been considered as an interesting means for extending the wavelength range of the laser sources. In 2003 a microcavity-based cascated Raman laser was demostrated in WGM silica microspheres with submilliwatt pump power[82].

In cascaded Raman oscillation, the Raman signals serve to secondary pump field and generate higher-order Raman waves.As the pump power is increased, the first Stokes line extracts power from the pump until it becomes strong enough to seed the generation of a next Stokes line. This process can continue in order to generate more Raman peaks. The cascade process can be modeled as coupled harmonic oscillators with the pump and the Raman fields by including higher order coupling terms[83]

$$\frac{dE_p}{dt} = \left[-(1/2\tau_t)_p - g_{R1}^c(\omega_p/\omega_R) \mid E_{R1} \mid^2\right] E_p + k_p s \tag{3.40}$$

$$\frac{dE_{R1}}{dt} = \left[-(1/2\tau_t)_p + g^c_{R1} \mid E_p \mid^2 - g^c_{R1}(\omega_{R1}/\omega_{R2}) \mid E_{R1} \mid^2\right] E_{R1} \tag{3.41}$$

$$\frac{dE_{RN}}{dt} = \left[-(1/2\tau_t)_{RN} + g^c_{RN} \mid E_{R(N-1)} \mid^2\right] E_{RN} \tag{3.42}$$

where E_R is the slowly varying cavity field amplitude of the Nth Stokes wave, τ_t is the photon lifetime and g_R is the intracavity Raman gain coefficient. s is the pump field amplitude ($P_{in} =\mid s \mid^2$) and $k_p = \sqrt{1/\tau_{ext}}$ is the coupling coefficient of the input pump with the WG mode E_p. The thresholds for the higher order emissions can be found, in the steady state, by solving iteratively the set of equations. The even and the odd order Nth Raman field modes exhibit different threshold powers as a function of the order N, as evident from the following solutions

$$P_t^{N=2m+1} = \frac{1}{C(\Gamma)} \frac{\pi^2 n^2}{g_R \lambda_p \lambda_R} V_{eff} \frac{1}{Q_0^2} \frac{(1+K)^3}{K} \frac{(N+1)^3}{8} \tag{3.43}$$

$$P_t^{N=2m} = \frac{1}{C(\Gamma)} \frac{\pi^2 n^2}{g_R \lambda_p \lambda_R} V_{eff} \frac{1}{Q_0^2} \frac{(1+K)^3}{K} \frac{N^2(N+2)^2}{8} \tag{3.44}$$

where $C(\Gamma)$ is the modal coupling. These equations show that the all odd-orders increase as the square root of the pump power and even-orders are clamped. Otherwise, all even-order lines increase linearly with pump power while odd orders are clamped.

3.3 Cascaded Four wave mixing

The frequency comb process is based on four-wave mixing among two pump photons ω_{pump} with a signal ω_S and idler photon ω_I. It requires two condictions to be satisfied: the momentum conservation, which is intrinsically satisfied in WGM resonators [113], and the energy conservation, which is not a priori satisfied since the separation between adjacent modes $\nu_{FSR} = |\nu_m - \nu_{m+1}|$

can vary due to the material and cavity dispersion. Indeed, only in recent works, this process has been observed by coupling CW laser in microcavities exploiting the Kerr nonlinearity to enable cascaded four-wave mixing.

The comb generation can occur in two different ways: as a "Type I" (or a natively mode spaced comb) with sidebands separated by one FSR and a "Type II" (or multimode spaced comb) with sidebands separated from the pump by several FSR. Cascaded Four Wave Mixing preserve the initial spacing to higher-order emerging sidebands thank to the conservation of the energy in the parametric processes [36].

The Kerr comb formation starts by generation of the first symmetrical lines generated in a degenerate FWM process when the parametric gain overcomes the loss of the cavity. The separation of the new lines to the pump depends on the dispersion and the pump power. The nonlinear coupled mode equations can help us to understand that the first lines can oscillate either in the resonator mode near the pump or at a multiple of this separation [85]. The evolution of the mode amplitude A_μ can be described by

$$\frac{\partial A_\mu}{\partial t} = -\frac{\kappa}{2}A_\mu + \delta_{\mu 0}\sqrt{\kappa_{ext}}se^{i(\omega_p-\omega_0)}t + ig\sum_{\mu',\mu'',\mu'''} A_{\mu'}A_{\mu''}A_{\mu'''}e^{-i(\omega_{\mu'}+\omega_{\mu''}-\omega_{\mu'''}-\omega_\mu)t} \quad (3.45)$$

where $\mu = \mu^{'} + \mu^{''} - \mu^{'''}$ denotes the mode numbers, $\kappa = \kappa_0 + \kappa_{ext}$ is the cavity decay rate (the sum of the intrinsic and coupling rate), $\omega_\mu = \omega_0 + D_1\mu + \frac{D_2\mu^2}{2}$ is the frequency of the cavity eigenmodes in which $D_1 = 2\pi FSR$ and D_2 is the difference between two neighboring FSRs at the pump frequency ω_0. $s = \sqrt{P_{in}/\hbar}$ is the amplitude of P_{in} and $\delta_{\mu 0}$ is the Kronecker delta. The nonlinear coupling coefficient is

$$g = \frac{\hbar\omega_0^2 c n_2}{n_0^2 V_{eff}} \quad (3.46)$$

The set of equation can be rewritten in a dimensionless way [86]:

$$\frac{\partial a_\mu}{\partial \tau} = -(1 + i\zeta_\mu)a_\mu + i \sum_{\mu' \leq \mu''} (2 - \delta_{\mu'\mu''})a_{\mu'} a_{\mu''} a^*_{\mu'+\mu''-\mu} + \delta_{0\mu} f \tag{3.47}$$

where

$$a_\mu = A_\mu \sqrt{\frac{2g}{\kappa}} e^{-i(\omega_\mu - \omega_p - \omega D_1)t} \tag{3.48}$$

and

$$f = s\sqrt{\frac{8\eta g}{\kappa^2}} \tag{3.49}$$

$$\zeta_\mu = \frac{2(\omega_\mu - \omega_p - \mu D_1)}{\kappa} = \zeta_0 + d_2\mu^2 \tag{3.50}$$

and the coupling strenght is $\eta = \kappa_{ext}/\kappa$, $d_2 = D_2/\kappa$, $\tau = \kappa t/2$. The steady state when no sidebands are excited can be described by

$$f^2 = (\zeta_0 - |a_0|^2)^2 |a_0|^2 + |a_0|^2 \tag{3.51}$$

where a_0,$a_{+\mu}$ and $a^*_{-\mu}$ are respectively pump, signal and idler mode. In order to find the mode numbers of the first line generated at the parametric threshold [87], a set of characteristic equation for parametric sideband of the three mode system is considered

$$\frac{\partial a_{+\mu}}{\partial \tau} = -(1 + i\zeta_\mu - 2i|a_0|^2)a_{+\mu} + ia_0^2 a^*_{-\mu} \tag{3.52}$$

$$\frac{\partial a^*_{-\mu}}{\partial \tau} = -(1 - i\zeta_\mu + 2i|a_0|^2)a_{-\mu} - ia_0^{*2} a_{-\mu} \tag{3.53}$$

with eigenvalues:

$$\lambda = -1 \pm \sqrt{|a_0|^4 - (\zeta_\mu - 2|a_0|^2)^2} \tag{3.54}$$

The threshold of the parametric frequency convertion [86], at which the gain of the sidebands excited is equal to the cavity decay rate, is

$$P_{th} = \frac{\kappa^2 n_0^2 V_{eff}}{8\eta\omega_0 c n_2} \tag{3.55}$$

and the gain of the sidebands [88], for $P_{pump} > P_{th}$, can be written as

$$G = \sqrt{\kappa^2(\frac{P_{abs}}{P_{th}})^2 - 4\left(\omega_0 - \omega_p + \mu^2 D_2 - \kappa\frac{P_{abs}}{P_{th}}\right)^2} \tag{3.56}$$

where P_{abs} is the power absorbed by the cavity. At threshold ($G = \kappa$) from Eq.(3.56) we can obtain

$$\sqrt{\frac{f^2}{|a_0|^2 - 1}} - d_2\mu_{th}^2 + |a_0|^2 - \sqrt{|a_0|^4 - 1} = 0 \tag{3.57}$$

The relative mode number difference of the primary sidebands is

$$\mu_{th} = \sqrt{\frac{\sqrt{f^2 - 1} + 1}{d^2}} = \sqrt{\frac{\kappa}{D_2}\left(\sqrt{\frac{P_{in}}{P_{th}} - 1} + 1\right)} \tag{3.58}$$

and the minimum $\mu_{th,min} = \sqrt{\kappa/D_2}$, achievable when $P_{th} = P_{in}$, depens only on the decay rate κ and the second order dispersion D_2. The same parameters we can derive for the generation of secondary sidebands (μ'' and μ''') via a non-degenerate four-wave mixing process of the pump ($\mu = 0$) and the primary sideband μ' starting from a set of equation analogous to (3.52) and (3.53):

$$\frac{\partial a_{\mu''}}{\partial\tau} = -(1 + i\zeta_{\mu''} - 2i|a_0|^2 - 2i\left|a_{\mu'}\right|^2)a_{\mu''} + 2ia_0 a_{\mu'} a^*_{\mu'''} \tag{3.59}$$

$$\frac{\partial a^*_{\mu'''}}{\partial\tau} = -(1 - i\zeta_{\mu'''} + 2i|a_0|^2 + 2i\left|a_{\mu'}\right|^2)a^*_{\mu'''} - 2ia_0^* a^*_{\mu'} a_{\mu''} \tag{3.60}$$

where the influence of other excited lines is neglected. These frequency combs result to be useful in application where high repetition rate and

(>10GHz spacing between lines) and high power per line (>100μW) is desirable, such as spectrometer calibration [89], spectroscopy [90] and telecomunication [91]. The theory of generation of frequency combs in silica microsphere has been described in 2010 by Chembo et al. [87].

3.4 Article 1: Stimulated anti-Stokes Raman scattering resonantly enhanced in silica microsphere

3.4.1 Abstract

Efficient stimulated anti-Stokes Raman scattering has been observed in silica microspherical resonators pumped by CW laser. This process is observed in the normal dispersion regime. The lack of correlation between stimulated antiStokes and Stokes scattering spectra indicates that the signal has to be resonant with the cavity.

3.4.2 Introduction

Stimulated nonlinear optical processes, including Brillouin and Raman scattering, have been observed at ultralow threshold powers in whispering gallery mode silica microresonators [92, 94],crystalline microresonators [95, 97],polymer-coated silica microresonators [135] and in liquid microdroplets [99, 103].Stimulated anti-Stokes Raman scattering (SARS) have been observed in single-component microdroplets with strong Raman gain [104] and from minority species in multicomponent microdroplets with low Raman gain [105], in the latter, external seeding at the Stokes frequency was used to enhance the SARS signal. Stimulated Raman scattering (SRS) and stimulated Brillouin scattering (SBS) are pure gain processes and, therefore, both processes are automati-

cally phase-matched. However, SARS does require phase matching, in order to be efficiently generated and it is threshold less. The nonlinear polarization of the anti-Stokes wave, P_{as}^{NL} ,is defined by the relation:

$$P_{as}^{NL} = \chi^{(3)} E_P^2 E_S^* e^{i(2k_P - k_S)z} \tag{3.61}$$

where E_P and E_S are the amplitude of the pump and Stokes waves, respectively, χ^3 the third-order nonlinear susceptibility, and k_i are the propagation vectors for the pump, and Stokes waves [104, 105]. Whispering gallery mode resonators (WGMR) provide huge advantages for SRS generation, especially ultralow thresholds [92]. Thus, SRS has been extensively observed and studied in WGMR, but not SARS. SARS, like CARS, is a four-wave mixing (FWM) process, where the beating frequency between the pump and the anti-Stokes (or Stokes) waves matches a vibrational transition of the medium. In this Letter, we present cavity resonantenhanced SARS generation, multiorder SARS, and third-order nonlinear processes in silica WGMR at any dispersion value [106, 108]. The cavity-enhanced SARS emission has a linewidth similar to that of SRS and the pump, and a high-quality mode [109].

3.4.3 Experimental setup and results

Microspheres can be easily fabricated directly on the tip of a standard telecom fiber. In order to obtain micro-spheres below the fiber diameter, we melt the end of a half-tapered fiber, obtained by heating and stretching the fiber itself until it breaks. For this purpose, we used a fiber fusion splicer. Using a sequence of arc discharges, we can fabricate spheres down to about 25μm controlling their size down to about one percernt of their diameter [110]. The residual fiber stem is mounted on a translation stage with piezoelectric actuators and a positioning resolution of 20 nm. The diameters of the micro-

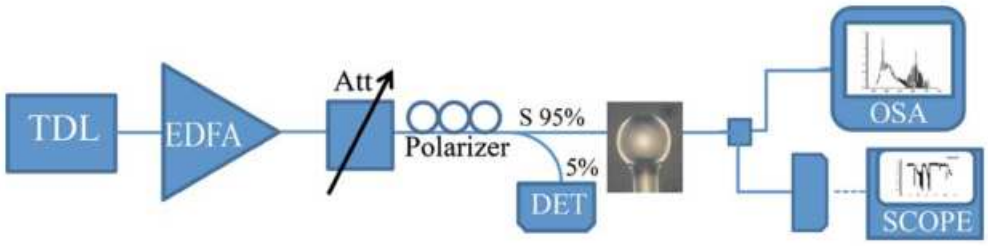

Figure 3.4: Experimental setup.

spheres used in these experiments range from a minimum diameter of about 25 μm up to a maximum diameter of about 160 μm. The corresponding Q factors are $5 \cdot 10^6$ (linewidth $\gamma = 40$ MHz) and 10^7 (linewidth $\gamma = 20$ MHz). The experimental setup is shown in Fig.(3.4). The laser light from a tunable diode laser (TDL) is amplified with an erbium-doped fiber amplifier (EDFA) and, after passing a polarization controller, is coupled to the equator of WGMR by means of a tapered fiber, produced in-house too. The laser is tuned into a resonance from high to low frequencies, which results in thermal self-locking [111] of the WGMR mode to the pump laser. SRS, SARS, and Raman family modes were detected on an optical spectrum analyzer (OSA, ANDO AQ6317B), directly transmitted by the taper fiber. All experimental results have been obtained for a similar launched pump power of about 80 mW.

Figure 3.5 shows SARS and the multiorder SRS spectrum of a silica microsphere of about 25 μm diameter. The pump laser is centered at 1571.8 nm, the first order Stokes component red-shifted by 347 cm^{-1} approximately, and the anti-Stokes component blue-shifted by 347 cm^{-1}, corresponding to one of the higher Raman gain modes of fused silica. The other SARS peak at 437 cm^{-1} observed in Figure 2 is not the result of a cascade process, but a first-order transition corresponding to the Raman gain band centered at 463 cm^{-1}.

The two symmetric sidebands of the anti-Stokes line centered at 437 cm^{-1}

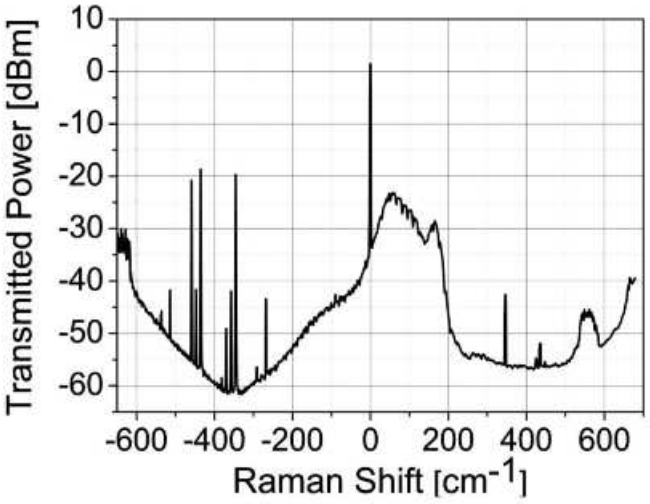

Figure 3.5: Experimental spectrum of SARS and SRS in a microsphere of 25 μm diameter.

are the result of a FWM process involving a nonresonant (electronic) $\chi^{(3)}$ [108]. They are centered at 426 cm^{-1} and 448cm^{-1}. Figure 3.6 shows a process with equally separated SARS and SRS modes (about 245 cm^{-1}) for a microsphere of about 40 μm of diameter, pumped at 1544 nm. The other SRS modes are first-order transitions that correspond to the Raman bands centered at 463 cm^{-1} and 790 cm^{-1}, not to cascaded SRS. Similar results were obtained by pumping a microsphere of diameter ranging from 45 to 98 μm at 1550 nm. It is worth to mention that in our experiments we measured different frequency shifts that correspond to the four largest component positions of the Raman gain (ν_1= 463 cm^{-1},ν_2= 362.5 cm^{-1},ν_3= 231.25 cm^{-1}, ν_4= 497 cm^{-1})[112].

The above mentioned results have been achieved in the regime of normal dispersion [113, 106, 107], in contrast with well-established theoretical models [114, 115], which only predicted FWM and modulation instabilities in resonators with anomalous dispersion. This occurrence is due to the cavity boundary conditions that introduce an additional degree of freedom: the frequency detuning of the pump from the eigenmode of the nonlinear res-

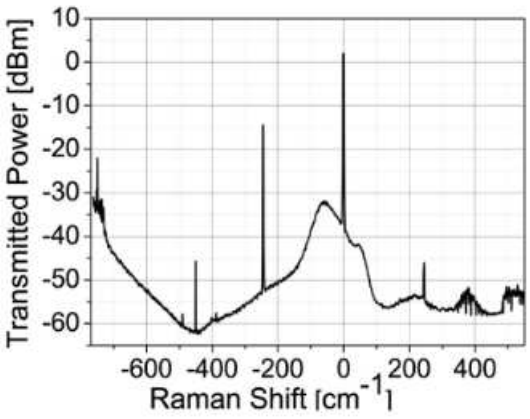

Figure 3.6: Experimental spectrum of anti-Stokes–Stokes lines in a microsphere of 40 μm diameter.

onator [106, 116]. The Kerr effect induces a negative nonlinear frequency shift of about 30 MHz in the position of the resonant frequency in our experiments, whereas the thermo-optic frequency shift is larger. However, these shifts only change mildly the free spectral range of the resonator [106] and in consequence the linear dispersion, calculated as the variation of the free spectral range [117].

Figure 3.7 shows a SARS spectrum from a silica micro- sphere of 85 μm of diameter. Also in this case, we have observed first-order transitions that correspond to the Raman bands centered at 362, 497, and 930 cm^{-1} (large peaks around 600 cm^{-1}, 750 cm^{-1} , and 900 cm^{-1} are due to OSA artifacts).

We also tested larger microspheres, with a diameter of about 160 μm, for two different pump wavelengths, one at 1553 nm and two at 1537 nm, in the regime of anomalous dispersion and of compensated dispersion according to [114].

Figure 3.8. shows an almost continuous comb with a SARS line more efficient than the corresponding SRS line in the compensated regime.

Figure 3.9 shows the anomalous dispersion regime with the pump centered at 1553 nm.

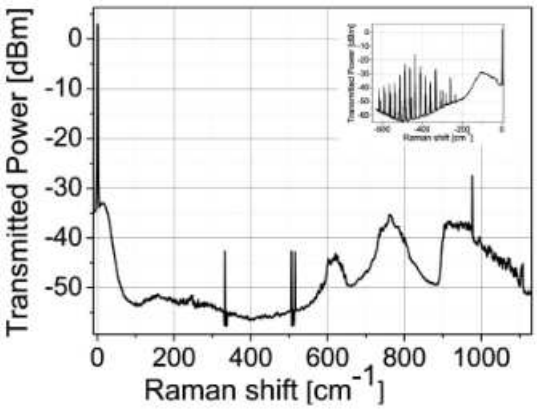

Figure 3.7: Experimental spectrum of a silica microsphere of 85 μm, showing multiorder SARS. Inset: correspondent SRS family modes.

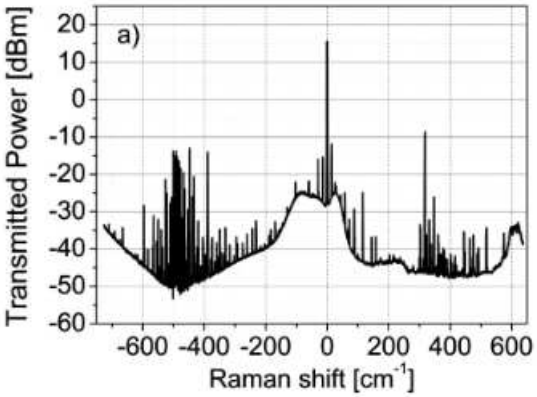

Figure 3.8: Experimental spectra of a 160 μm diameter: strong anti-Stokes-lasing

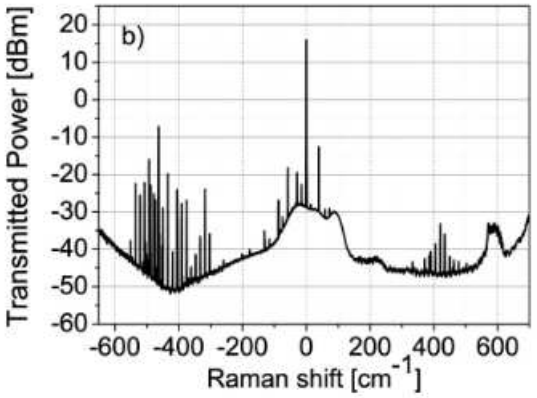

Figure 3.9: Experimental spectra of a 160μm diameter microsphere: sparse combs.

In this regime, three distinct spectral regions can be distinguished: a SARS family modes, a SRS one, and FWM in the vicinity of the pump. In these cases, the spectral broadening towards the longer wavelengths is provided by SRS, and the broadening to the shorter wavelengths is provided by biharmonic pumping (FWM among the pump and the multiorder SRS) resulting in SARS. The lack of continuity in all spectra indicates the nonsolitonic nature of the spectral broadening. Some features of the experimental spectra shown in here (unusually strong anti-Stokes components and extraordinarily symmetric spectra) cannot be explained by SRS only, mainly because the SRS gain spectrum is antisymmetric: only the Stokes waves undergo exponential gain, whereas the anti-Stokes waves are exponentially absorbed [74]. The anti-Stokes Raman components are known to be coupled to the Stokes Raman ones [74, 75], even for large dispersion. This coupling results in the growth of the anti-Stokes wave along the micro-sphere in direct proportion to the Stokes wave through an effectively phase-matched hyperparametric process. For a perfect phase matching condition, each eigensolution is seen to be an equal combination of Stokes and anti-Stokes components with a power ratio of one. In the opposite condition, the Stokes and anti-Stokes components are effectively decoupled.

In an intermediate case, when the phase mismatch gradually deviates from zero, the ratio between antiStokes and Stokes powers of the first Raman order is given by the following equation [25]:

$$\frac{P_a}{P_S} = \left| \frac{\gamma q P}{2\gamma q P + \beta_2 \Omega^2} \right|^2 \tag{3.62}$$

where P is the cavity build-up pump power, $\Omega/2\pi$ is the frequency shift between the pump and the first Raman order, β_2 is the linear dispersion calculated as the variation of the free spectral range, γ is the nonlinearity coefficient and $q = (1-\alpha) + \alpha\chi^3 = 0.82 + i0.25$, is a complex number that depends on the Raman susceptibility of silica and on the fractional contri-

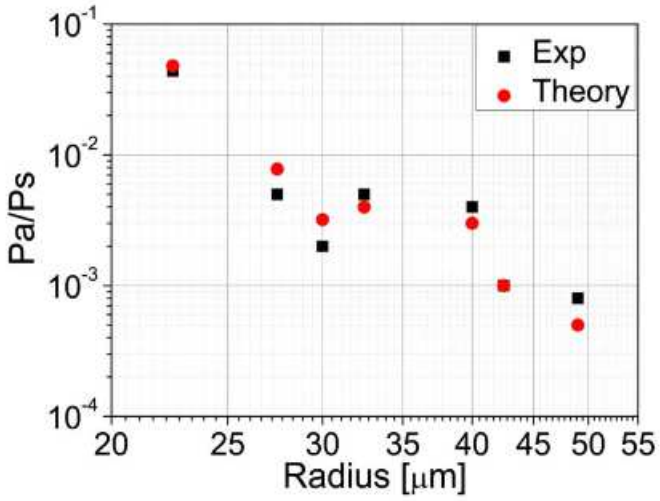

Figure 3.10: P_a/P_S ratio in log–log scale: experimental (solid black squares) and calculated values (solid red circles).

bution of the electronic susceptibility to the total nonlinear index [77, 109]. This expression is valid for both regimes, normal and anomalous, as far as the linear dispersion $\Delta k = \beta_2 \Omega^2$ is large. The values obtained from Eq. 3.62 are in close agreement with the experimental ones, given the uncertainties in β_2 and γ, as it can be seen in Fig. 3.10.

3.4.4 Conclusion

In conclusion, SARS has been observed in silica micro- spheres in the regime of normal dispersion. SARS is always detected in presence of SRS, and never in the absence of SRS, in agreement with the theory of Bloembergen and Shen [118]. SARS intensity is specially enhanced when SARS frequency is resonant with a cavity mode and phase matched with the pump and the SRS signal. Resonant SARS and SRS corresponding to different Raman bands were also observed.

3.5 Article 2: Generation of hyper-parametric oscillations in silica microbubbles

3.5.1 Abstract

Cavity resonant enhanced stimulated Raman scattering (SRS), four-wave mixing, and broadband hyper-parametric oscillation in silica microbubble whispering gallery mode resonators (WGMR) in forward and backward directions are reported in this Letter. We show that microbubbles can operate not only in a highly ideal two-photon emission regime, but also generate combs, both natively and multimode spaced. The nonlinear process is phase matched because of the interaction of different mode families of the resonator.

3.5.2 Introduction

Whispering gallery mode resonators (WGMR) strongly enhance light-matter interactions because of their extraordinarily high quality factors and small mode volumes. Based on these unique properties, a huge variety of nonlinear optical processes has been observed in WGMR [143, 120, 121]. Coupling conditions also play a very important role in favoring one type of nonlinear process over another [88]. Pure gain processes, such as stimulated Brillouin scattering (SBS) and stimulated Raman scattering (SRS), are automatically phase matched [74, 100, 145]. SBS bulk gain is much greater than SRS gain; however, SBS is difficult to observe in WGMR, mainly because of the fact that there could be no whispering gallery mode (WGM) present at the Brillouin offset to support the Stokes component [122, 123]. SRS is then the easiest nonlinear process related to third-order susceptibility χ^3 to be generated in WGMR [108]. It often competes with optical (hyper)-parametric oscillations, such as four-wave mixing (FWM), which has a higher gain but stringent phase matching conditions [88, 92]. This constraint could limit the spectral

band of the parametrical oscillations. Usually, the phase matching condition can be obtained by using higherorder modes [120, 121] or WGMR with huge tuning ranges, such as microbubble and microbottle resonators [124, 125, 126]. In this Letter, we present cavity resonant enhanced SRS, FWM, and broad hyper-parametric oscillation in silica microbubble resonators (MBR) in forward and backward directions. Here, all nonlinearities are related to the third-order susceptibility χ^3 because of the inversion of symmetry that silica exhibits. The observed Raman anti-Stokes spectrum shows two sidebands that resemble that of modulation instability [96].

3.5.3 Experimental setup and results

The MBRs were fabricated from slightly pressurized silica capillaries using a modified fusion splicer, where the electrodes could rotate by 360° to obtain uniform heating of the capillary. The detailed fabrication and characterization procedure can be found in [125, 61]. Figure 3.11(a) shows an optical image of a MBR fabricated with this method, which was created from a capillary with an ID of 200 μm OD of about 280 μm (Postnova Z-FSS200280 capillary).

The diameters of the microbubbles used in these experiments range from a minimum diameter of about 420 μm to a maximum diameter of about 475 μm with wall thicknesses ranging from 3 to 4 μm 0.5 μm. The Q values were obtained by measuring the resonance linewidth of the excited WGM modes. The corresponding quality factors Q are about $3.5x10^7$ [Fig.3.11(b)].The experimental setup is shown in Fig. 3.11(c). The laser light from a tunable diode laser (TDL) is amplified with an erbium doped fiber amplifier (EDFA), and, after passing an attenuator (ATT) and a polarization controller (PC), is coupled to the equator of a MBR by means of a tapered fiber, produced in-house, too. The laser is tuned into a resonance from high to low frequen-

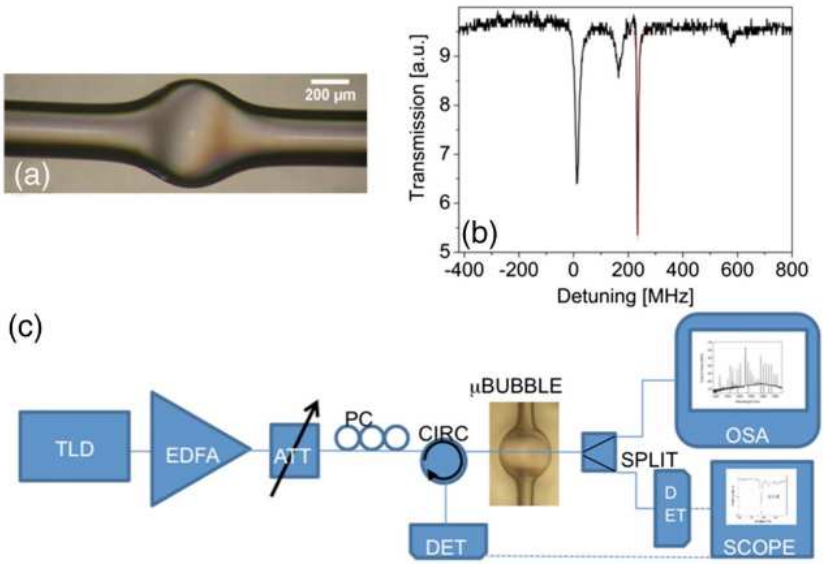

Figure 3.11: (a) MBR with OD ∼475 μm and wall thickness ∼4 μm, created from a capillary with ID ∼200 μm and OD ∼280 μm. (b) Resonance spectrum of MBR. The red line is the Lorentzian fit of a resonance. (c) Experimental setup.

cies, which results in thermal self-locking [111] of the WGMR mode to the pump laser. A splitter at the end of the taper sends part of the signal into an optical spectrum analyzer (OSA) and part to a photo-detector and oscilloscope (TEKTRONIX). The backward directed spectra have been collected through a circulator (CIRC) placed at the input of the taper, after the polarization control. SRS, Raman family modes, FWM, and combs were detected on an OSA (ANDO AQ6317B), directly transmitted by the taper fiber. The maximum launched pump power is about 80 mW. Figure 3.12(a) shows a degenerate FWM of the laser pump in a MBR with a diameter of about 475 μm, coupled into the forward direction of the tapered fiber. It can be seen that the idler–signal emission ratio is near unity. The pump wavelength is centered at 1558,4 nm, the idler at 1557,3 nm, and the signal at 1559,5 nm. The signal and idler are spaced by twice the free spectral range (FSR).

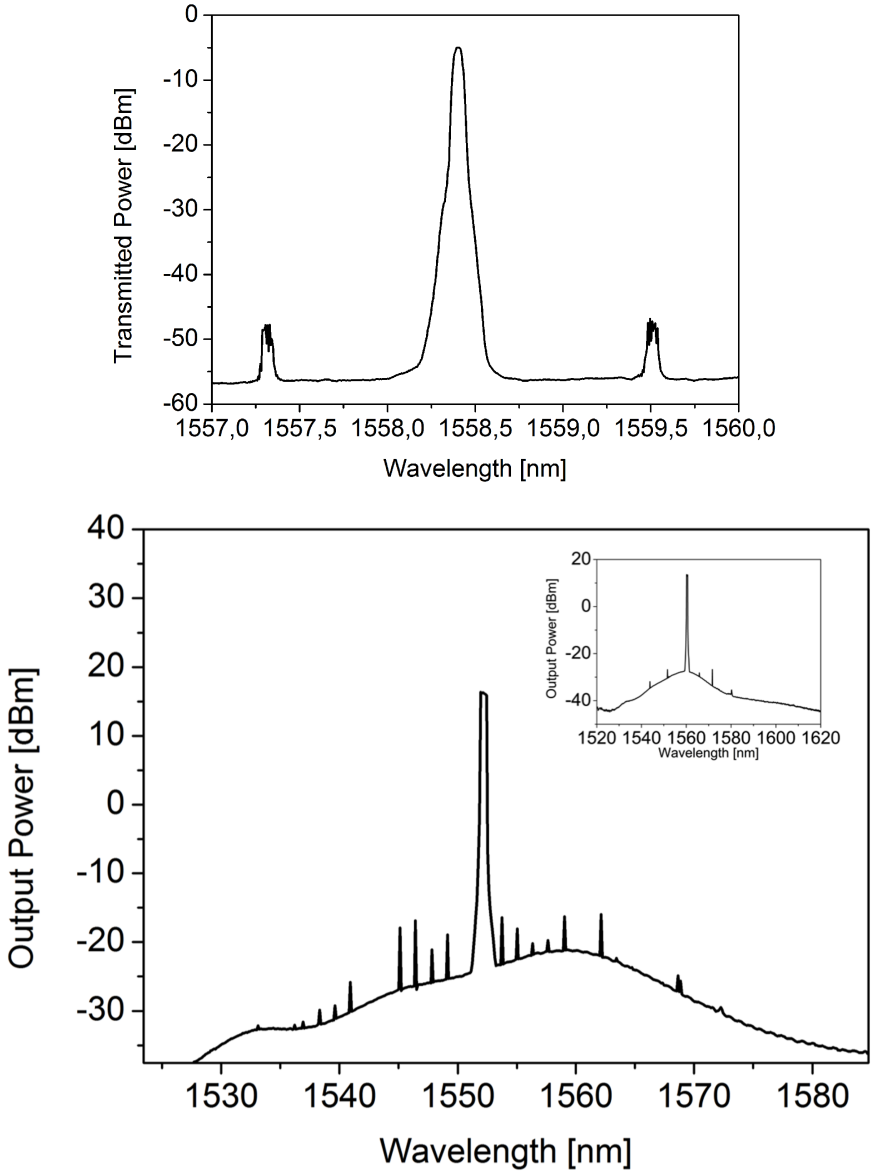

Figure 3.12: (a) Experimental spectrum measured for a microbubble with a diameter of about 475 μm. It shows a FWM parametric oscillation at 1558,4 nm; the signal and idler are spaced by twice the FSR (2 x 1.1 nm). (b) Experimental spectra of a 475 μm diameter MBR with a frequency offset of one FSR. Inset: experimental spectra of the same microbubble with a frequency offset of 5 FSR.

By increasing the pump power and/or slightly tuning the pump wavelength, cascaded FWM can occur. Figure 3.12(b) shows two examples of a regime where multiples of FSR have been selected as preferential sidebands. We have realized a "Type I" comb [127], or a natively mode spaced comb [85] with sidebands separated by one FSR [Fig. 3.12(b)], and, by tuning the pump frequency, a "Type II" [127], or multimode spaced comb [85] with sidebands, separated from the pump by several FSR [Fig. 3.12(b) inset]. Figure 3.12(b) shows a sparse hyper-parametrical oscillation with a frequency offset at one FSR when the MBR is pumped at 1560,34 nm (Type I), whereas the inset shows an oscillation with two pairs of frequency side bands centered at 1552,13 nm with a frequency offset at 5 times the FSR (Type II). In the Type I comb, there are more anti-Stokes than Stokes frequencies. The Stokes line in the inset of Fig.3.12(b), centered at about 1580 nm, is a first-order transition that corresponds to the Raman band centered at 100 cm^{-1} and does not have a corresponding anti-stokes line. Stimulated anti-Stokes Raman Scattering (SARS) intensity is specially enhanced when SARS frequency is resonant with a cavity mode and phase matched with the pump and the SRS signal [128]. Figure 3.13 shows an aperiodic, but broader, hyper-parametrical oscillation centered at 1552,64 nm in the backward direction.

The FWM pairs in the vicinity of the pump are separated by one FSR; different SRS family modes are generated at about 14 THz from the pump and an intensity envelope around the anti-Stokes frequencies which resembles a modulation intensity. [96] In this case, the anti-Stokes side of the spectrum is denser than the Stokes side. This result is similar to that obtained in [121], where it was explained that the probability of optimal conditions for the FWM increases in the blue side of the spectrum because of the increase of the Q-factor and the WGM density in that side of the spectrum. The left inset of Fig. 3.12 shows the details of the anti-Stokes comb around 1508 nm. In this case, the intensity of the antiStokes component is high enough to

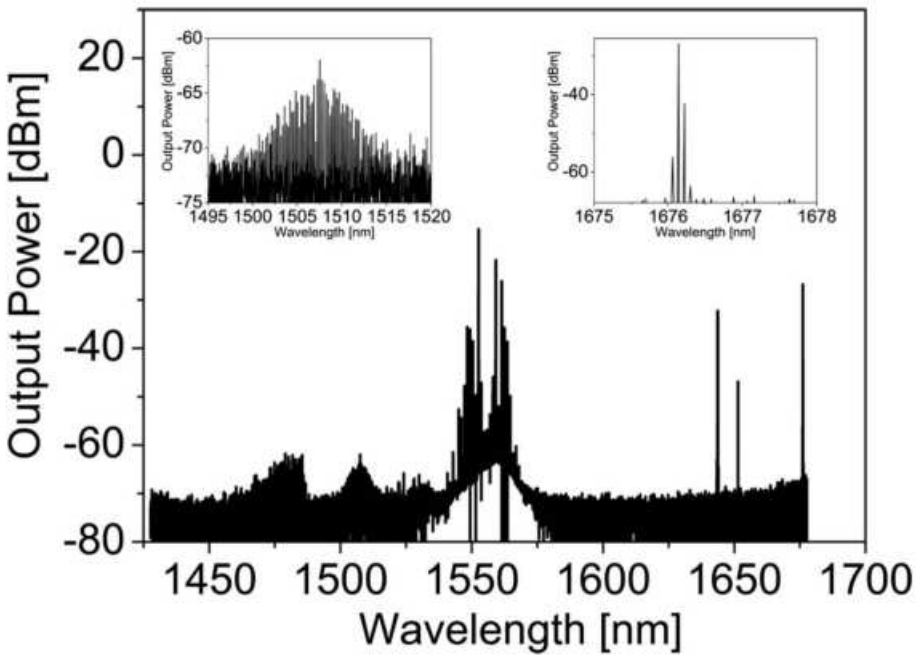

Figure 3.13: Aperiodic hyper-parametric oscillation with different spacing; FWM in the vicinity of the pump spaced by azimuthal FSR, SRS family modes, and intensity envelope spectrum at anti-Stokes frequency. Insets: (left) anti-Stokes frequency comb spectrum with a frequency offset of twice the FSR_p(1 x 0,12nm),and (right) SRS family modes separated one FSR_p.

generate its own parametrical oscillation, with a separation smaller than the FSR of the cavity. This can be explained by the geometrical characteristics of a MBR. MBRs are spheroidal WGM resonators with quite dense spectral characteristics [126]. A spheroidal WGMR has two nearly equidistant mode families characterized by their respective azimuthal (characterized by the quantum number l) and vertical (characterized by the quantum number p) FSR [124, 128]. The vertical FSR is proportional to the azimuthal FSR_l in the following way: $FSR_p = FSR_l(R-r)/r$ where R and r are the semi-axes of the spheroid, being $r < R$ the shorter semi-axis of the spheroid [129, 121]. The Stokes components are not single SRS laser lines, but a set of different lines separated by one FSR_p, which is about to 0,12 nm (right inset of Fig. 3.13). Based on the presence of FSR , we assume that these mode families (same azimuthal, but different vertical quantum number) have a good spatial overlap and interaction among them, giving as a result of their interaction, different frequency spacing and an asymmetric spectrum [121]. We have evaluated the second-order dispersion of the MBR for both radii at the wavelength of interest as the variation of the FSR. We have used an expansion from Gorodetsky and Fomin [130] to numerically calculate the geometric dispersion in a cold spheroid. Gorodetsky and Fomin used a quasi-classical method and obtained the following approximation for the resonant frequencies ν:

$$\nu(l) = \frac{c}{2\pi Rn}\left[l - \alpha_q\left(\frac{l}{2}\right)^{\frac{1}{3}} + \frac{2p(R-r)+R}{2r} - \frac{\chi n}{\sqrt{n^2-1}} + \right.$$
$$\left. + \frac{3\alpha_q^2}{20}\left(\frac{l}{2}\right)^{-\frac{1}{3}} - \frac{\alpha_q}{12}\left(\frac{2p(R^3-r^3)+R^3}{r^3} + \frac{2n\chi(2\chi^2-3n^2)}{(n^2-1)^{\frac{3}{2}}}\right)\left(\frac{l}{2}\right)^{-\frac{2}{3}}\right]. \tag{3.63}$$

where p is the vertical quantum number, l is the azimuthal quantum number, q an integer mode index (q = 1 for the fundamental mode family),

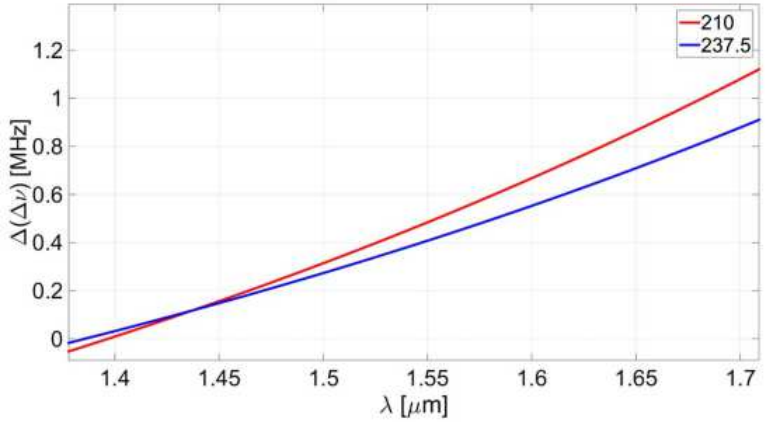

Figure 3.14: Total dispersion of a cold MBR for two different radii: 210 (red) and 237.5 (blue) μm.

α_q are the negative q_{th} zeros of the Airy function ($\alpha_1 = -2.34$ is the first zero of the Airy function), n is the refraction index for fused silica (n = 1.45), and $\chi = 1$ for quasi-TE modes and $\chi = 1/n^2$ for quasi-TM modes. The geometrical dispersion is normal and large, with values of several hundreds of kHz. However, the material dispersion is quite large at the wavelengths considered in this Letter. We calculated the refractive index that is frequency dependent using the Sellmeier equation for silica. The total dispersion is anomalous and large, also with values of several hundreds of kHz. Figure 3.14 shows the calculated total dispersion for two cold MBRs used in this work, one with a diameter of 420 μm and the other one for the diameter of 475 μm.

The Kerr effect induces a negative nonlinear frequency shift that can be calculated from

$$\Delta\nu_{res} \approx -\nu_{res}\frac{n_2}{n^2}\frac{c}{4\pi^2 R A_{eff}}\frac{N}{\gamma}P_{in} \tag{3.64}$$

where n_2 is the nonlinear refractive index (n_2 is $2.2 \times 10^{-20} m^2\ W^{-1}$ A_{eff} is the effective area, γ is the linewidth of the resonance, N is the peak power enhancement, and P_{in} in for silica), A_{eff} is the launched power into the MBR.

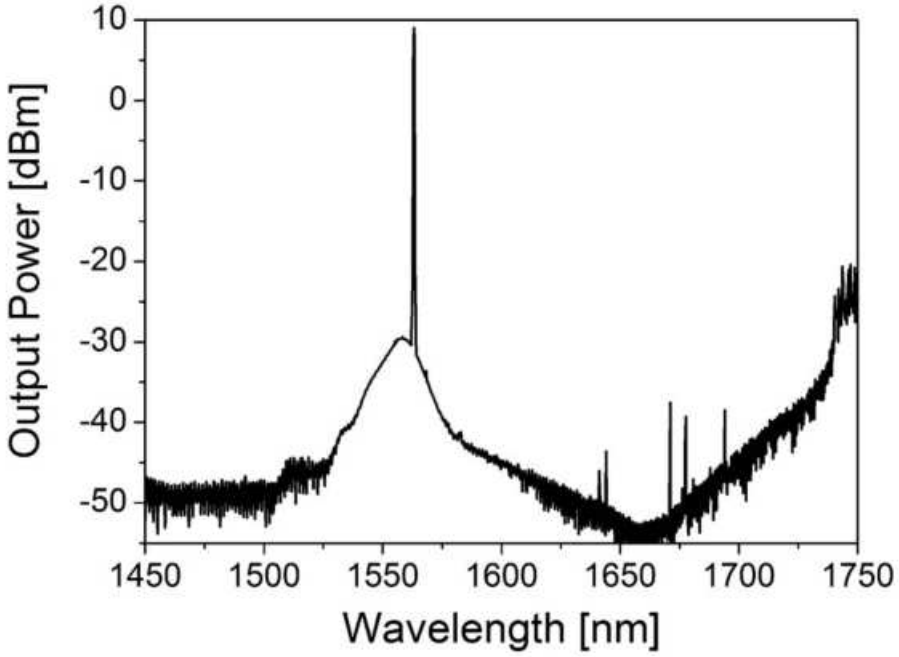

Figure 3.15: Experimental spectrum of a 420 μm MBR showing different SRS lines in the forward direction.

In our experiment, the Kerr shift is about 300 MHz for a 475 μm diameter MBR without peak power enhancement. The total variation induced into the dispersion will be about 600 Hz into a dispersion of about 500 kHz (Fig. 3.14). The thermo-optic effect will induce larger shifts, but these effects will change mildly the FSR [86], and, in consequence, the linear dispersion that is calculated as the variation of the FSR. For a MBR of about 420 μm of diameter, the only nonlinear phenomenon observed was SRS (Fig. 3.15). In this case, the separation between the pump and the SRS line is about 110 nm which corresponds to the 460 cm^{-1}(13.5 THz) line of the silica Raman gain [131].

Even though it has been proved that, in smaller resonators, SRS competes with FWM [132], we think that in the 420 μm resonator the coupling condition is responsible for the decrease of FWM efficiency. The difference between the two diameters is too small in our case to have important changes

in the density of the modal spectra. Dispersion is also so similar between the two MBRs that it is difficult to favor one regime over the other.

3.5.4 Conclusion

We have observed a variety of nonlinear processes related to the third-order susceptibility χ^3 such as SRS, FWM, and frequency combs in silica microbubble resonators when pumped with a CW laser. The repetition rate of the antiStokes frequency comb is not an integer number of the FSR, indicating the interaction of family modes with the same azimuthal number l and different polar order. Different from [132], we have not observed the anchorage of the first sideband close to the pump, in correspondence to the mode crossing. For these reasons, we have excluded linear mode interaction or mode coupling [133, 134]. The hyper-parametric oscillations are much broader than the only case published up to now [135]. The results obtained here can pave the way for molecular spectroscopy, active sensing, and last, but not least, generation of quantum correlated photon pairs at room temperature.

Chapter 4

Optical Frequency Conversion in silica microspheres

4.1 Third order sum frequency and third harmonic generation

Third-order sum-frequency generation (TSFG) has been studied in WGM structures, in particular in liquid droplets, starting from 1989 [136, 137, 138]. TSFG is a weak process, even when condictions are optimized the emission is only 10^{-4} times as strong as the SRS. A model for TSFG in spherical dieletric micoresonators can be based on the work of Chew et al [139] for emission from a polarization source whithin a sphere.

TSFG results from the nonlinear polarization [140]:

$$\mathbf{P}^{NLS}(\mathbf{r},\omega) = \chi^{(3)}\mathbf{E}_a(\mathbf{r},\omega_a)\mathbf{E}_b(\mathbf{r},\omega_b)\mathbf{E}_c(\mathbf{r},\omega_c) \tag{4.1}$$

where $\chi_{(3)}$ is the third-order susceptibility of the hosting material and $E(\omega_i)$ is the electric field amplitude at frequency ω_i. Energy conservation requires that $\omega_{TSFG} = \omega_1 + \omega_2 + \omega_3$. A particul case of TSFG is the third-harmonic generation (THG) in which the three input frequencies are degen-

erate and so $\omega_{TGH} = 3\omega_1$.

The polarization in (4.1) can be written as

$$\mathbf{P}^{NLS}(\mathbf{r},\omega) = D\sum_{jkl}\chi^{(3)}_{ijkl}E_a(\mathbf{r},\omega_a)E_b(\mathbf{r},\omega_b)E_c(\mathbf{r},\omega_c) \tag{4.2}$$

where j,k,l are the three orthogonal coordinate directions and D is the number of distinct permutation of ω_a, ω_b and ω_c. Being silica an isotropic material only three indipendent elements can be considered

$$\chi_{ijkl} = \chi_{1122}\delta_{ij}\delta_{kj} + \chi_{1212}\delta_{ik}\delta_{jl} + \chi_{1212}\delta_{il}\delta_{jk} \tag{4.3}$$

In spherical coordinates (r,θ,ψ), for the transverse electric field (TE) in a sphere, the radial component is zero and so the θ component of the polarization $\mathbf{P}^{NLS}(\mathbf{r},\omega)$ can be written as

$$P^{NLS}_{\theta} = \chi^{(3)}_{1111}(E_{a\theta}E_{b\theta}E_{c\theta}) + \chi^{(3)}_{1122}(E_{a\theta}E_{b\phi}E_{c\phi}) + \chi^{(3)}_{1212}(E_{a\phi}E_{b\theta}E_{c\phi}) + \chi^{(3)}_{1221}(E_{a\phi}E_{b\phi}E_{c\theta}) \tag{4.4}$$

where $\chi^{(3)}_{1111} = \chi^{(3)}_{1122} + \chi^{(3)}_{1212} + \chi^{(3)}_{1221}$. In the simplest case of THG $\chi^{(3)}_{1122} = \chi^{(3)}_{1212} = \chi^{(3)}_{1221}$ and so

$$\chi^{(3)}_{ijkl} = \chi^{(3)}_{1122}(\delta_{ij}\delta_{kj} + \delta_{ik}\delta_{jl} + \delta_{il}\delta_{jk}) \tag{4.5}$$

and the θ component of the polarization is

$$P^{NLS}_{\theta} = 3\chi^{3}_{1122}(E^3_{a\theta} + E_{a\theta}E^2_{a\phi}) \tag{4.6}$$

The radiations generated by the polarization $\mathbf{P}^{NLS}(\mathbf{r}',\omega)$, where $\mathbf{r}'$ is the source position, induce additional fields which have to satisfy the boundary conditions at the surface of the sphere. If $\mathbf{E}(\mathbf{r},\omega)$ are assumed to slowly vary in time, the total power radiated from the sphere can be written

$$P(\omega) = \frac{c}{8\pi k^2} \sum_{n,m} \left[\left| f_n \int a_E(n,m) d^3r' \right|^2 + \left| g_n \int a_M(n,m) d^3r' \right|^2 \right] \quad (4.7)$$

where

$$f_n = \frac{i/k_t a}{n(\omega)^2 j_n(k_t a) \left[x h_n^{(1)}(x) \right]' - h_n^{(1)}(x) \left[k_t a j_n(k_t a) \right]'} \quad (4.8)$$

$$g_n = \frac{i/k_t a}{j_n(k_t a) \left[x h_n^{(1)}(x) \right]' - h_n^{(1)}(x) \left[k_t a j_n(k_t a) \right]'} \quad (4.9)$$

in which j_n and h_n^1 are the spherical Bessel and Hankel functions and the primes $'$ indicate differentiation with respect to the argument. a is the sphere radius, $n(\omega)$ is the refractive index at ω, $x = \omega a/c$ is the size parameter and k_t is the wave number inside the sphere. The amplitude factor is given by

$$\int a_E(n,m) d^3r' = 4\pi k^2 \int \mathbf{P}^{NLS}(\mathbf{r}', \omega) \nabla' \times \left[j_n(k_t r') \mathbf{Y}^*_{nnm}(\theta', \phi') \right] d^3r' \quad (4.10)$$

$$\int a_M(n,m) d^3r' = 4\pi i k^3 \int \mathbf{P}^{NLS}(\mathbf{r}', \omega) j_n(k_t r') \mathbf{Y}^*_{nnm}(\theta', \phi') d^3r' \quad (4.11)$$

where $\mathbf{Y}_{nnm}(\phi, \psi)$ is the vector spherical harmonic

$$\mathbf{Y}_{nnm}(\theta, \phi) = -i/\left[n(n+1) \right]^{1/2} \mathbf{r} \times \nabla Y_{nm}(\theta, \psi) \quad (4.12)$$

in which

$$Y_{nm}(\theta, \phi) = \left[\frac{(2n+1)(n-m)!}{4\pi(n+m)!} \right]^{1/2} P_n^m(cos\theta) e^{(im\phi)} \quad (4.13)$$

with the associated Legendre function $P_n^m(cos\theta)$.

If the three waves generating the TSFG are standing-waves then the output is also a standing wave. The SRS fields (TE) can be written as

$$\mathbf{E_s}(\mathbf{r},\omega_s) = A g_n j_n(k_t r)\left[\mathbf{Y}_{nnm}(\theta,\phi) + \mathbf{Y}^*_{nnm}(\theta,\phi)\right]/2 \tag{4.14}$$

where A is the amplitude factor proportional to $\sqrt{I_{SRS}}$ and they are labeled n_s and m_s with s is a, b and c. The power radiated into TE output mode, labeled n_3, m_3 is

$$\begin{aligned} P(\omega) &= \frac{c}{8\pi k^2}\left| g_{n_3}(\omega)\int a_M(n_3,m_3)d^3r'\right|^2 \\ &= 2\pi c k^4 \left|g_{n_3}(\omega)\right|^2 \left|\int \chi^{(3)}\left[A_a g_{n_a}(\omega_a) j_{n_a}(k_a r')\frac{\mathbf{Y}_{n_a n_a m_a}+\mathbf{Y}^*_{n_a n_a m_a}}{2}\right]\right. \\ &\qquad \times\left[A_b g_{n_b}(\omega_b) j_{n_b}(k_b r')\frac{\mathbf{Y}_{n_b n_b m_b}+\mathbf{Y}^*_{n_b n_b m_b}}{2}\right] \\ &\left.\times\left[A_c g_{n_c}(\omega_c) j_{n_c}(k_c r')\frac{\mathbf{Y}_{n_c n_c m_c}+\mathbf{Y}^*_{n_c n_c m_c}}{2}\right] j_{n_3}(k_t r')\mathbf{Y}^*_{n_3 n_3 m_3} d^3r'\right|^2 \end{aligned} \tag{4.15}$$

Obtaining the total power at ω requires the integration over all ω

$$P^T_{n_3 m_3} = \int_0^\infty P_{n_3 m_3}(\omega)d\omega \tag{4.16}$$

Finally, separatating the radial and angular contributions the power integrated over ω becomes

$$\begin{aligned} P^*_{n_3 m_3} &= 2\pi c k^4 A_a^2 A_b^2 A_c^2 \left|\int_0^a j_{na}(k_{at}r')j_{nb}(k_{bt}r')j_{nc}(k_{ct}r')j_{n_3}(k_t r')r'^2 dr'\right|^2 \\ &\times\left|\int\left[\chi^3\left(\frac{\mathbf{Y}_{n_a n_a m_a}+\mathbf{Y}^*_{n_a n_a m_a}}{2}\right)\left(\frac{\mathbf{Y}_{n_b n_b m_b}+\mathbf{Y}^*_{n_b n_b m_b}}{2}\right)\left(\frac{\mathbf{Y}_{n_c n_c m_c}+\mathbf{Y}^*_{n_c n_c m_c}}{2}\right)\right]\right. \\ &\left.\mathbf{Y}^*_{n_3 n_3 m_3} d\Omega\right|^2 \int_0^\infty \left|\int_{\omega_b=0}^{\omega}\int_{\omega_a=\omega-\omega_b}^{\omega} g_{n_a}(\omega_a)g_{n_b}(\omega_b)g_{n_c}(\omega_c)d\omega_a d\omega_b\right|^2 \left|g_{n_3}(\omega)\right|^2 d\omega. \end{aligned} \tag{4.17}$$

The TSFG power is proportional to the spatial overlap integrals as well as to a frequency overlap integral. The spatial one is over the sphere volume for the product of the fields of TSFG mode and the three generating modes.

4.2 Article 3: Optical Frequency Conversion in Silica-Whispering-Gallery-Mode Microspherical Resonators

4.2.1 Abstract

High quality factor whispering-gallery-mode microresonators are ideally suited for nonlinear optical interactions. We analyze, experimentally and theoretically, a variety of $\chi^{(3)}$ nonlinear interactions in silica microspheres, consisting of third harmonic generation and Raman assisted third order sum-frequency generation in the visible. A tunable, room temperature, cw multicolor emission in silica microspherical whispering-gallery-mode microresonators has been achieved by controlling the cavity mode dispersion and exciting nonequatorial modes for efficient frequency conversion.

4.2.2 Introduction

Whispering-gallery-mode resonators (WGMR) play an extremely important role in modern optics, being fundamental not only in many laser devices, but also as tools for very accurate frequency measurements and for nonlinear optics experiments as frequency conversion [142, 143]. The extraordinary high quality factors, up to 10^{11}, and the small volume modes make them an ideal device for shaping and enhancing light-matter interactions [88, 144]. Nonlinear wave generation at low power continuous wave (cw) is still one of the biggest challenges in nonlinear optics. Whispering-gallery-mode microresonators (WGMR) can be exploited for cw nonlinear frequency conversion due to their properties mentioned above. However, the high circulating intensities inside the WGMR are not a sufficient condition for efficient harmonic generation, parametric and hyperparametric oscillations: it requires fulfilling

phase and mode matching and energy conservation conditions [145, 57]. In the case of WGMR made of silica glass, which exhibits inversion of symmetry, second order nonlinear interactions are forbidden. Here, the elemental nonlinear interaction is due to third order susceptibility χ^3 effects, in which four photons are coupled. Previous work in this area, however, focuses on toroidal WGMR where most of the excitable modes are constrained to be the equatorial ones [146] or highly nonlinear materials [145, 147]. Efficient generation of visible light via third order sum-frequency generation (TSFG) or four wave mixing (FWM), and third harmonic generation (THG) in silica microspheres has not been effectively explored up to now. In this Letter we demonstrate tunable optical harmonic generation with extremely narrow linewidth in silica microspheres. The selection rules for silica microspherical WGMR have been obtained systematically taking into account spatial, radial, and angular mode overlaps and material and resonator dispersion profiles. This research is aimed to develop a room-temperature cw miniaturized visible laser source, tunable and narrow lined to study the possibility of using optical hyperparametrical oscillations for nonclassical light generation [147] and for developing interdisciplinary applications such as lab-on-a-chip biosensors. In the most general case of TSFG, three different waves interact with a nonlinear medium to generate a fourth wave of different frequency ($\omega_{TSFG} = \omega_1 + \omega_2 + \omega_3$). If the three input frequencies are degenerate, it will result in THG. In this case the energy conservation requires $\omega_{THG} = 3\omega_1$. The additional phase matching condition requires $n(\omega_{THG}) = n(\omega_p)$, which in general can be fulfilled, as linear and nonlinear dispersion can be compensated for by the dense distribution of degenerate WGMs with different polar number and decreasing effective index $n_{eff} = m/kR$[149]. In a WGMR, an additional boundary condition leads to a strict value for the resonant frequency, which may be in conflict with the strict energy conservation, meaning that ω_{TSFG} or ω_{THG} is out of resonance. The total TSFG power P^T emitted is proportional to

the overlap of the WGM eigenfunctions [Eq. (1)] [140]. These eigenfunctions are characterized by radial, azimuthal, and polar numbers, n, l, m and they are expressed, in spherical geometry, as a product of the spherical Bessel function $j_l(k_n r)$ and spherical harmonics $Y_{lm}(\theta, \psi)$.

$$P^T \propto \left| \int_0^R j_{l1}(k_{nl} r) j_{l2}(k_{n2}) j_{l3}(k_{n3} r) j_l^*(k_n r) r^2 dr \right|^2 \times \left| \int (\chi^3 Y_{l1m1} Y_{l2m2} Y_{l3m3}) Y_{lm}^* d\Omega \right|^2 \quad (4.18)$$

4.2.3 Experimental setup and results

Microspheres can be easily fabricated directly on the tip of a standard telecom fiber. In order to obtain microspheres below the fiber diameter we melt the end of a half-tapered fiber, obtained by heating and stretching the fiber itself until it breaks. For this purpose we used a fiber fusion splicer. Using a sequence of arc discharges we fabricated spheres down to about 25 μm in diameter controlling their size down to about 1% of their diameter [110]. The residual fiber stem is mounted on a translation stage with piezoelectric actuators and a positioning resolution of 20 nm. The experimental setup is shown in Fig. 4.1.

The light from a tunable diode laser (TDL) is amplified with an erbium-doped fiber amplifier (EDFA) and after passing a polarization controller is coupled to the WGMR by means of a tapered fiber, also produced in-house. The laser is tuned into a resonance from high to low frequencies, which results in thermal self-locking [111] of the WGMR mode to the pump laser. THG and TSFG signals were detected on an optical spectrum analyzer (OSA) or a spectrometer by collecting with a multimode fiber (MMF, 50 μm core, 0.2 NA), without coupling optics, the light scattered from the microsphere. Though the taper is not mode matched in the visible, a small portion of the

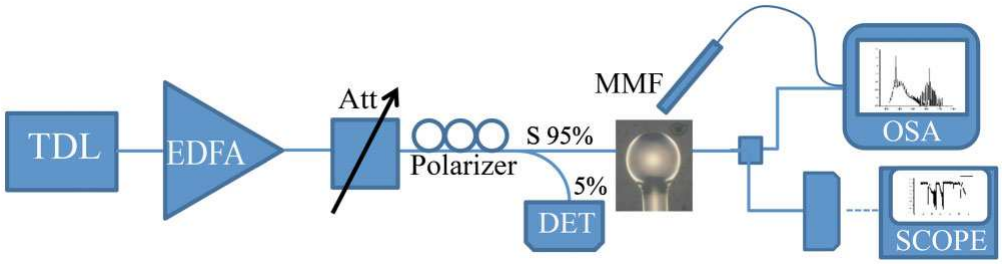

Figure 4.1: Scheme of the experimental setup. TDL: Tunable diode laser; EDFA: Erbium doped fiber amplified; Att: Attenuator; S: Splitter (95:5), DET: photodiode detector; MMF: multimode fiber; OSA: Optical Spectrum Analyzer; Scope: Oscilloscope.

signal is also coupled to the taper output and monitored on an OSA. A 3 dB splitter with one arm ending on a detector connected to an oscilloscope allows locating the resonance positions while scanning the laser. In order to fulfill the energy conservation condition we had to select the proper sizes for the microspheres. The geometrical dispersion for the fundamental WGM can be obtained by semi-analytical calculations [150]. We included linear material dispersion and calculated the optimum size of the spherical WGMR in which the dispersion is compensated, and the frequency mismatch $\Delta\nu = 3\nu_p - \nu_{THG}$ is close to zero. Indeed, Fig.4.2 shows the calculated linear dispersion for THG for the fundamental WGM modes defined as $\Delta\nu_{WGM} = (\nu_{WGMp} - \nu_{WGMTH}/3)$, i.e., the difference between the resonance position at the pump frequency and the closest resonance around the corresponding TH frequency divided by three. The dispersion curve is calculated in the range 25–40 μm for the sphere ray. We considered this range as a good compromise for keeping a high-Q (around 10^7: in fact the Q value decreases with microsphere size because of scattering [151]) and having at the same time high power density (cavity buildup factor and mode areas both decrease with R, so the intensity decreases with R [92]). Then, taking into account that the pump wavelength bandwidth is limited by the erbium gain band (1530–1570 nm), we obtained

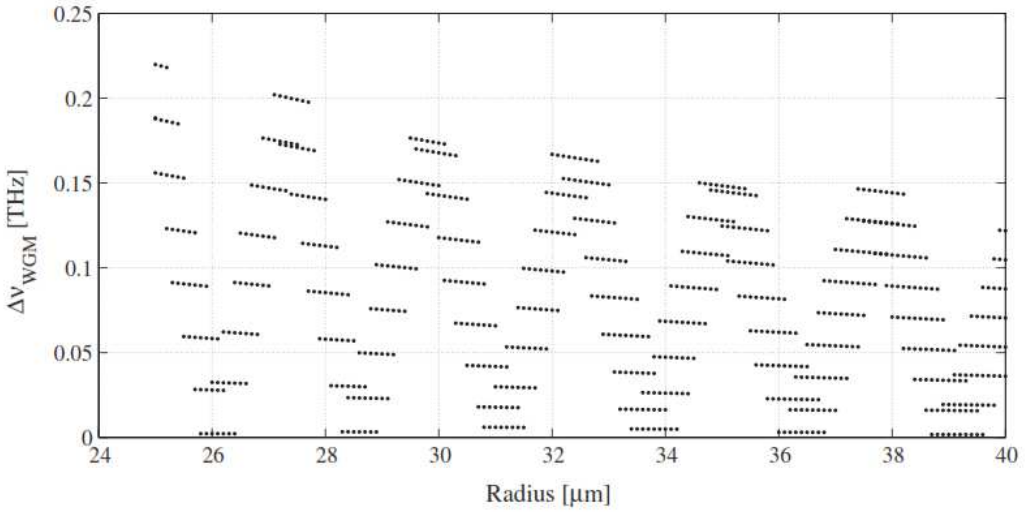

Figure 4.2: Difference between the resonance position at the pump frequency (in the range of the erbium gain bandwidth) and the closest resonance around the corresponding TH frequency (divided by 3). The dispersion is calculated for the fundamental WGMs only and shows a set of ranges for which we have an optimal match ($\Delta\nu_{WGM} = 0$).

a set of ray ranges for which we have an optimal match ($\Delta\nu$=0). Figure 4.2 shows an oscillatory behavior of $\Delta\nu$ vs microsphere size, and therefore there are only certain ideal sphere diameters for which $\Delta\nu$ is less than the sum of their individual linewidths [140]. We focused our experiment on the range between 28 and 29 μm.

The inset graph in Fig. 4.3(a) shows a typical emission spectrum with the THG signal occurring at 519.6 nm for a resonant pump wavelength of 1556.95 nm in a microsphere of 57$\pm$1 μm in diameter. We collected the THG signal scattered by the WGMR with a MMF (without coupling optics) for the pump power dependence measurements.

The scattered visible light shows a cubic dependence on the launched pump power, as shown in Fig. 4.3(a) (TH power versus 5% of the launched power measured after the splitter (see Fig. 4.1)). Tuning the THG signal is

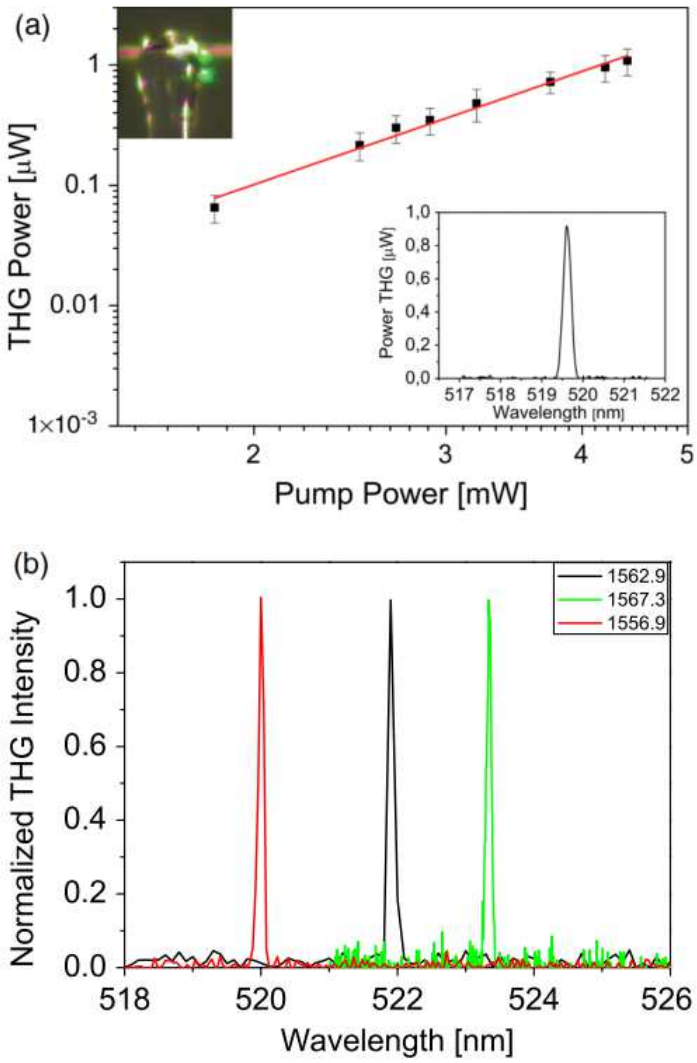

Figure 4.3: (a) Measured power of the generated TH signal versus the 5% of the pump power, under 1556.9 nm pumping (log-log scale), revealing a cubic dependency as expected for THG. The red line corresponds to the linear fit (slope 3.1 ±0.12, R=0.99). The inset graph shows the emission spectrum indicating THG at 519.6 nm when pumping at 1556.9 nm, whereas the inset picture was taken during the spectral measurements. (b) Measured TH signal for different pump wavelengths in the erbium band gain of the EDFA.).

possible by varying the pump wavelength in the range of the erbium band gain of the EDFA. In Fig. 4.3(b) we show three different TH wavelengths obtained in different microspheres by changing the pump wavelengths. The measured THG wavelengths showed a deviation comparable with the resolution of the optical spectrometer. In these cases, THG was observed without SRS (or FWM), demonstrating that under phase-matching conditions THG is enhanced in comparison with other nonlinear phenomena. In fact, TH power scales with $(Q_p)^3 Q_{TH}/V^2$, whereas other nonlinear competing phenomena scale with lower powers of Q/V [152] and SRS scales with $Q_p Q_{SRS}/V$. Our experiments were performed with a maximum launched pump power (P_p) of about 80 mW, and the corresponding maximum THG signal (P_{TH}) was about 1 μW for scattered [see the inset graph of Fig. 3(a)] and about 0.1 μW for fiber guided THG signal (the taper is not phase matched in the visible). Thus, our maximum conversion efficiency $\eta(P_{TH}/P_p)$ is in excess of 10^{-5}(10^{-6} for fiber guided TH signal). This value represents an increase of 6 orders of magnitude over that reported in a ring resonator [153]. The inset picture of Fig. 4.3(a) shows a THG signal codirectional with the pump (light in the taper is coming from the left), as expected [138]. For high pump powers, other nonlinear processes are observed in the IR region, such as stimulated Raman scattering (SRS) and cascaded SRS. Lasing through SRS and cascaded SRS exhibit a clear threshold [145, 212, 154] and a linear behavior with the pump power. In the presence of these phenomena, we have also observed TSFG in the visible, obtaining multicolor emission by tuning the pump wavelength: red, orange, yellow, and green. Figure 4.4 shows the measured spectra for each different color and the corresponding microscope picture of the microsphere. In the inset pictures of Fig.4.4, the TSFG signals are standing waves, since the sum involves only SRS fields. In these cases, the pump was high enough to generate several orders of Stokes Raman lines and Raman combs. TSFG and THG can also happen simultaneously. Figure

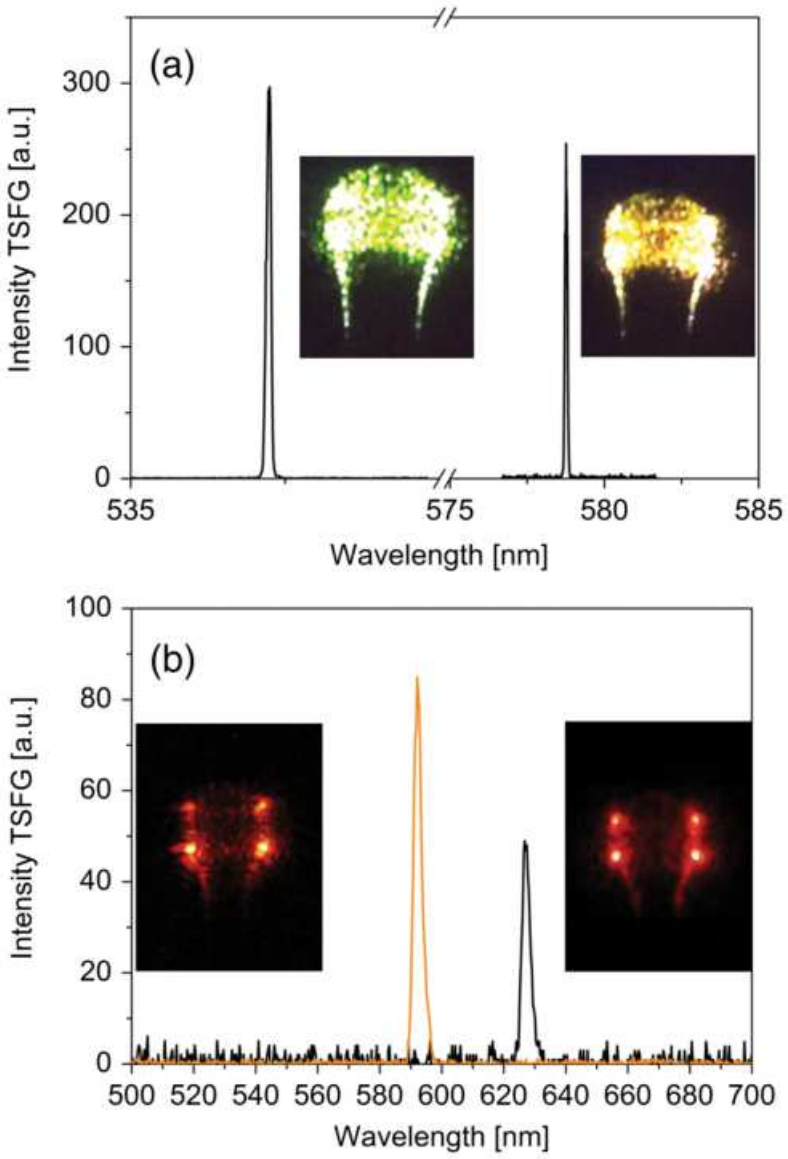

Figure 4.4: Emission spectra indicating third order sum frequency generation among the pump wavelength and the cascaded Raman lines. (a) Left: at 1568.4 nm pump wavelength, emission at 537.24 nm; right: at 1567 nm pump wavelength, with emission at 578.76 nm; (b) Left: at 1553 nm pump wavelength, emitting at 592 nm; right: at 1568.4 nm pump wavelength, with emission at 625 nm. The spectra shown in (a) have been taken with an OSA, and in (b) with a handheld spectrometer. The inset pictures show standing waves.

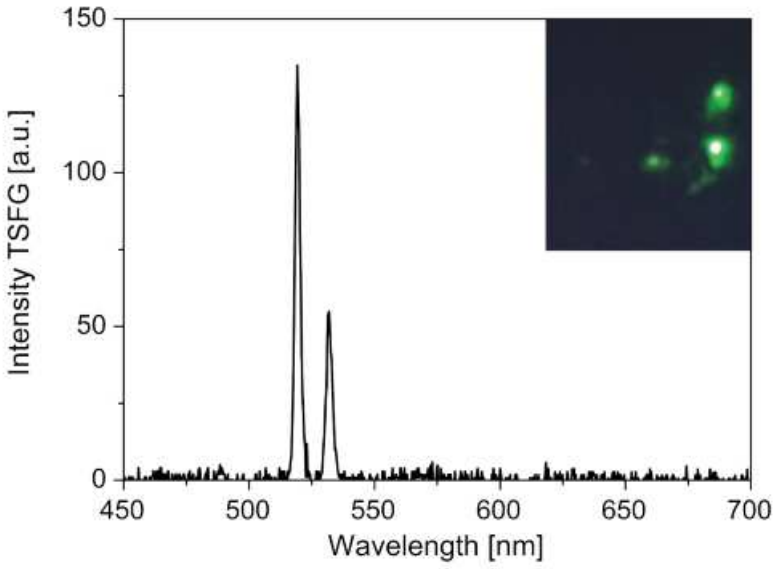

Figure 4.5: Emission spectra indicating third harmonic and third order sum frequency generation among the pump wavelength at 1554.4 nm at 1665.4 nm, with THG emission at 519.24 nm and TSFG at 531.5 nm. The inset picture shows a traveling wave.

4.5 shows the spectrum with two lines, one at 519.2 and one at 531.5 nm, the THG signal of the pump laser and the TSFG signal of the pump laser and a Raman line ($\omega_{TSFG} = 2\omega_p + \omega_{SRS}$).

In this case, the TSFG is a traveling wave, since the nonlinear polarization involves the pump laser (inset of Fig. 4.5). The lines are separated by 13 THz. As can be clearly seen from all the above inset pictures, we have experimentally observed that higher order polar modes ($l- \mid m \mid > 1$) have to be excited, with the coupling taper placed far from the equatorial plane (see inset of Fig. 4.3) in a region corresponding to the intensity peaks of these modes [149]. These modes not only allow the phase matching conditions to be fulfilled and compensate dispersion, as previously stated, but they also provide improved mode matching which is also required for efficient TSFG/THG. We recall that TSFG power is proportional to the overlap of

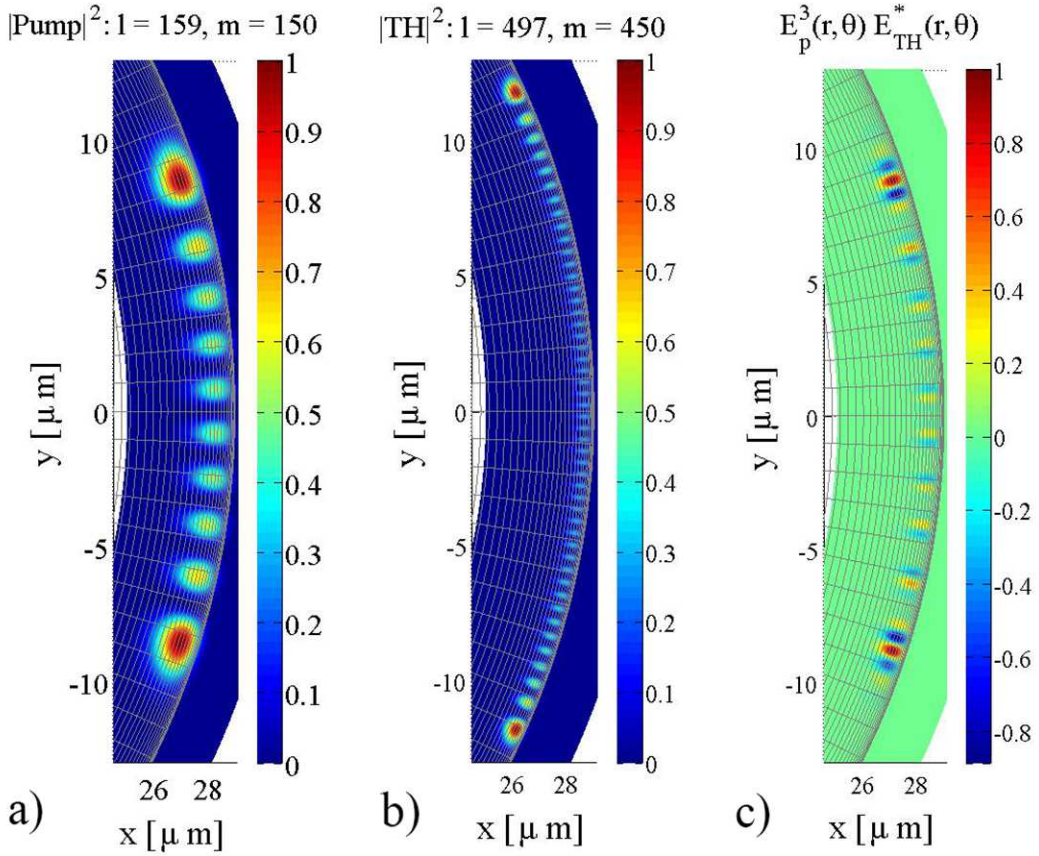

Figure 4.6: (a) Intensity distribution of the pump mode, (b) intensity distribution for the THG mode, and (c) overlap of the nonlinear polarization and the electric field distribution of the THG mode. The color bar indicates the relative intensities in arbitrary units.

the WGM eigenfunctions [see Eq. (4.18)] and, for the degenerate case of THG, the total power is proportional to the overlap of the cubic power of the pump field with the corresponding TH field. Figure 4.6 distribution in a microsphere with a radius of 29 μm for the pump mode [Fig. 4.6(a)] and the THG mode [Fig.4.6(b)]; and the overlap [Fig. 4.6(c)] between the nonlinear polarization and electric field distribution of the THG for a specific example of a well matched mode.

A good overlap in the regions corresponding to the fields "inversion point" is observed. The simulations of the optical modes have been done following

the Mie theory with a homemade program. The pump mode is the first order mode at 1567 nm ($n_p = 1, l_p = 159, m_p = 150$) and the THG mode is the first order mode at 522 nm ($n_{THG} = 1, l_{THG} = 497, m_{THG} = 450$). This case satisfies the quantum SRS rules for angular momentum composition [143] and represents a perfect phase match, since the coherence length of a WGM resonance for THG is infinite for $m_{THG} = 3m_p (l_{coh} = \pi R/ \mid m_{THG} - 3m_p \mid)$, and it has the largest angular overlap ($l_{THG} \sim 3l_p$) [140].

4.2.4 Conclusion

We observed fiber coupled THG and TSFG in silica microspherical WGMR for several pump wavelengths within the erbium band gain of the EDFA. Cavity mode dispersion was controlled by choosing suitable sizes of the silica microspheres. Phase matching was improved by exciting high order modes coincident with a particular THG and/or TSFG frequency. In this case, there is a good spatial overlap of the resonances at the pump frequency and THG frequency. The THG and pump photons are in the states $|n_{THG} l_{THG} m_{THG}\rangle$ and satisfied $|n_p l_p m_p\rangle$, respectively, and satisfied $l_{THG} \sim 3l_p$ and $m_{THG} = 3m_p$. With this work, we have illustrated the great potential of WGMR as frequency converters for cw compact, room temperature, narrow linewidth, and tunable sources for lab-on-a-chip biosensors, spectroscopic applications, and the possibility of generation of nonclassical light.

Chapter 5

Long Period Gratings for new coupling techniques

5.1 General Properties

The concept of long period fiber grating (LPG) as a periodic refractive index (RI) perturbation along the axis of an optical fiber, appeared in 1996 [155]. LPGs can be written in all kind of fibers and the techniques available for the production can be divided in two groups: the ones for permanent gratings and the ones for reversible gratings [156].

The most common methods to fabricate gratings is to illuminate the side of a photosensitive and/or hydrogenated fiber with a UV laser, like a KrF excimer laser [157, 158] or the second harmonic of a CW Ar ion laser (244 nm)[159]. However, there are several alternative technique that does not require the fiber to be photosensitive. For instance, by heating a fiber heavily twisted [160], by periodic etched corrugating cladding [161] or through an amplitude mask for a He ions beam [162].

In any case, the modulation profile of the radial index can be written as:

$$n(z) = n_1 \left\{ 1 + \omega(z) \left[1 + cos\left(\frac{2\pi}{\Lambda} z \right) \right] \right\} \tag{5.1}$$

where n_1 is the fiber core unperturbated refractive index, Λ is the grating period and $\omega(z)$ is the envelope of the refractive index modualtion. If an induced index changes $\delta n_{co}(z)$ is created across the core of a step-index fiber, $n(z) \approx \Gamma \delta n_{co}(z)$ where Γ is the core power confinement factor and n_{co} is the refractive index of the core. The effective index can be found through an effective index parameter b, solution of the dispersion relation [163]:

$$V\sqrt{1-b}\frac{J_{l-1}(V\sqrt{1-b})}{J_l(V\sqrt{1-b})} = -V\sqrt{b}\frac{K_{l-1}(V\sqrt{b})}{K_l(V\sqrt{b})} \tag{5.2}$$

where l is the azimuthal order and $V = 2\pi/\lambda a\sqrt{n_{co}^2 - n_{cl}^2}$ is a normalized frequency, a the core radius and n_{cl} is the refractive index of the cladding. The effective index and b are related by $b = (n_{eff}^2 - n_{cl}^2)/(n_{co}^2 - n_{cl}^2)$ and Γ can be determinated by

$$\Gamma = \frac{b^2}{V^2}\left[1 - \frac{J_l^2(V\sqrt{1-b})}{J_{l+1}(V\sqrt{1-b})J_{l-1}(\sqrt{1-b})} \right] \tag{5.3}$$

A qualitative picture of the interaction in the system can be obtained, in the ray optics, starting by the diffraction equation for the incident and the diffracted light:

$$n_2 sin\theta_2 = n_1 sin\theta_1 + q\frac{\lambda}{\Lambda} \tag{5.4}$$

where n_1 is the RI of the core, n_2 is the cladding RI, q is the order of diffraction, λ is the wavelength of the light, Λ is the period of the diffraction grating, θ_1 is the incident angle and θ_2 the diffraction angle (Fig.5.1).

For a transmission grating, the prominent diffraction order is $q = -1$. By defining the effective refractive index $n_{eff,co} = n_{co} sin\theta$ and $n_{eff,cl} = n_{cl} sin\theta_2$, the Eq.(5.1) can be rewritten as

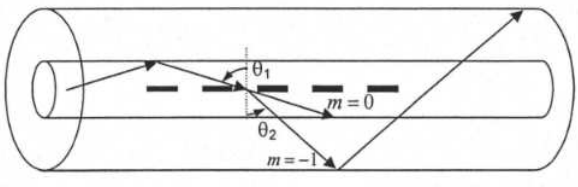

Figure 5.1: Illustration of core-cladding mode coupling in a LPG.

$$\lambda = (n_{eff,co} - n_{eff,cl})\Lambda \tag{5.5}$$

The core-cladding mode coupling can be described using a couple mode theory, assuming uniform RI modulation across the LPG. Due to the mode orthogonality, mode coupling occurs only between the same azimuthal mode orders. The ampitude change of the core mode (HE_{11}) and the co-propagating cladding modes ($HE_{1\nu}$) can be written as:

$$\frac{dA^{co}}{dz} = jk_{11-11}^{co-co}A^{co} + j\sum_{\nu}\frac{m}{2}k_{1\nu-11}^{cl-co}A_{\nu}^{cl}exp(-j2\delta_{1\nu-11}^{cl-co}z) \tag{5.6}$$

$$\sum_{\nu}\left[\frac{dA_{\nu}^{cl}}{dz} = j\frac{m}{2}k_{1\nu-11}^{cl-co}A^{co}exp(j2\delta_{1\nu-11}^{cl-co}z)\right] \tag{5.7}$$

where A^{co} is the amplitude of the HE_{11} core mode, A_{ν}^{cl} is the amplitude of the ν-th order cladding mode. The core-core self coupling coefficinet and the $HE_{11} - HE_{1\nu}$ coupling coefficient are respectively

$$\kappa_{11-11}^{co-co}(z) = \frac{\omega\epsilon_0 n_1^2\sigma(z)}{2}\int_0^{2\pi}d\phi\int_0^{r_1}rdr\left(|E_r^{co}|^2 + |E_\theta|^2\right) \tag{5.8}$$

$$\kappa_{1\nu-11}^{cl-co}(z) = \frac{\omega\epsilon_0 n_1^2\sigma(z)}{2}\int_0^{2\pi}d\phi\int_0^{r_1}rdr\left(E_r^{\nu,cl}E_r^{co*} + E_\theta^{\nu,cl}E_\theta^{co*}\right) \tag{5.9}$$

The detuning parameter is

$$\delta_{11-1\nu}^{cl-co} = \frac{1}{2}\left(\beta_{11}^{co} - \beta_{1\nu}^{cl} - \frac{2\pi}{\Lambda}\right) \tag{5.10}$$

where $\beta_{11}^{co} = n_{eff,11}^{co} k_0$ is the propagation constant of the core mode and $\beta_{1\nu}^{cl} = n_{eff,1\nu}^{cl} k_0$ is the propagation constant for the cladding mode.

By assuming that only one of the cladding modes is near to the resonance of the core mode and neglecting all other resonances. The analytical solution for an uniform grating $\sigma(z) = \sigma n_1$ can be written as

$$A_{11}^{co}(L/2) = \left[cos(\gamma_c L) + j\frac{\hat{\sigma}}{\gamma_c} sin(\gamma_c L) \right] A_{11}^{co}(-L/2) + j\frac{\kappa_{1\nu}^{cl-co}}{\gamma_c sin(\gamma_c L) A_{1\nu}^{cl}(-L/2)} \tag{5.11}$$

$$A_{1\nu}^{cl}(L/2) = j\frac{\kappa}{\gamma_c} sin(\gamma_c L) A_{11}^{co}(-L/2) + \left[cos(\gamma_c L) - j\frac{\hat{\sigma}}{\gamma_c} sin(\gamma_c L) \right] A_{1\nu}^{cl}(-L/2) \tag{5.12}$$

where

$$\gamma_c = \sqrt{\kappa_{1\nu-11}^{cl-co} + \sigma^2} \tag{5.13}$$

$$\hat{\sigma} = \delta_{11-1\nu}^{cl-co} + \frac{\kappa_{11-11}^{co-co} - \kappa_{1\nu-1\nu}^{cl-cl}}{2} \tag{5.14}$$

$$\kappa_{1\nu-1\nu}^{cl-cl}(z) = \frac{\omega \epsilon_0 n_1^2 \sigma(z)}{2} \int_0^{2\pi} d\phi \int_0^{r_1} r dr \left(\left| E_r^{cl} \right|^2 + \left| E_\phi^{cl} \right|^2 \right) \tag{5.15}$$

By imposing the boundary condiction for a LPG ($A_{11}^{co}(-L/2) = 1$ and $A_{1\nu}^{cl}(-L/2) = 0$), the transmission spectrum can be calculated

$$T = \frac{|A_{11}^{co}(L/2)|^2}{|A_{11}^{co}(-L/2)|^2} = \frac{\delta_{11-1\nu}^{cl-co2}}{\gamma_c^2} sin^2(\gamma_c L) + cos^2(\gamma_c L) \tag{5.16}$$

The maximum loss in the transmission spectrum, at the resonant wavelength (where the detuning parameter $\delta_{11-1\nu}^{cl-co} = 1/2(\beta_{11}^{co} - \beta_{1\nu}^{cl} - 2\pi/\Lambda) = 0$) is

$$T_{min}^{11-1m} = 1 - sin^2 \kappa_{11-1m} L \tag{5.17}$$

Other two important paramenters are the spectral bandwidth of the co-propagating resonance [164]:

$$\frac{\Delta\lambda}{\lambda} \approx \frac{\lambda}{\Delta nL}\left(1+\frac{4\kappa_{1\nu-01}^{cl-co}L}{\pi}\right)^{1/2} \tag{5.18}$$

where $\Delta n = n_{eff}^{co} - n_{eff}^{cl}$, and the the ratio of power coupled into a particular nth cladding mode to the initial power guided into the core, which is given by [155]:

$$\frac{P_{cl}^{n}(L)}{P_{01}(0)} = \frac{sin^2\left[\kappa L\sqrt{1+\left(\frac{\delta}{\kappa}\right)^2}\right]}{1+\left(\frac{\delta}{\kappa}\right)^2} \tag{5.19}$$

where δ is the detuning parameter and κ is the coupling constant $\kappa_{1\nu-01}^{cl-co}$.

5.2 Applications

LPGs have several applications in the comunication and sensing fields. In the first case, the three most important are probably the band rejection filters [165], the optical switches [166] and the add-drop multiplexers [167]. From sensoristic point of view the LPG are very sensitive to the changes of physical parameters as temperature [168], bending [169], strain [170], torsion [171] and the refractive index of the surrounding medium [172].

The sensitivity to changing surrouding RI derives from the dependence, of the phase matching condition, on the effective refractive index of the cladding mode. n_{eff}^{cl} is determinated by the difference between the RI of the cladding and the one of surronding medium. The greatest sensitivity occurs when $n_{environment} \approx n_{cladding}$. Generally the sensitivity increases with the order of the cladding modes (short periods) [173]. LPGs can be used as detector for chemical measures of concentration in liquids of sugar [175] or salt [176], as biosensor [177] and flow sensor [178].

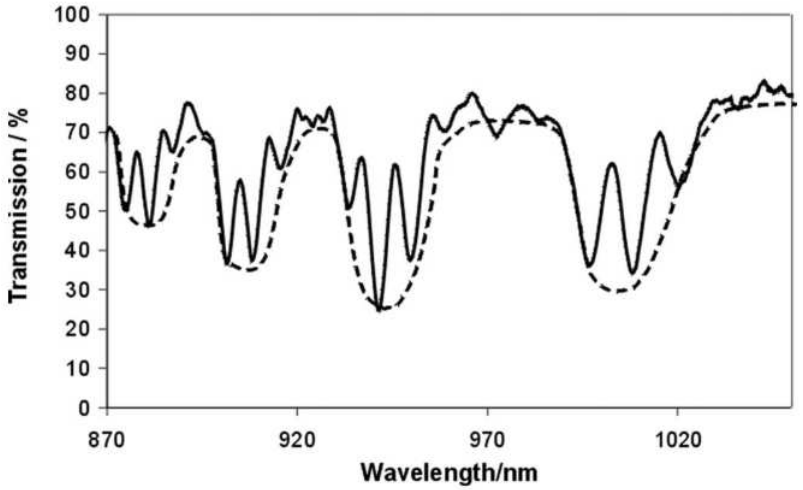

Figure 5.2: Attenuation bands with interference fringes in the transmission spectrum of a cascaded LPG [174].

Due to the variety of application, several variations of LPG have been employed: LPGs at the phase matching turning point [179], chirped [180], tilted [181], cascaded [141] and phase shifted LPGs [182].

Our attention has been focusing in particular on the cascaded LPGs which consist of two identical LPGS written in series along the same section of the fiber. The first LPG couples some of the light from the core to the cladding. The light propagates in the free region towards the second grating via the core and the cladding. Then the cladding mode is coupled back into the core by the second LPG to form a kind of Mach-Zender interferometer[174]. The light coupled from the cladding into the core at the second LPG, due to the difference between the effective refractive indices of the cladding and core modes, experiences a different optical path length compare with the light that propagate though the core. The interference generates a channeled spectrum, as show in the solid line of figure 5.2.

The period of the channelled spectrum pattern within the attenuation bands of the LPG is determinated by the distance between the gratings [183]. The smaller the separation the longer the period. Even the lenght of each

grating affect the trasmission of the cascated LPG [141]. If d is the grating length and $\Delta\beta$ is the detuning parameter, the amplitude of the core mode coupled by the first grating can be calculated from:

$$\frac{A(d)}{A(0)} = exp\left[i(\Delta\beta/2)d\right]\left(cos(sd) - i\frac{\Delta\beta}{2s}sin(sd)\right) \tag{5.20}$$

where s is defined by $s^2 = \kappa\kappa* + (\Delta\beta/2)^2$ with κ the coupling coefficient of the grating. The amplitude of the core mode after the second LPG can be written as

$$\begin{aligned}\frac{A(L+2d)}{A(0)} &= \left(cos(sd) - i\frac{\Delta\beta}{2s}sin(sd)\right)^2 \\ &\times exp\left[i\Delta\beta d - i(\beta_{core} - \beta_{clad})(L+d)\right] - \alpha\frac{\kappa\kappa*}{s^2}sin^2(sd)\end{aligned} \tag{5.21}$$

where L is the distance between the gratings, α is the loss on the cladding mode. The above equation can be rewritten in polar form:

$$\frac{A(L+2d)}{A(0)} = \left[cos^2(sd) + \left(\frac{\Delta\beta}{2s}\right)^2 sin^2(sd)\right] exp(i\psi) - \alpha\frac{\kappa\kappa*}{s^2}sin^2(sd) \tag{5.22}$$

where the total phase shift is

$$\psi = \Phi_{in} - (\beta_{core} - \beta_{clad})(L+d) \tag{5.23}$$

and

$$\Phi_{in} = 2\ tan^{-1}\left(-\frac{\Delta\beta}{2s}tan(sd)\right) + \Delta\beta d \tag{5.24}$$

is the phase shift within the gratings. The peak of the resulting sinusoidal interference fringes is obtained when the relative phase is an integer multiple of 2π. We can get the fringe spacing S by differentiating Eq.(5.23) with respect to λ

$$S = \frac{\lambda^2}{\Delta m_{in} d + \Delta m_{out}(L-d)} \tag{5.25}$$

where *in* and *out* mean the value within and out the grating region. The effective group index is defined as

$$\Delta m = \Delta n_{eff} - \lambda \frac{d\Delta n_{eff}}{d\lambda} \tag{5.26}$$

in which $\Delta n_{eff} = n_{eff}^{co} - n_{eff}^{cl}$.

It results to be inversely proportonal to the distante between the center of the gratings and to the difference between the effective group index of the two modes. Finally the band envelope of the interference fringes are obtained when the phase factor $exp(i\psi) = \pm 1$:

$$T_{min} = [T_{sing} - \alpha(1 - T_{sing})]^2 \tag{5.27}$$

$$T_{max} = [T_{sing} + \alpha(1 - T_{sing})]^2 \tag{5.28}$$

where $T_{sing} = cos^2(sd) + (\Delta\beta/2s)^2 sin^2(sd)$ is the transmissivity of a single LPG calculated as the absolute square of Eq.(5.20).

The cascaded LPG configuration has been used, first of all, for sensing purposes [184]. A high sensitivity and resolution can be reached when the fringe pattern is fine enough (narrow bandwidth). If the region between the two gratings is covered with a material that changes the RI, the channelled spectrum changes whilst the band envelope remains unchanged [185].

5.3 Article 4: Long period grating-based fiber coupler to whispering gallery mode resonators

5.3.1 Abstract

We present a new method for coupling light to high-Q silica whispering gallery mode resonators (WGMs) that is based on long period fiber gratings (LPGs) written in silica fibers. An LPG allows selective excitation of high-order azimuthally symmetric cladding modes in a fiber. Coupling of these cladding modes to WGMs in silica resonators is possible when partial tapering of the fiber is also implemented in order to reduce the optical field size and increase its external evanescent portion. Importantly, the taper size is about one order of magnitude larger than that of a standard fiber taper coupler. The suggested approach is therefore much more robust and useful especially for practical applications. We demonstrate coupling to high-Q silica microspheres and microbubbles detecting the transmission dip at the fiber output when crossing a resonance.

5.3.2 Introduction

High-Q whispering gallery mode (WGM) microresonators, with their long cavity lifetime and small mode volumes, strongly enhance light-matter interactions and are extensively exploited both for fundamental studies and for practical applications [149, 186]. A critical point is the implementation of an efficient and controllable coupling of the light to the cavity modes. The best approach relies on phase-matched evanescent-field coupling and requires some overlap between the evanescent field of the WGM and that of the coupler [52]. The devices most commonly used to inject light into

a WGM microresonator are either prisms [49], or waveguides, such as integrated waveguides [188, 189], and tapered optical fibers [190]. Fiber tapers are used for lab demonstrations in nonlinear optics, both with silica based micro-resonators [191] and with low-index crystalline disks [192]. Indeed, silica fiber biconical tapers are excellent and easy-to-align coupling tools that offer great flexibility for an ideal phase- and mode-matching to the resonator modes. Additionally, add–drop configurations with an input and an output taper can be efficiently implemented for different applications like filtering [193] or sensing [194]. The appropriate taper waist can be as small as 1 μm in diameter, with the fundamental mode extending significantly into the free space surrounding the taper. However, a critical point for these fiber couplers is the fact that the tapered region is very thin and therefore very fragile and easy to deteriorate. We demonstrate a new method for coupling light from high-order fiber-cladding modes to high-Q silica WGMs in silica resonators. The approach is based on a long period fiber grating (LPG) followed by an adiabatically tapered section of the fiber, which is about one order of magnitude thicker than that of standard fiber tapers, and therefore much more robust. An LPG is characterized by a series of periodic refractive index changes in the core of a single-mode optical fiber. A standard LPG has typically a grating period Λ in the range from 100 to 500 μm, and the coupling happens between the fundamental core mode and copropagating azimuthally symmetric LP0i ($i \geq 2$) cladding modes. One or more attenuation bands characterize the transmission spectrum with the minimum of each band representing the coupling with a selected cladding mode [155].

5.3.3 Experimental setup and results

We manufacture the LPGs in boron-germanium codoped optical fibers (Fibercore PS1250/1500) with a point-to-point technique, by using a KrF excimer

laser (Lambda Physic COMPex 110 at λ=248 nm). The fiber is mounted on a motorized translation stage and is then irradiated by the laser spot, which is appropriately shaped and focused with a cylindrical lens and with an adjustable micrometric slit. The stage and laser operations are controlled by a PC, allowing easy customization of the LPG's characteristics [195]. Direct UV writing process allows fabricating pure volume gratings, and therefore, our LPGs are polarization insensitive. It is well known that coupling strength between the fiber (or more generally, a waveguide) mode and the WGM depends on how good the modes are overlapped and their phases are matched [52]. Phase matching is possible within a wide range in WGM resonators because of the dense distribution of effective refractive indices, whose values decrease when increasing the order of the corresponding radial and azimuthal modes [187]. On the other side, to improve the modes overlap, partial tapering of the fiber is necessary in order to increase the evanescent portion of the field outside the taper and to reduce its overall size. LPG-based evanescent-field coupling has been suggested [196] and demonstrated [197] in bare fibers mainly for broadband filtering purposes. However, a similar approach without tapering the fiber after the LPG would not work in our case. Taper has to be adiabatic so that the same excited mode propagates in the tapered section. Additionally, its minimum size has to be above cut-off for that mode so that it does not radiate outside the taper and it is transmitted after the taper. In this way it is possible to observe the resonance dip corresponding to the coupling with a WGM when monitoring the light transmitted at the fiber output (while scanning the wavelength). With the data provided by the manufacturer for the fiber and by using commercial software [198], we calculated the minimum taper diameters, which depend on the excited mode and the surrounding medium, and the corresponding LP0i effective refractive indices. For the wavelength band we targeted (third telecom window, up to 1640 nm), and the LPG period (above 370 μm), we found ideal diameters

in excess of 15 μm (in air). These tapers are one order of magnitude thicker than the "standard" fiber tapers used for coupling light to WGM resonators [149], and therefore, they are much more robust. Fiber taper are fabricated by heating and at the same time slowly stretching a section of an optical fiber. The stripped fiber is placed inside a short alumina cylinder, which is then heated by an oxygen-butane flame up to a temperature close to the melting point of silica (about 2100°C) [149]. An LPG with a period of 425 μm and 1 cm long was fabricated on one side of the taper, which was pulled first. The period was chosen in order to have the maximum dip around 1625 nm. We characterized the transmission of the fiber core after the LPG and the taper section first, and then in the opposite direction, from the taper to the LPG. For this purpose, we used two fiber pigtailed tunable external cavity lasers (Anritsu Tunics Plus) covering the band wavelength from 1390 nm to 1640 nm. Results are shown in Fig.5.3. We found that the LPG transmission band was the same independently on the direction of the incident light (LPG or taper first). Each attenuation band represents the coupling with a selected cladding mode. The deepest one around 1625 nm corresponds to the excitation of the LP06 mode, as shown in the near field image in Fig.5.3, which is collected with a vidicon tube camera.

The 10-dB attenuation band means that 90% of the power is coupled from the fundamental fiber mode to the LP06 cladding mode. The tapered section we fabricated had a minimum waist of 18 μm. The effective index of the LP06 mode at the minimum waist is 1.3497 at 1625 nm with about 1% of the power outside the fiber. Effective mode area, which is roughly inversely related to the overlap integral with the WGM (and therefore inversely related to coupling strength), is about 30 times larger than that of the fundamental LP_{01} mode of a 2μm taper but still more than 40 times smaller than that of a LP06 cladding mode in a standard bare fiber. Microsphere size should be large enough so that, within a cavity-free spectral range (FSR), the LPG

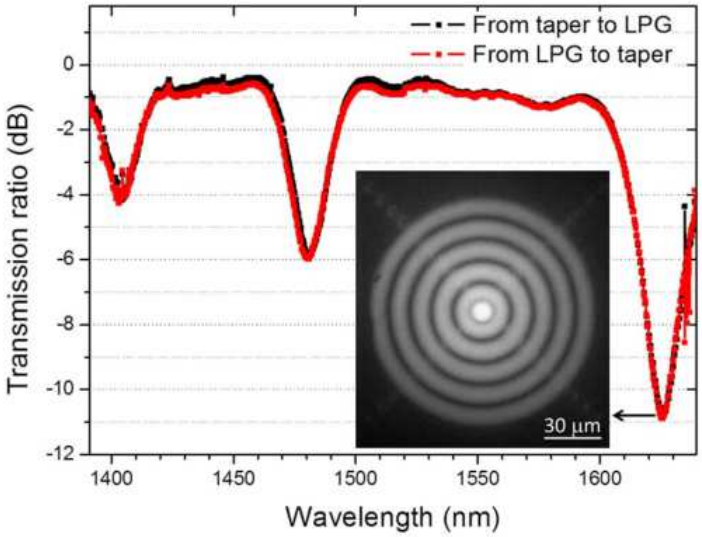

Figure 5.3: Transmission spectra of the fiber core through an LPG with a period of 425 μm and a taper of 18 μm. The spectra are measured in both directions. The picture shows the near field intensity image of the LP06 mode associated with the attenuation band around 1625 nm.

transmission dip is almost flat, and therefore, transmission is not distorted by the LPG. The bandwidth of the coupler is then set by the resonators FSR. A larger bandwidth would not be necessary as we would simply get replicas of the same resonator spectrum. We selected microspheres larger than 240 μm, corresponding to 2.4 nm FSR. Indeed within such band, we observe only a 0.35dB (8%) change in the LPG transmission dip at 1625 nm. The microspheres can be easily fabricated by melting the tip of a standard silica fiber by using a fiber fusion splicer (FITEL S182 K). A cleaved tip of the fiber is inserted in one arm of the splicer, and a series of arcs are then produced. The tip partially melts, and surface tension forces produce the spherical shape [110]. The setup for testing the new coupling approach is shown in Fig.5.4.

The LPG exciting cladding modes is followed by the "thick" taper where coupling with the resonator takes place. The picture in the inset shows a

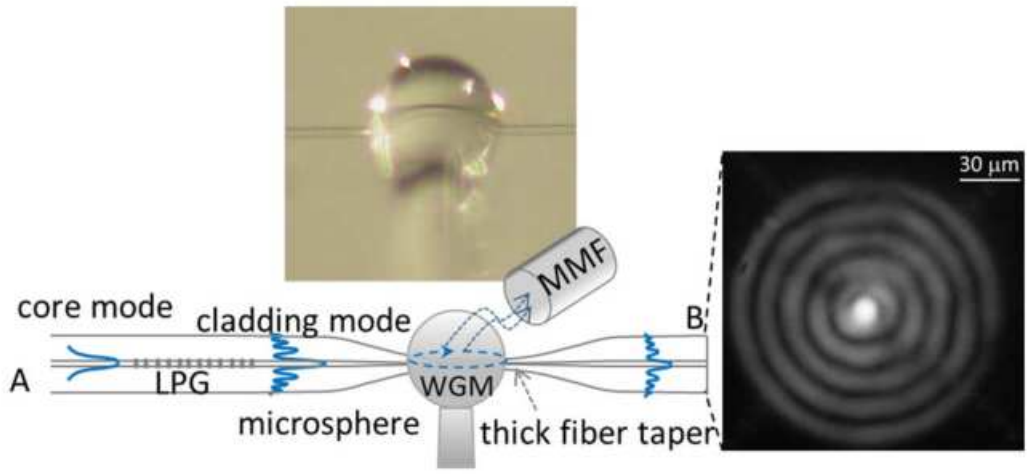

Figure 5.4: Sketch of the experimental setup showing the LPG exciting the cladding mode followed by a "thick" taper where coupling with the resonator takes place. The image in the inset shows a 290μm silica sphere with the fiber taper visible in the background. Light scattered from the microsphere is collected using a multimode fiber (MMF). The picture on the right shows the near field intensity image of the output at 1625 nm.

silica microsphere in contact with the fiber taper visible in the background. We point out that all our measurements where performed with the taper in contact with the micro-resonators, which makes our approach very stable. Light transmitted through the fiber is then collected at the output through a microscope objective and focused on a photo-detector connected to an oscilloscope (or focused on a vidicon tube camera for IR imaging). The light scattered from the microsphere can be collected using a multimode fiber (MMF) and sent to a second detector. In order to maximize the signal, the MMF is placed with its axis tangent to the microsphere, so that the input facet mainly collects forward scattering. The fiber has its cladding removed and is cleaved after the tapered section (side B in Fig.5.4) in order to monitor the transmission of the cladding modes or collect the near field. The fiber output is placed on a low-index Teflon holder. The field intensity image of the output around 1625 nm is shown on the right side of Fig.5.4. The LP06 mode structure appears rather well preserved after the tapered section, which is intended to be adiabatic, and the mode should carry a significant portion of the power, even though the taper supports hundreds of modes (V number $\sim$36 at the minimum waist). As expected, when collecting the total power at the fiber output, we observe minimum modulation or absorption in the transmission band, which appears almost flat in the wavelength range of Fig.5.3. The pigtailed external cavity laser sources having a linewidth of 300 kHz can be finely and continuously swept in wavelength by a few GHz. By scanning around 1625 nm, we successfully observed resonances in the transmission spectra of microspheres of different sizes (we tested a range from 260 to 290 μm in diameter). Figure 5.5 shows a typical WGM resonance excited by our coupling system in a 290μm silica microsphere with a Q factor in excess of 10^7 and a contrast K (fractional depth of the resonance dip in intensity transmittance) of about 22%.

The term coupling efficiency is often used as equivalent of the contrast K.

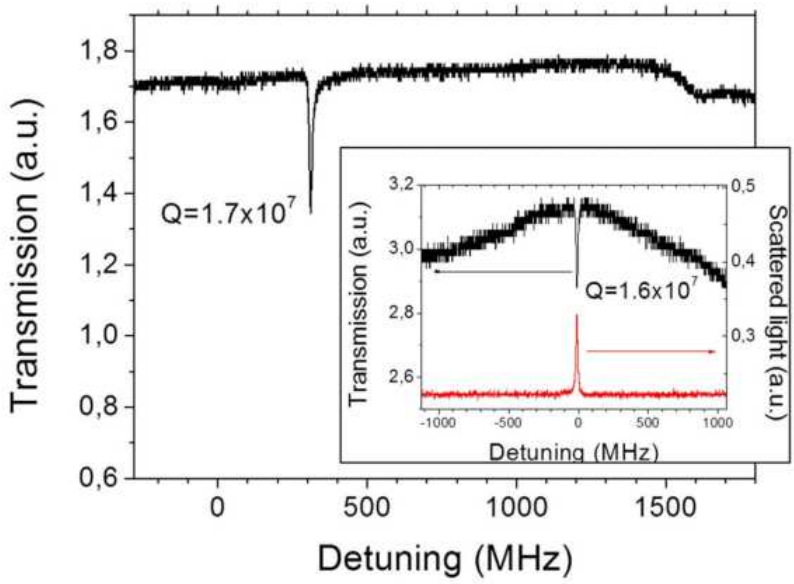

Figure 5.5: Example of WGM resonances excited in a 290μm silica microsphere around 1625 nm by using the proposed coupling system. Maximum resonance contrast is about 22%. The inset shows a resonance monitored both in transmission and by collecting the scattered light through a MMF.

So 22% represents the total efficiency of the coupling from the fundamental fiber mode to a microresonator WGW. The inset shows another resonance, which is monitored both in transmission and by collecting the scattered light through the MM fiber. As already mentioned, because of the large mode area of the cladding mode, as compared with the fundamental mode of micrometer size tapers, the coupling strength is strongly reduced. In consequence, the density of the excited resonances is effectively diminished in the transmission spectrum. The phase-matching condition to the cladding mode, as previously stated, can be fulfilled thanks to the higher order radial and azimuthal modes of spherical WGM resonators [187]. The maximum resonance contrast is partially limited by the fact that we are far from the condition of "single-mode" waveguide coupler, but we have instead a multimode coupler [130]. In fact, as already stated, in the tapered section, partial scrambling of modes occurs and some power is contained in other modes (rather than the selected cladding mode) including the fundamental core mode. At the resonant wavelength this portion of the power is just transmitted through the taper. Anyway, the measured resonance contrast is high enough for practical applications in sensing, which are mainly based on monitoring the resonance shift [199]. Finally, no significant coupling was observed when placing the microsphere outside the tapered portion of the fiber or when scanning outside the attenuation band of the LPG. It is important to point out a unique feature of this novel coupling approach to micro-optical WGM resonators. In fact by fabricating a series of LPGs with different periods (along the same fiber), each having a different attenuation band and followed by a taper, it would be possible to independently address (by selecting the proper wavelength) different microspheres coupled along the fiber. This "multiplexing" feature would be particularly significant for some applications like distributed biosensing and would not be possible with the "standard" fiber taper coupling method. We have also demonstrated coupling to microbubble resonators that

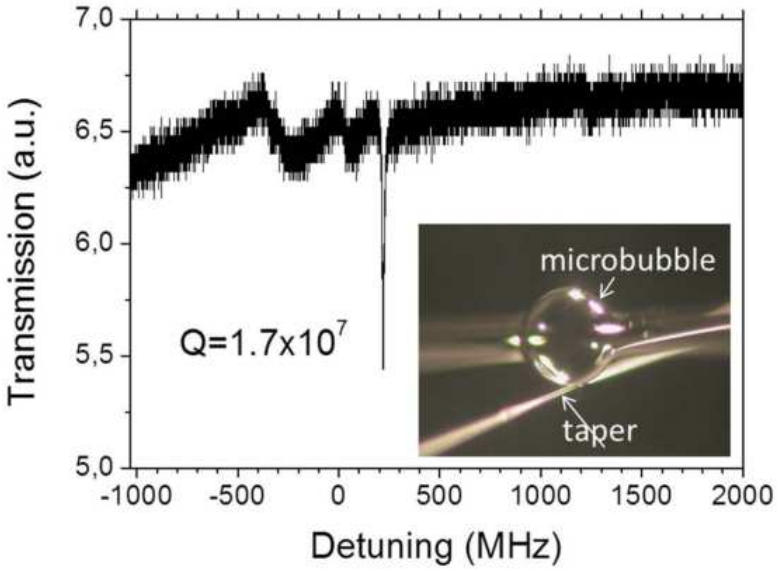

Figure 5.6: Example of a WGM resonance excited in a silica micro-bubble with external diameter of a 490 μm. The inset is an image of the microbubble in contact with the coupling taper.

recently reveal to be ideal for optofluidics-based applications [200, 201]. The microbubbles are fabricated from slightly pressurized silica capillaries using a modified fusion splicer, where the electrodes are placed in a U-shaped holder that can rotate by 360°. One end of the capillary is sealed with optical glue, whereas the other one is connected to a homemade pressurization system. The capillary is then filled with an inert gas and placed between the electrodes. Uniform heating of the capillary is obtained by arc discharge and simultaneous rotation of the U-shaped holder around the capillary [61]. Figure 5.6 shows a WGM resonance excited in a silica microbubble with external diameter of a 490 μm.

Q factor is in excess of 10^7 and the contrast K is about 15%. The inset of Fig.5.6 is an image of the microbubble placed in contact with the coupling taper.

5.3.4 Conclusion

In conclusions we have proposed a new method based on fiber LPGs for improved robustness of fiber coupling to silica micro-resonators. The idea is to excite highorder LP fiber modes through an LPG. The LPG is followed by an adiabatic taper that reduces the cladding mode size and allows the evanescent part of the field to overlap with the WGM of the micro-resonators. We demonstrated efficient coupling to high-Q silica microsphere and microbubble resonators detecting the transmission dip corresponding to an excited resonance. The taper is about one order of magnitude thicker than the standard fiber taper used for coupling light to WGM resonators, and therefore, this new method offers improved robustness for practical applications. Additionally, with this method, by cascading LPGs with different periods, a wavelength selective addressing of different silica micro-resonators along the same fiber would be possible.

5.4 Article 5: Quasi-distributed and wavelength selective addressing of optical micro-resonators based on long period fiber gratings

5.4.1 Abstract

A novel all-in-fiber method for coupling light to high-Q silica whispering gallery mode (WGM) optical micro-resonators is presented, which is based on a pair of long period fiber gratings (LPGs) written in the same silica fiber, along with a thick fiber taper (15–18 μm in waist) in between the LPGs. The proposed coupling structure is robust and can be replicated many times

along the same fiber simply cascading LPGs with different bands. Typical Q-factors of the order of 10^8 and total coupling efficiency up to 60% were measured collecting the resonances of microspheres or microbubbles at the fiber end. This approach uniquely allows quasi-distributed and wavelength selective addressing of different micro-resonators along the same fiber.

5.4.2 Introduction

Real-time physical, chemical and biological sensing are critical in many applications, such as environmental pollution measurement, health care, gas detection and industrial processes control. Major requirements are measurements at multiple locations, large spatial area coverage, operation capability in harsh environments and low cost. Particularly, there is a critical need for technologies that can provide distributed or quasi-distributed measurement at multiple points. Fiber optics sensors are ideal transducers for applications requiring devices that are durable, stable and insensitive to external perturbations [202]. The challenging goal of this work was to find an all-in-fiber coupling method to implement a quasi-distributed interrogation of whispering gallery mode (WGM) microoptical resonators. In fact, high quality factor (Q) WGM micro-resonators are known to exhibit unique properties for sensing by using different geometries [42]. Light can be stored for a long time in small volumes thus increasing tremendously the probability to interact with the external environment during the numerous roundtrips at the resonator surface. Any small change in size and/or refractive index at the cavity surface induces, through the interaction with the evanescent part of the WGM field, either a change in the resonator Q-factor or a shift in the resonance frequency [203]. As an example, highly sensitive biosensors able to detect single nanoparticles or molecules have been demonstrated [31]. However, in case of multiple sensing a critical point for this type of micro-optical transducers is

the development of a coupling system able to interrogate a series of cavities along the same fiber, in order to implement a quasi-distributed sensor. So far, none of the several methods [187] that have been developed to efficiently couple light to WGM micro-resonators simply fulfils this key request. With one or more standard fiber tapers [190], for instance, it is impossible to selectively excite micro-resonators and it is extremely critical to distinguish (a priori) the resonances of each cavity by collecting the signal at the fiber end. Additionally, standard fiber tapers used for coupling are very thin, down to 1 μm in diameter, and therefore they are very fragile. In previous works [204, 205], we proposed a configuration for coupling light to a high-Q silica WGM resonator, which is based on a long period grating (LPG) written in silica fiber followed by a thick fiber taper. The LPG allowed wavelength selective excitation of highorder cladding modes, so that thicker and more robust taper (with waist diameters in excess of 15 μm, which are easy to fabricate and do not degrade in time) could be used for coupling light from the fiber to the WGM resonator. This configuration is more robust than the standard fiber taper coupler but it does not allow interrogating more spheres coupled to the same fiber by monitoring the transmitted light. The only possibility of multiplexing consists of collecting the scattered light from each resonator and eventually sent the signal to a photodetector [205], which is a quite complicated approach. Conversely, the transmitted light cannot be used for multiplexing. In fact, in a first configuration, if the fiber jacket is kept after the taper, it cuts off the modulated cladding mode, whereas, in a second case, if the jacket is removed, then the cladding mode excited by the LPG would be coupled to all the resonators following the LPG. Herein, to overcome these limitations, a new all-in-fiber coupling system for quasi-distributed and wavelength selective addressing of several WGM resonators is proposed. This approach consists of replicating many times the same structure that is based on a pair of identical LPGs with a fiber taper in between.

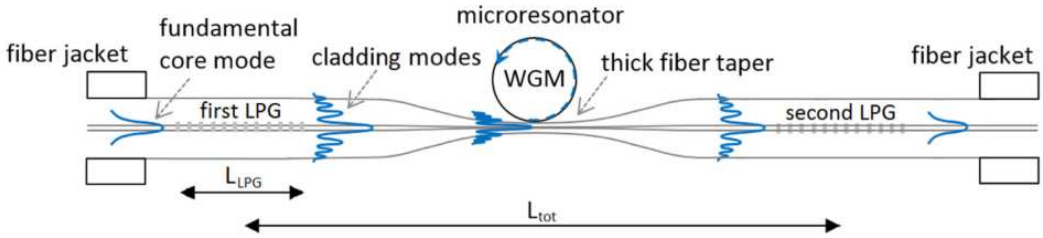

Figure 5.7: Schematic representation of the fiber based coupling unit consisting of a pair of LPGs and a taper in between.

Compared to the previous approaches [190, 204], the presence of the second LPG allows coupling of the light back into the core and therefore all the necessary information is contained into the core mode, which is transmitted up to the end of the fiber and collected by a single photodetector. By fabricating pairs of identical LPGs operating in different wavelength bands, it is possible to achieve multiple selective coupling and interrogation (or selective addressing) of spatially quasi-distributed micro-resonators by using the same optical link.

5.4.3 Fabrication and experimental setup

A schematic representation of the coupling mechanism to WGM resonators by using the proposed approach is depicted in Fig. 5.7.

First, adiabatic fiber tapers were fabricated by a heating and pulling procedure [110] in a single-mode boron-germanium co-doped optical fibers (Fibercore PS1250/1500) with core and cladding diameters of 6.9 μm and 124.6 μm, respectively. Tapers with a diameter of 15–18 μm were fabricated allowing the transmission of the selected cladding mode. For efficient coupling of these cladding modes to silica WGM resonators, partial tapering of the fiber is necessary in order to reduce the optical field size and increase its external evanescent portion [204]. However, as already pointed out, the tapered region is one order of magnitude thicker than that of the standard

tapers (1–2 μm), and therefore it is much more robust for practical applications. After the taper fabrication, the coupling unit was completed by fabricating the pair of identical LPGs on both sides of the tapered fiber (see Fig. 5.7). An LPG is characterized by a series of periodic refractive index changes in the core of a single-mode optical fiber, with a grating period Λ ranging from 100 μm to 600 μm. In such structure, the coupling occurs between the fundamental core mode (LP_{01}) and co-propagating azimuthally symmetric cladding modes (LP_{0m}, m$\geq$2), each of which generates an attenuation dip in the fiber transmission spectrum [216]. The gratings were inscribed with a point-by-point technique by using a KrF excimer laser (Lambda Physic COMPex 110) [195]. The first LPG selectively couples the light from the core mode to a specific cladding mode, which evanescently excites the resonator WGMs in the tapered section. The resonator is placed in contact with the taper for improved stability. The second LPG couples the light back into the fiber core, thus all the information is contained in the core. This structure can be replicated many times on the same fiber allowing wavelength selective addressing of more resonators. Two different pairs of LPGs with Λ of 340 μm and a length L_{0m} of 17 mm (for the first coupling unit) and with Λ of 365 μm and a L_{LPG} of 21.9 mm (for the second coupling unit) were fabricated.

For proving the effectiveness and feasibility of the proposed system, two types of resonators, silica microspheres [110] and microbubbles [61] were fabricated in our labs. Diameters ranging from 260 μm to 290 μm for microspheres and from 380 μm to 500 μm for microbubbles were selected. In both cases, the resonator size was large enough so that the free spectral range (FSR) was significantly smaller than the LPGs bandwidth [204]. The experimental setup used for the characterization of the transmission spectrum consists of two fiber pigtailed tunable external cavity lasers (Anritsu Tunics Plus, linewidth 300 KHz), covering the bandwidth from 1390 nm to 1640

nm. An optical spectrum analyzer (OSA– Ando AQ6317B) detects the signal. The coupling approach was tested by means of the same laser sources, that can be finely and continuously swept in wavelength within few GHz, and a single photodetector connected to an oscilloscope. The experiments were performed in air but, because of the improved taper robustness, we plan to design a similar coupling unit to operate in an aqueous environment.

5.4.4 Results and discussion

The spectra of the two single LPGs (before making the second identical ones to form the two pairs) were first recorded and are shown in Fig.5.8 merged together (red line).

The two attenuation bands at wavelengths of 1518.99 nm and 1613.31 nm represent the coupling with the same LP_{07} cladding mode achieved with different Λ, 340 μm and 365 μm, respectively. The band depth exceeds 15 dB for both LPGs because high coupling efficiencies with the cladding modes were targeted. Figure 5.8 also details the spectrum measured by putting in series the two coupling units, i.e. the two pairs of LPGs with the respective tapers (blue line). Typical interference patterns can be observed as, for each LPG pair, the system acts as a Mach-Zehnder interferometer (MZI) [174]. The maximum modulation amplitudes (best MZI contrast) corresponding to the 3 dB attenuation wavelengths of the single LPGs (see the dashed grey line in Fig. 5.8) appear as two fringe patterned sidebands symmetrically placed on both sides of the single LPG minimum transmission wavelengths (1518.99 nm and 1613.31 nm). At these wavelengths, instead, a reduced modulation amplitude and a rather high transmission can be observed, showing that the light is effectively coupled back into the core mode by the second LPG after the tapered sections. Minimum insertion losses are about 1 dB at 1518.99 nm and about 2 dB at 1613.31 nm. In addition, Fig. 5.8 shows that the period

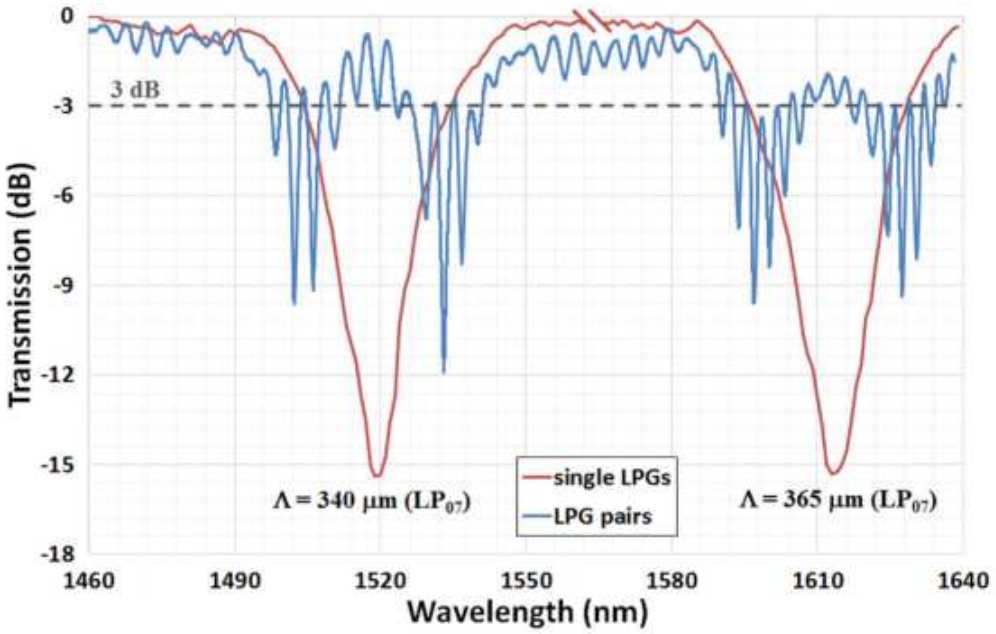

Figure 5.8: Transmission spectra of the two single LPGs (solid red line) showing minimum transmission at the wavelengths of 1518.99 nm ($\Lambda = 340$ μm) and 1613.31 nm ($\Lambda = 365$ μm), respectively, and of the two LPG pairs together (solid blue line). The grey line crosses the -3 dB value of the attenuation dips of the single LPG and corresponds to the maximum LPG based MZI contrast.

of the interference fringes related to the second coupling unit ($\Lambda = 365$ μm) is smaller than that of the first one ($\Lambda = 340$ μm). This can be ascribed to the greater physical distance L_{tot} of the two LPGs composing the second coupling unit (roughly 5.2 cm) with respect to the first one (roughly 4.4 cm). As a number of external perturbations, such as fiber bending, temperature and refractive index, affects the transmission spectra of the coupling unit, an initial calibration of the system acquiring these spectra (in order to assess the operating central wavelength) will be needed for optimal performances. Each coupling unit was individually tested and high-Q WGM resonances in both microspheres and microbubbles were effectively excited. The resonators were placed in contact with the tapers. Phase-matching conditions between the LPG cladding modes and the WGMs were fulfilled thanks to the radial and azimuthal high-order modes of spherical WGM resonators [205]. The transmission dips were fitted by a Lorentzian function obtaining typical Q-factor values close to 10^8 for both types of micro-resonators. Figure 5.9 shows the WGM resonances excited both in microspheres (Fig. 5.9(a)) and microbubbles (Fig. 5.9(b)) together with a 3D sketch of the coupling system for both microcavities.

The main graphs show the maximum Q-factors achieved for each type of resonators, while the insets show the maximum contrast achieved with the corresponding microcavity. By optimizing the state of polarization of the input light (coupling units are polarization insensitive [204] but the WGM distribution in the resonator depends on the polarization) and the resonator position along the taper, we observed maximum coupling efficiency (or resonance contrast) of about 50%–60%. In our case, the system acts as a multimode waveguide coupler (not all the lunched power is in the selected cladding mode) and thus the contrast is limited, since it is not possible to reach the condition of single-mode coupler [207]. The coupling efficiency has been significantly improved as compared to our previous work [204]. The reason

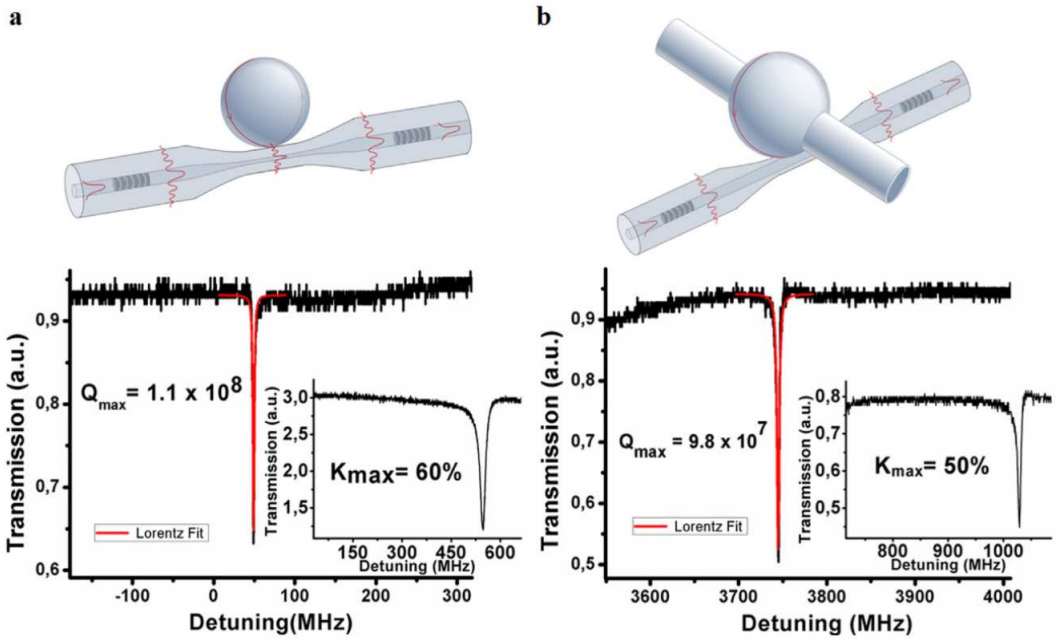

Figure 5.9: Sketch of the LPG pair-based coupling units exciting WGMs in both microspheres (a) and microbubbles (b), along with an example of typical WGM resonances obtained for both micro-cavities. The two insets show the maximum coupling efficiency obtained for both types of micro-cavities.

could be related to the fact that the cladding mode is coupled back in the core right after interacting with the resonator, and once in the core there are no additional losses. In the previous configuration, the cladding mode was left propagating at the fiber-air interface along the whole remaining part of the fiber, possibly introducing additional losses in the modulated signal (and thus reducing the resonance contrast). A wavelength range up to about 15 nm for each coupling unit (from 1510 nm to 1525 nm for the first LPG pair and from 1605 nm to 1620 nm for the second one) was considered for efficient coupling, as within this range up to 90% of the power is coupled from the fundamental mode to the LP_{07} cladding mode (see single LPG transmission spectra in Fig. 5.8). In order to confirm that the light can be selectively coupled in the micro-cavities, the laser source was also tuned outside the attenuation band of the LPGs, for instance from 1545 nm to 1585 nm (see Fig. 5.8), and no significant coupling was observed as expected. After this individual characterization, the system composed by the two in-series coupling units was analyzed. Figure 5.10(a) show the resonances obtained by scanning (about 2 GHz) around the LPG central wavelengths (1518.99 nm for the first coupling unit and 1613.31 nm for the second one), when both resonators were in contact with their respective tapers (as sketched on the top of Fig. 5.10(a)).

Typical Q-factor values comparable to those previously mentioned were observed. The selectivity test was carried out by alternatively de-coupling one of the resonator and by looking at the transmission spectrum of the other micro-cavity, as shown in Fig. 5.10(b) (first resonator in contact, second resonator detached, as sketched on the top of the figure) and in Fig. 5.10(c) (second resonator in contact, first resonator detached). In particular, several measurements were performed varying the taper coupling position along the azimuthal axis of the resonators. It was found that each resonator was independently excited and the resonances of one resonator were not present in

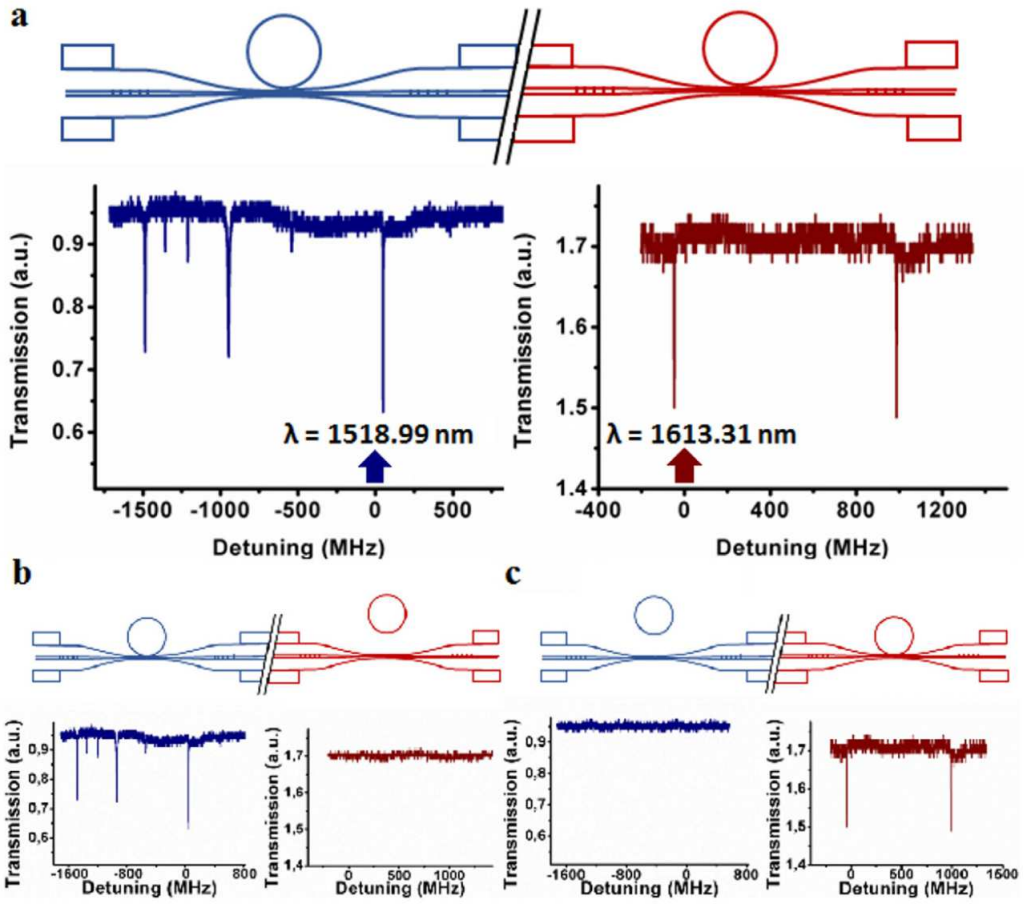

Figure 5.10: Sketch of two in series coupling units with both resonators (circle) coupled to each tapered section of the fiber and corresponding resonances obtained by scanning the laser source around the LPGs central wavelengths (a). First resonator in contact, second not (b). Second resonator in contact, first not (c). The resonances of each coupling unit remain unchanged proving they are independently excited without cross-talk.

the 'wavelength range' of the other one. Therefore, the proposed coupling system can be used for quasi-distributed sensing. In our case, considering a wavelength range of 50 nm 'reserved' for each LPG pair (a range larger than the 3 dB bandwidth for each LPG can be considered in order to safely avoid any cross-talk) and the source bandwidth of 250 nm, up to 5 coupling units could be fabricated along the same fiber, leading to possible multiplexing of up to 5 different micro-cavities selectively coupled and independently interrogated. Considering that typical insertion losses of the single coupling unit are 2 dB, total losses not exceeding 10 dB for a set of 5 units can be assumed.

5.4.5 Conclusion

An independent and selective coupling with high-Q WGM micro-resonators was demonstrated based on a new all-in-fiber method consisting of a pair of long period gratings with a fiber taper in between. The first LPG is used for the selective excitation of cladding modes, whereas the taper allows evanescent coupling from the fiber to the resonator WGM. The second LPG couples the light modulated by the resonator back into the core. The proposed structure is robust and easy handled thanks to the use of a thick taper (15–18 μm waist), and allows collecting light just from the fiber core thanks to the second LPG. The structure can be replicated many times along the same fiber depending on the source bandwidth and all the information can be independently collected at the end of the fiber by using a single detector. Q-factor of the order of 10^8 and total coupling efficiency up to 60% were experimentally achieved by using silica microspheres and microbubbles. To the best of our knowledge, this approach allows for the first time a quasi-distributed and wavelength selective addressing of different WGM micro-optical resonators along the same fiber with an almost-zero resonance cross-talk, thus improving the perspective of optical fiber-based sensing and biosensing. In addition,

the proposed system results to be a very promising platform for multiplexing hollow WGM microstructures, like microbubble resonators, which are intrinsically suited for integrated microfluidics [208].

Chapter 6

Conclusions

In this thesis I have presented my studies on the nonlinear optical effects (NLE) in whispering gallery mode microresonators and the results of the work that has been done for improving the sensing applicability and reliability of this kind of cavities. The silica WGMRs are produced in our labs by using arc discharge melting methods and they are efficiently excited by using home made tapered fibers.

In microspheres and microbubble we have started observing a variety of nonlinear processes related to the third-order susceptibility such as SRS and FWM, in agreement with the theory of Bloembergen and Shen [P2, P8]. In particular, we got anti-Stokes frequency comb in the microbubble resonators with a repetition rate that is not an integer number of the FSR, indicating the interaction of family modes with the same azimuthal but different polar number [P5]. It is worth to notice that the hyper-parametric oscillations in these cavities results to be much broader than the cases published up to now. The first results can pave the way for the application of NLE in WGMs resonators for molecular spectroscopy and active sensing. After that we have illustrated the potential of WGMRs as frequency converters and tunable sources. Third harmonic generation and third order sum frequency generation were exploited by controlling the cavity mode dispersion and the

phase matching of the involved modes [P1]. For microspheres with different dimensions, simulations and experiments have been done on visible light generation starting from CW IR excitation in the erbium-band gain of an EDFA. We got a conversion efficiency of 10^{-5}, six orders of magnitude over that reported in other ring resonators.

WGM microresonator keep demonstrating their potential for easily studying and exploiting non-linear optical effects. In the last years a lot of work has been done on frequency comb (FC) generation and Brillouin emission. These two different phenomena can find potential applications for producing efficient compact highly coherent laser and low phase noise microwave and radio frequency generators for applications to telecommunications and other domains. For the future it would be worth to deeply investigate how to broaden the wavelength window for generating hyperparametric oscillation by manipulating material and geometric dispersion in micro-bubble resonators. Besides, a further investigation that could be of particular interest is the study of how these kind of cavities can enhance Brillouin scatterning efficiency simultaneously with SRS and FWM emissions.

The final section gives an overview of a new coupling system that have been developed exploiting long period gratings. This all-in-fiber method consists of a pair of LPGs, for the excitation and the collection of the cladding modes, and a partial taper in between the two LPGS, for the evanescent coupling of the WGMs. An independent and selective coupling was demostrated for the first time allowing a quasi-distributed and wavelength selective addressing of WGMRs along the same fiber. These results definitely improve the perspective of fiber-based sensing [P4, P6]. Up to now LPG fiber-based sensing has demonstrated intrinsic capabilities such as insensitivity to electromagnetic radiation, lightweight, small size, great sensitivity and good resolution. Our coupling technique opens the way to various new sensing experiments where one would work with the WGMR multiplexing to improve

the performances of multiple single-point biosensors and even environmental control devices (gas control, corrosion control and so on). It would be interesting to compare the results that could be got using an LPG-WGMR system with those of the conventional quasi-distributed LPG fiber configurations.

Our works have investigated also the feasibility of biosensors using silica WGMRs underlining the importance of the functionalization layer [P10], the possibility of increasing the sensitivity using a silicon coating [P3] and enhancing the performances, without loss of robustness of the system, by means of a microbubble resonator [P9].

In conclusion microresonators have great potential to becomes the essential components for ultra-compact linear and nonlinear photonic devices.

Complete list of publications

Author's contribution

In the papers P1,P2,P4,P5,P6 and P8 listed below I am the first author and I have been in charge of all the experimental part (except in paper P6 where Dr. F. Chiavaioli equally contributed). I have also contributed to the data analysis and to the preparation of the manuscripts. In all the other pubblications I have contributed in writing and the co-operation with co-authors has been significant.

ISI Journal articles

P1 - D. Farnesi, A.Barucci, G. Righini, S. Berneschi, S. Soria, and G. Nunzi Conti, "Optical Frequency Conversion in Silica-Whispering-Gallery-Mode Microspherical Resonators" Physics Review Letters 112, 093901 (2014).

P2 - D. Farnesi, Franco Cosi, Cosimo Trono, Giancarlo C. Righini, Gualtiero Nunzi Conti, and Silvia Soria, "Stimulated anti-Stokes Raman scattering resonantly enhanced in silica microspheres" Optics Letters, Vol. 39, Issue 20, pp. 5993-5996 (2014).

P3 - D. Ristic, A. Chiappini, M. Mazzola, D. Farnesi, G. Nunzi-Conti, G.C. Righini, P. Féron, G. Cibiel, M. Ferrari, M. Ivanda, "Whispering gallery

mode profiles in a coated microsphere", The European Physical Journal Special Topics 223, 1959 (2014).

P4 - D. Farnesi, F. Chiavaioli, G. C. Righini, S. Soria, C. Trono, P. Jorge, and G. Nunzi Conti, "Long period grating-based fiber coupler to whispering gallery mode resonators" Optics Letters, Vol. 39, Issue 22, pp. 6525-6528 (2014)

P5 - D. Farnesi, A.Barucci, G.C.Righini, G. Nunzi Conti and Silvia Soria, Optics Letters, "Generation of hyper-parametric oscillations in silica microbubbles" Vol. 40, No.19 (2015).

P6 - D. Farnesi, F. Chiavaioli, F. Baldini, G. C. Righini, S. Soria, C. Trono, and G. Nunzi Conti, "Quasi-distributed and wavelength selective addressing of optical micro-resonators based on long period fiber gratings" Optics Express, Vol. 23, N.16 (2015).

P7 - A. Cosci, F. Quercioli, D. Farnesi, S. Berneschi, A. Giannetti, F. Cosi, A. Barucci, G. Nunzi Conti, and S. Pelli, G. Righini , "Confocal refectance microscopy for determination of microbubble resonator", Opt. Express 23, 16693 (2015).

P8 - D. Farnesi, S. Berneschi, F.Cosi, G.C.Righini, S. Soria and G. Nunzi Conti, "Stimulated Stokes and Antistokes Raman Scattering in microspherical whispering gallery mode resonators" J. Vis. Exp., Issue 110 (2016); doi: 10.3791/53938.

P9 - A. Barucci, S. Berneschi, A. Giannetti, F. Baldini, A. Cosci, S. Pelli, D. Farnesi, G. C. Righini ,S. Soria and G. Nunzi Conti, "Optical Microbubble Resonators with High Refractive Index Inner Coating for Bio-Sensing Applications An Analytical Approach", Sensors 16, 1992 (2016).

P10 - C. Pastells, M.Pilar Marco , D. Merinoc, P. Loza-Alvarez, L. Pasquardini, L. Lunelli, C. Pederzolli, N. Daldosso, D. Farnesi, S. Berneschi , G. C. Righini, F. Quercioli, Gualtiero Nunzi Conti, Silvia Soria, "Two photon versus one photon fluorescence excitation in whispering gallery mode microresonators" Journal of Luminescence 170 860–865 (2016)

P11 - A. Cosci, F. Quercioli, D. Farnesi, S. Berneschi, A. Giannetti, F. Cosi, A. Barucci, G. Nunzi Conti, and S. Pelli, G. Righini, "Resonance Frequency of Optical Microbubble Resonators Direct Measurements and Mitigation of Fluctuations", Sensors 16, 1405 (2016).

Conference proceedings

1. D. Farnesi, A. Barucci, G. C. Righini, G. Nunzi Conti, S. Soria, "Nonlinear effects in ultrahigh Q optical resonators", Photonics North (PN), 2016, 10.1109/PN.2016.7537945 (2016)

2. D. Farnesi, A. Barucci, G. Righini, G. Nunzi Conti, and S. Soria, "Nonlinear Microcavities: from rainbow lasers to frequency Combs" 2016 Photonics and Fiber Technology Congress (ACOFT, BGPP, NP) paper ATh3C.1, invited paper, OSA (2016)

3. D. Farnesi, F. Chiavaioli, F. Baldini, F. Cosi, G.C. Righini, S. Soria, C. Trono, G. Nunzi Conti, "Long period gratings based frequency selective interrogation of micro-resonators along the same fiber", SPIE LASE, 972703-972703-6; 2016 doi:10.1117/12.2213706

4. S. Berneschi, F. Baldini, A. Barucci, A. Cosci, F. Cosi, D. Farnesi, G. Nunzi Conti, G.C. Righini, S. Soria, S. Tombelli, C. Trono, S. Pelli, A. Giannetti, "Localized biomolecules immobilization in optical microbubble resonators", SPIE 9727, 972719(2016); doi:10.1117/12.2213683

5. D. Farnesi, A. Barucci, S. Berneschi, F. Cosi, G.C. Righini, G. Nunzi Conti, S. Soria, "Third order nonlinear phenomena in silica solid and hollow whispering gallery mode resonators", SPIE 9727, 97270K-97270K-6 (2016); doi:10.1117/12.2212344

6. D. Farnesi, G. C. Righini, G. Nunzi Conti, F. Quercioli, S. Soria, "Microbubble resonators as enhancement platforms for linear and nonlinear applications", invited paper SPIE 9655, 965527 (2015); doi:10.1117/12.2185830

7. A. Giannetti, A. Barucci, S. Berneschi, A. Cosci, F. Cosi, D. Farnesi G. Nunzi Conti, S. Pelli, S. Soria, S. Tombelli, C. Trono, G. C. Righini, F. Baldini "Optical micro-bubble resonators as promising biosensors", SPIE 9506, 950617 (2015); doi:10.1117/12.2180242

8. C. Pastells, M. Pilar Marco, D. Merino, P. Loza-Alvarez, L. Pasquardini, C. Pederzolli, D. Farnesi, S. Berneschi, G. C. Righini, G. Nunzi Conti, S. Soria Huguet, "Non-linear fluorescence excitation of Rhodamine 6G and TRITC labeled IgG in whispering gallery mode microresonators", SPIE 9343, 93430K (2015); doi:10.1117/12.2079112

9. A. Cosci, F. Quercioli, D. Farnesi, S. Berneschi, A. Giannetti, F. Cosi, A. Barucci, F. Baldini, G. Nunzi Conti, S. Soria, S. Pelli, and G. Righini, "Optical Microbubble Resonator Thickness Measurements by Means of Reflectance Confocal Microscopy", CLEO Europe 2015 paper CHP24 (2015)

10. D. Farnesi, F. Chiavaioli, F. Cosi, G. C. Righini, S. Soria, C. Trono, and G. Nunzi Conti, "Cladding modes fiber coupling to silica microresonators based on long period gratings", SPIE 9343, 934318 (2015); doi:10.1117/12.2080360

11. D. Farnesi, G. C. Righini, A. Barucci, S. Berneschi, F. Chiavaioli, F. Cosi, S. Pelli, S. Soria, C. Trono, D. Ristic, M. Ferrari, and G. Nunzi

Conti, "Coupling light to whispering gallery mode resonators", (Invited Paper) SPIE 9133, 913314 (2014)

12. D. Farnesi, A. Barucci, S. Berneschi, G. C. Righini, S. Soria, and G. Nunzi Conti, "Multicolour emission in silica whispering gallery mode microspherical resonators", (Invited Paper) SPIE 8960 , 896008 (2014).

13. S. Berneschi, F. Baldini, A. Barucci, F. Cosi, D. Farnesi, A. Giannetti, G. Nunzi Conti, S. Pelli, S. Soria, S. Tombelli, C. Trono, G.C. Righini, "Biosensing with microresonators and fibre nanotips" IEEE ICTON 2013, 1-5, DOI: 10.1109/ICTON.2013.6602947 (2013)

14. I.A. Kolmychek, D. A. Kopylov,T.V. Murzina, F. Baldini, S.Berneschi, D. Farnesi, A. Giannetti, S. Tombelli, G. Nunzi Conti, and S. Soria, "Impact of termal oxidation, surface chemistry and porous silicon morphology for sensing applications", SPIE 8627, 86271E (2013)

15. G. Nunzi Conti, F. Baldini, S. Berneschi, D. Farnesi, A. Giannetti, S. Soria, C. Trono, L. Lunelli, L. Pasquardini, C. Pederzolli, "Whispering gallery mode microresonators: Results on aptasensors and on a new sensing approach" (Invited Paper) SPIE 8600, 86001O (2013)

16. D. Farnesi, A. Barucci, S. Berneschi, M. Brenci, F. Cosi, G. Nunzi Conti, S. Pelli , G. C. Righini, and S. Soria, "High Q silica microbubble resonators", SPIE 8264, 826417(2012)

17. Nunzi Conti, G., Barucci, A., Berneschi, S., Brenci, M., Cosi, F., Farnesi, D., Pelli, S., Righini, G.C., Soria, S., "Coupling approaches and new geometries in whispering-gallery-mode resonators", (Invited Paper) SPIE 8236, 82360V (2012).

Bibliography

[1] T. Maiman, "Stimulated optical radiation in ruby," Nature 187, 493– 494 (1960).

[2] A. Javan, W. R. Bennett, and D. R. Herriott, "Population Inversion and Continuous Optical Maser Oscillation in a Gas Discharge Containing a He-Ne Mixture," Phys. Rev. Lett. 6, 106, 1961.

[3] H. Kroemer, "A proposed class of hetero-junction injection lasers," In Proc. IEEE, 51, 1782 – 1783 (1963).

[4] C. K. N. Patel, "Continuous-Wave Laser Action on Vibrational-Rotational Transitions of CO2 ," Phys. Rev. 136, A1187 (1964).

[5] P. P. Sorokin and J. R. Lankard, "Stimulated Emission Observed from an Organic Dye, Chloro-aluminum Phthalocyanine," IBM J. Res. Dev. 10, 162 (1966).

[6] F. P. Schäfer, "Organic Dye Solution Laser," Appl. Phys. Lett. 9, 306 (1966).

[7] N. G. Basov, V. A. Danilychev, Y. Popov, and D. D. Khodkevich, "Laser Operating in the Vacuum Region of the Spectrum by Excitation of Liquid Xenon with an Electron Beam," Zh. Eksp. Fiz. i Tekh. Pis'ma. Red. 12, 473–474 (1970).

[8] P.A. Franken, A.E.Hill,C. Peters,and G.Weinreich "Generation of optical harmonics" Physical Review Letters 7,118 (1961).

[9] M. Bass, P.A. Franken, A.E. Hill,C.W. Peters and G. Weinreich "Optical mixing" Physical Review Letters 8, 18 (1962).

[10] R.W.Terhune, P.D.Maker, and C. M.Savage, "Optical harmonic generation in calcite" Physical Review Letters 10, 404 (1962).

[11] Kenneth E. Niebuhr "Generation of laser axial mode difference frequencies in a nonlinear dielettric", Applied Physics Letters 2, 136 (1963).

[12] S.A. Akhmanov, A.I. Kovrigin, A.S. Piskarskas, V.V. Fadeev, and R.V. Khokhlov "Observation of parametric amplification in the optical range" JETP Lett. 2, 191–193 (1965).

[13] J. A.Giordmaine and R. C. Miller "Tunable coherent parametric oscillation in LiNbO3 at optical frequencies" Physical Review Letters 14, 973 (1965).

[14] C. V. Raman, Indian J. Phys. 2, 387 (1928).

[15] C. V. Raman and U. S. Krishnan, Nature 121, 501 (1928).

[16] G.S. Landsherg, L.I. Mandelstam, "Uber die Lichtzerstreung in Kristallen", Zeitschrift fur Physik 50, 769 (1928).

[17] E. J. Woodbury and W. G.Ng, Proc. IRE 50 (1962) 2367.

[18] G. Eckhardt et al. Phys. Rev. Lett. 9, 455 (1962).

[19] N. Bloembergen "The Stimulated Raman Effect" American Journal of Physics 35, 989 (1967).

[20] W. Kaiser and M. Maier, in Laser Handbook, F. T. Arecchi and E. O. Schulz-Dubois, eds. Vol. 2 (North-Holland, Amsterdam, 1972).

[21] A. Penzkofer et al. "Progress in Quantum Electronics" 6 55-140 (1979).

[22] M. G. Raymer and I. A. Walmsley, "Progress in Optics" vol XXVIII, by E. Wolf (North Holland, Amsterdam, 1990).

[23] C. G. B. Garrett, W. Kaiser, and W. L. Bond "Stimulated Emission into Whispering Modes of Spheres" Physical Review 124, 1807 (1961).

[24] Sir Isaac Newton, Opticks (William Innys, London, 1730).

[25] L. Lorenz, Lysbevægelsen i og uden for en af plane Lysbølger belyst Kugle (Luno, 1890).

[26] G. Mie, "Beitrage zur Optik trüber Medien, speziell kolloïdaler Metallosungen," Ann. Phys. (Leipzig) 25, 337–445 (1908).

[27] P. Debye, "Der lichtdruck auf kugeln von beliebigem material," Annalen der physik 335(11), 57–136 (1909).

[28] H. C. van de Hulst, Light Scattering by Small Particles (Peter Smith Pub Inc, 1982).

[29] P. W. Barber and R. K. Chang, Optical effects associated with small particles (World Scientific, 1988).

[30] C. F. Bohren and D. R. Huffman, Absorption and Scattering of Light by Small Particles (Wiley-VCH, 1998).

[31] F. Vollmer and S. Arnold, "Whispering-gallery-mode biosensing: label-free detection down to single molecules," Nat. Methods 5, 591–596 (2008).

[32] T. J. Kippenberg and K. J. Vahala, "Cavity Opto-Mechanics," Opt. Express 15, 17172-17205(2007).

[33] F. Marquardt, "Optomechanics: Push towards the quantum limit," Nat. Phys. 4,513–514 (2008).

[34] D. W. Vernooy, A. Furusawa, N. P. Georgiades, V. S. Ilchenko, and H. J. Kimble, "Cavity QED with high-Q whispering gallery modes," Phys. Rev. A 57, R2293 (1998).

[35] M. Pöllinger and A. Rauschenbeutel, "All-optical signal processing at ultra-low powers in bottle microresonators using the Kerr effect," Opt. Express 18, 17764– 17775 (2010).

[36] P. Del'Haye, A. Schliesser, O. Arcizet, T. Wilken, R. Holzwarth, and T. J. Kippenberg, "Optical frequency comb generation from a monolithic microresonator," Nature 450, 1214–1217 (2007).

[37] A. A. Savchenkov, A. B. Matsko, V. S. Ilchenko, and L. Maleki, "Optical resonators with ten million finesse," Opt. Express 15, 6768–6773 (2007).

[38] J. Schäfer, J. P. Mondia, R. Sharma, Z. H. Lu, A. S. Susha, A. L. Rogach, and L. J. Wang, "Quantum dot microdrop laser," Nano Lett. 8, 1709–1712 (2008).

[39] R. Sharma, J. P. Mondia, J. Schäfer, Z. H. Lu, and L. J. Wang, "Effect of evaporation on blinking properties of the glycerol microdrop Raman laser," J. Appl. Phys. 105, 113104 (2009).

[40] M. Pelton and Y. Yamamoto, "Ultralow threshold laser using a single quantum dot and a microsphere cavity," Phys. Rev. A 59, 2418 (1999).

[41] V. B. Braginsky, M. L. Gorodetsky, and V. S. Ilchenko, "Quality-Factor and Nonlinear Properties of Optical Whispering Gallery Modes," Phys. Lett. A, vol. 137, pp. 393–397, 1989.

[42] M. R. Foreman, J. D. Swaim, and F. Vollmer, "Whispering gallery mode sensors" Advances in Optics and Photonics Vol. 7, Issue 2, pp. 168-240 (2015).

[43] D. Farnesi , S. Berneschi, F. Cosi, G. C. Righini, S. Soria, G. Nunzi Conti, Stimulated Stokes and Antistokes Raman Scattering in Microspherical Whispering Gallery Mode Resonators. J. Vis. Exp. (110), e53938, doi:10.3791/53938 (2016).

[44] O.Svelto, Principles of lasers ; by David C. Hanna (Plenum Press New York, 1976).

[45] John E. Heebner, PhD Thesis "Nonlinear Optical Whispering Gallery Microresonators for Photonics".

[46] Soria S, Berneschi S, Brenci M, Cosi F, Conti GN, Pelli S, Righini GC., Optical microspherical resonators for biomedical sensing. Sensors (Basel) 11(1):785-805 (2011).

[47] G. C. Righini, Y.Dumeige, P.Feron, M. Ferrari, G. Nunzi Conti, D. Ristic and S.Soria, Whispering gallery mode microresonators: Fundamentals and applications, Rivista del nuovo cimento, Vol. 34, 7(2011).

[48] C. C. Lam, P. T. Leung, and K. Young, J. Opt. Soc. Am. B 9, 1585 (1992).

[49] M. Gorodetsky and V. Ilchenko, Optics Communications 113, 133 (1994).

[50] J Hecht. City of Light: The Story of Fiber Optics. Oxford University Press, 1999.

[51] T Miya, Y Terunuma, T Hosaka, and T Miyashita. Ultimate low-loss singlemode fibre at 1.55 um. Electronics Letters, 15(4):106 108, 1979.

[52] B. E. Little, J. P. Laine, and H. A. Haus. Analytic theory of coupling from tapered fibers and half-blocks into microsphere resonators. Journal of Lightwave Technology, 17(4):704—715, (1999).

[53] S. Lacroix, R. Bourbonnais, F. Gonthier, and J. Bures, "Tapered monomode optical fibers: understanding large power transfer," Appl. Opt. 25, 4421–4425 (1986).

[54] D. T. Cassidy, D. C. Johnson, and K. O. Hill, "Wavelength-dependent transmission of monomode optical fiber tapers," Appl. Opt. 24, 945–950 (1985).

[55] A. Yariv and P. Yeh, Optical Waves in Crystals (WileyInterscience, New York, 1984), pp. 177.

[56] Haus H., Waves and Fields in Optoelectronics (Prentice-Hall) 1984.

[57] Dumeige Y., Trebaol S., Ghis¸a L., Nguyen T. K. N., Tavernier H. and Feron P., J. Opt. Soc. Am. B, 25, 2073(2008).

[58] M. L. Gorodetsky, A. D. Pryamikov, and V. S. Ilchenko, "Rayleigh Scattering in High-Q Microspheres," J. Opt.Soc. Am. B 17, 1051–1057 (2000).

[59] J. E. Heebner and R. W. Boyd, "Enhanced all-optical switching by use of a nonlinear fiber ring resonator," Opt. Lett. 24,847(1999).

[60] F. Vollmer et al., Protein detection by optical shift of a resonant microcavity. Appl. Phys. Lett. 80, 4057–4059 (2002).

[61] S. Berneschi, D. Farnesi, F. Cosi, G. Nunzi Conti, S. Pelli, G. C. Righini, and S. Soria, "High Q silica microbubble resonators fabricated by arc discharge" Opt. Lett. 36, 3521 (2011).

[62] Hanumegowda NM, Stica CJ, Patel BC, White I, Fan X. Refractometric sensors based on microsphere resonators. Appl. Phys. Lett. 87:201107(2005).

[63] Arnold S, Ramjit R, Keng D, Kolchenko V, Teraoka I. Microparticle photophysics illuminates viral bio-sensing. Faraday Discuss. 137,65–83 2008.

[64] Drever R, Hall JL, Kowalski F, Hough J, Ford G, Munley A, Ward H. Laser phase and frequency stabilization using an optical resonator. Appl. Phys. B.31:97–105, 1983.

[65] Teraoka, I.; Arnold, S. Enhancing the sensitivity of a whispering-gallery mode microsphere sensor by a high-refractive-index surface layer. J. Opt. Soc. Am. B, 23, 1434–1441 2006.

[66] D. Ristic et al., "Whispering gallery mode profiles in a coated microsphere" The European Physical Journal Special Topics 223, 1959 (2014).

[67] Li, H.; Guo, Y.; Sun, Y.; Reddy, K.; Fan, X. Analysis of single nanoparticle detection by using 3-dimensionally confined optofluidic ring resonator. Opt. Express, 18, 25081–25088, 2010.

[68] A. Barucci, S. Berneschi, A. Giannetti, F. Baldini, A. Cosci, S. Pelli, D. Farnesi, G. C. Righini ,S. Soria and G. Nunzi Conti, "Optical Microbubble Resonators with High Refractive Index Inner Coating for Bio-Sensing Applications An Analytical Approach" Sensors 16, 1992 (2016).

[69] A. Cosci, F. Quercioli, D. Farnesi, S. Berneschi, A. Giannetti, F. Cosi, A. Barucci, G. Nunzi Conti, and S. Pelli, G. Righini , "Confocal reflectance microscopy for determination of microbubble resonator", Opt. Express 23, 16693 (2015).

[70] A. Cosci et al. "Resonance Frequency of Optical Microbubble Resonators Direct Measurements and Mitigation of Fluctuations", Sensors 16, 1405 (2016).

[71] C. Pastells, M. Pilar , D. Merinoc, P. Loza-Alvarez, L. Pasquardini, L. Lunelli, C. Pederzolli, N. Daldosso, D. Farnesi, S. Berneschi , G. C. Righini, F. Quercioli, G. Nunzi Conti, S. Soria, "Two photon versus one photon fluorescence excitation in whispering gallery mode microresonators" Journal of Luminescence 170 860–865 (2016)

[72] R. Shuker and R. W. Gammon, Phys. Rev. Lett. 25, 222 (1970).

[73] R. J. Glauber "Coherent and Incoherent States of the Radiation Field" Phys. Rev. 131, 2766 (1963).

[74] R. Boyd "Nonlinear Optics" 3rd Edition, Academic Press (2008).

[75] Y. R. Shen "The Principles of Nonlinear Optics" John Wiley and Sons, Inc (2003).

[76] G.P. Agrawal "Nonlinear fiber optics (Fourth Edition)" Academic Press, Elsevier (2007).

[77] R. H. Stolen , J. P. Gordon , Tomlinson W. J., Haus H. A. "Raman response function of silica-core fibers" J. Opt. Soc. Am. B 6, 1159–1166 (1989).

[78] E. Golovchenko, P. V. Mamyshev, A. N. Pilipetskii, and E. M. Dianov, IEEE J. Quantum Electron. 26, 1815 (1990);

[79] E. Golovchenko et al.,J. Opt. Soc. Am. B 8, 1626 (1991).

[80] Coen S., Wardle D. A., Harvey J. D. "Observation of non-phase-matched parametric amplification in resonant nonlinear optics" Phys. Rev. Lett. 89, 273901/1–4 (2002).

[81] K. Hakuta, M. Suzuki, M. Katsuragawa, and J. Z. Li, Phys. Rev. Lett. 79, 209 (1997).

[82] B. Min, T. Kippenberg, and K. Vahala, "A compact fiber-compatible cascaded Raman laser" Opt. Lett., vol. 28, pp. 17–17, 2003.

[83] T. Kippenberg et al., "Theoretical and experimental study of stimulated and cascaded Raman scattering in ultrahigh-Q optical microcavities" IEEE Journal of Selected Topics in Quantum Electronics, Volume: 10, Issue: 5 (2004).

[84] A. A. Savchenkov et al. Tunable optical frequency comb with a crystalline whispering gallery mode resonator. Phys. Rev. Lett. 101, 093902 (2008).

[85] T. Herr, K. Hartinger, J. Riemensberger, C. Y. Wang, E. Gavartin, R. Holzwarth, M. L. Gorodetsky and T. J. Kippenberg, Universal formation dynamics and noise of Kerr-frequency combs in microresonators, Nature Photonics 6, 480–487 (2012).

[86] A. B. Matsko, Savchenkov, A. A., Strekalov, D., Ilchenko, V. S. and Maleki, L. "Optical hyperparametric oscillations in a whispering-gallery-mode resonator: Threshold and phase diffusion." Physical Review A 71, 033804 (2005).

[87] Y. K. Chembo, Strekalov, D. V. and Yu, N. Spectrum and dynamics of optical frequency combs generated with monolithic whispering gallery mode resonators. Physical Review Letters 104, 103902 (2010).

[88] T. Kippenberg, Spillane, S. M. and Vahala, K. J. Kerr-nonlinearity optical parametric oscillation in an ultrahigh-Q toroid microcavity. Physical Review Letters 93, 083904 (2004).

[89] T. Steinmetz et al. Laser frequency combs for astronomical observations. Science 321, 1335–1337 (2008).

[90] S. A. Diddams, L. Hollberg and V. Mbele Molecular fingerprinting with the resolved modes of a femtosecond laser frequency comb. Nature 445, 627–630 (2007).

[91] W. Liang, D. Eliyahu, V. S. Ilchenko, A. A. Savchenkov, A. B. Matsko, D. Seidel and L. Maleki, High spectral purity Kerr frequency comb radio frequency photonic oscillator, Nature Communications 6, 7957(2015).

[92] S. M. Spillane, T. J. Kippenberg, and K. J. Vahala, Nature 415, 621 (2002).

[93] S. M. Chitanvis and C. D. Cantrell, J. Opt. Soc. Am. B 6, 1326 (1989).

[94] M. Tomes and T. Carmon, Phys. Rev. Lett. 102, 113601 (2009).

[95] A. A. Savchenkov, A. B. Matsko, M. Mohageg, and L. Maleki, Opt. Lett. 32, 497 (2007).

[96] I. S. Grudinin, A. B. Matsko, and L. Maleki, Phys. Rev. Lett. 102, 043902 (2009).

[97] W. Liang, V. S. Ilchenko, A. A. Savchenkov, A. B. Matsko, D. Seidel, and L. Maleki, Phys. Rev. Lett. 105, 143903 (2010).

[98] B.B. Li, Y.-F. Xiao, M.-Y. Yan, W. R. Clements, and Q. Gong, Opt. Lett. 38, 1802 (2013).

[99] J.-Z. Zhang and R. K. Chang, J. Opt. Soc. Am. B 6, 151 (1989).

[100] J. B. Snow, S. X. Qian, and R. K. Chang, Opt. Lett. 10,37 (1985).

[101] S. X. Qian and R. K. Chang, Phys. Rev. Lett. 56, 926 (1986).

[102] H. B. Lin and A. J. Campillo. Cw nonlinear optics in droplet microcavities displaying enhanced gain. Physical Review Letters, 73(18):2440—2443, 1994.

[103] J. Cooney and A. Gross, Opt. Lett. 7, 218 (1982).

[104] D. H. Leach, R. K. Chang, and W. P. Acker, Opt. Lett. 17, 387 (1992).

[105] V. E. Roman, J. Popp, M. H. Fields, and W. Kiefer, Appl. Opt. 38, 1418 (1999).

[106] A. B. Matsko, A. A. Savchenkov, and L. Maleki, Opt. Lett. 37, 43 (2012).

[107] W. Liang, A. A. Savchenkov, V. S. Ilchenko, D. Eliyahu, D. Seidel, A. B. Matsko, and L. Maleki, Opt. Lett. 39, 2920 (2014).

[108] A. B. Matsko, A. A. Savchenkov, D. Strekalov, V. S. Ilchenko, and L. Maleki, Phys. Rev. A 71, 033804 (2005).

[109] P. A. Roos, L. S. Meng, S. K. Murphy, and J. L. Carlsten, J. Opt. Soc. Am. B 21, 357 (2004).

[110] M. Brenci, R. Calzolai, F. Cosi, G. N. Conti, S. Pelli, and G. C. Righini, Proc. SPIE 6158, 61580S (2006).

[111] T. Carmon, L. Yang, and K. Vahala, Opt. Express 12, 4742 (2004).

[112] D. Hollenbeck and C. D. Cantrell, J. Opt. Soc. Am. B 19, 2886 (2002).

[113] A. A. Savchenkov, A. B. Matsko, V. S. Ilchenko, I. Solomatine, D. Seidel, and L. Maleki, Phys. Rev. Lett 101, 093902 (2008).

[114] I. H. Agha, Y. Okawachi, M. A. Foster, J. E. Sharping, and A. L. Gaeta, Phys. Rev. A 76, 043837 (2007).

[115] I. H. Agha, Y. Okawachi, and A. L. Gaeta, Opt. Express 17, 16209 (2009).

[116] S. Coen and M. Haelterman, Phys. Rev. Lett. 79, 4139 (1997).

[117] P. DelHaye, Optical frequency comb generation in monolithic resonators,Ph.D. thesis (Ludwig-Maximilians-Universitaet, 2011).

[118] N. Bloembergen and Y. R. Shen, Phys. Rev. Lett 12, 504 (1964).

[119] G. Kozyreff, J. L. Dominguez-Juarez, and J. Martorell, Laser Photon. Rev. 5, 737 (2011).

[120] D. Farnesi, A. Barucci, G. C. Righini, S. Berneschi, S. Soria, and G. Nunzi Conti, Phys. Rev. Lett. 112, 093901 (2014).

[121] W. Liang, A. A. Savchenkov, Z. Xie, J. F. Mac Millan, J. Burkhart, V. S. Ilchenko, C. W. Wong, A. B. Matsko, and L. Maleki, Optica 2,40 (2015).

[122] H. Lee, T. Chen, J. Li, K. Y. Yang, S. Jeon, O. Painter, and K. J. Vahala, Nat. Photonics 6, 369 (2012).

[123] B. J. Eggleton, C. G. Poulton, and R. Pant, Adv. Opt. Photon. 5, 536 (2013).

[124] M. Sumetsky, Opt. Lett. 29, 8 (2004).

[125] M. Sumetsky, Y. Dulashko, and R. S. Windeler, Opt. Lett. 35, 898 (2010).

[126] G. S. Murugan, N. M. Petrovich, Y. Jung, J. S. Wilkinson, and M. N. Zervas, Opt. Express 19, 20773 (2011).

[127] F. Ferdous, H. Miao, D. E. Leaird, K. Srinivasan, J. Wang, L. Chen, L. T. Varghese, and A. M. Weiner, Nat. Photonics 5, 770 (2011).

[128] D. Farnesi, F. Cosi, C. Trono, G. C. Righini, G. Nunzi Conti, and S. Soria, Opt. Lett. 39, 5993 (2014).

[129] A. A. Savchenkov, A. B. Matsko, W. Liang, V. S. Ilchenko, D. Seidel, and L. Maleki, Nat. Photonics 5, 293 (2011).

[130] M. L. Gorodetsky and A. E. Fomin, IEEE J. Sel. Top. Quantum Electron. 12, 33 (2006).

[131] Y. Ooka, Y. Yang, J. Ward, and S. N. Chormaic, "Raman lasing in a hollow, bottle-like microresonator," arXiv: 1505.06414 (2015).

[132] I. S. Grudinin, L. Baumgartel, and N. Yu, Opt. Express 21, 26929 (2013).

[133] A. A. Savchenkov, A. B. Matsko, W. Liang, V. S. Ilchenko, D. Seidel, and L. Maleki, Opt. Express 20, 27290 (2012).

[134] Y. Liu, Y. Xuan, X. Xue, P.-H. Wang, S. Chen, A. J. Metcalf, J. Wang, D. E. Leaird, M. Qi, and A. M. Weiner, Optica 1 , 137 (2014).

[135] M. Li, X. Wu, L. Liu, and L. Xu, Opt. Express 21, 16908 (2013).

[136] W P. Acker, D. H. Leach, and R. K. Chang, "Third-order optical sum-frequency generation in micrometer-sized liquid droplets," Opt. Lett. 14, 402-404 (1989).

[137] D. H. Leach, W P. Acker, and R. K. Chang, "The effect of the phase velocity and spatial overlap of spherical resonances on sum-frequency generation in droplets," Opt. Lett. 15, 894- 896 (1990).

[138] D. H. Leach, R. K. Chang, W P. Acker, and S. C. Hill, "Thirdorder sum-frequency generation in droplets: experimental results," J. Opt. Soc. Am. B 10, 34-45 (1993).

[139] H. Chew, M. Sculley, M. Kerker, P. J. McNulty, and D. D. Cooke, "Raman and fluorescent scattering by molecules embedded in small particles:

results for coherent optical processes," J. Opt. Soc. Am. 68, 1686-1689 (1978).

[140] S. C. Hill, D. H. Leach, and R. K. Chang, J. Opt. Soc. Am. B, 10, 16 (1993).

[141] B H Lee and J N. Bending sensitivity of in-series long-period fiber gratings. Optics Letters, 23(20):1624-1626, 1998.

[142] Y. P. Rakovich and J. F. Donegan, Laser Photonics Rev. 4, 179 (2010).

[143] G. Kozyreff, J. L. Dominguez-Juarez, and J. Martorell, Laser Photonics Rev. 5, 737 (2011).

[144] V. S. Ilchenko, A. A. Savchenkov, A. B. Matsko, and L. Maleki, Phys. Rev. Lett. 92, 043903 (2004).

[145] S. X. Qian and R. K. Chang, Phys. Rev. Lett. 56, 926 (1986).

[146] T. Carmon and K. Vahala, Nat. Phys. 3, 430 (2007).

[147] H.-B. Lin and A. J. Campillo, Phys. Rev. Lett. 73, 2440 (1994).

[148] R. Y. Camacho, Opt. Express 20, 21977 (2012).

[149] A. Chiasera, Y. Dumeige, P. Féron, M. Ferrari, Y. Jestin, G. Nunzi Conti, S. Pelli, S. Soria, and G. C. Righini, Laser Photonics Rev. 4, 457 (2010).

[150] S. Schiller, Appl. Opt. 32, 2181 (1993).

[151] M. L. Gorodestky, A. D. Pryamikov, and V. Ilchenko, J. Opt.Soc. Am. B 17, 1051 (2000).

[152] L. G. Helt, M. Liscidini, and J. E. Sipe, J. Opt. Soc. Am. B 29, 2199 (2012).

[153] J. S. Levy, M. A. Foster, A. L. Gaeta, and M. Lipson, Opt. Express 19, 11415 (2011).

[154] M. Jouravlev, D. R. Mason, and K. S. Kim, Phys. Rev. A 85, 093901-5 013825 (2012).

[155] A. Vengsarkar, P. Lemaire, J. Judkins, V. Bhatia, T. Erdogan, and J. Sipe. Long-period fiber gratings as band-rejection filters. Journal of Lightwave Technology 14(1), 58-65, 1996.

[156] H.S. Kim, S.H. Yun, I.K. Kwang, and B.Y. Kim. All-fiber acousto-optic tunable notch filter with electronically controllable spectral profile. Optics Letters 22(19): 1476-1478, 1997.

[157] G. Meltz, W. W. Morey, and W. H. Glenn, "Formation of Bragg Gratings in Optical Fibers by a Transverse Holographic Method," Optics Letters, 14, pp. 823 825, 1989.

[158] K. O. Hill, B. Malo, K. A. Vineberg, F. Bilodeau, D. C. Johnson, and I. Skinner, "Efficient Mode Conversion in Telecommunication Fiber Using Externally Written Gratings," Electronics Letters, 26, pp. 1270-1272, 1990.

[159] M. Verhaegen, P. Orsini, D. Perron, X. Daxhelet, and S. Lacroix. Long period gratings fabrication techniques. in Applications Of Photonic Technology 4 - Closing The Gap Between Theory, Development, And Application: 156-161, 2000.

[160] O.V. Ivanov. Fabrication of long-period fiber gratings by twisting of a standard single-mode fiber. Optics Letters 30(24), 3290-3292, 2005.

[161] C.Y. Lin and L.A. Wang. Loss-tunable long period fibre grating made from etched corrugation structure. Electronics Letters 35(21), 1872-1873, 1999.

[162] M. Fujimaki, Y. Ohki, J.L. Brebner, and S. Roorda. Fabrication of long-period optical fiber gratings by use of ion implantation. Optics Letters 25(2), 88-89, 2000.

[163] D. Marcuse, Theory of Dielectric Optical Waveguides. New York: Academic, 1991, ch. 2.

[164] D. G. Hall, "Theory of waveguides and devices," in Integrated Optical Circuits and Components, L. D. Hutcheson, ed. (Marcel Dekker, New York, 1987), Secs. 2.4.2 and 2.4.3.

[165] S.W. James and R.P. Tatam. Optical fibre long-period grating sensors: Characteristics and application. Measurement Science and Technology 14(5): R49-R61, 2003.

[166] V. Perlin and H. Winful. Nonlinear pulse switching using long-period fiber gratings. Journal of Lightwave Technology 18(3): 329-333, 2000.

[167] K.S. Chiang, Y.Q. Liu, M.N. Ng, and S.P. Li. Coupling between two parallel long-period fibre gratings. Electronics Letters 36(16): 1408-1409, 2000.

[168] S. James, R. Tatam, A. Twin, R. Bateman, and P. Noonan. Cryogenic temperature response of fibre optic long period gratings. Measurement Science and Technology 14(8): 1409-1411, 2003.

[169] D. Zhao, K. Zhou, X. Chen, L. Zhang, I. Bennion, G. Flockhart, W. MacPherson, J. Barton, and J. Jones. Implementation of vectorial bend sensors using long-period gratings UV-inscribed in special shape fibres. Measurement Science and Technology 15(8): 1647-1650, 2004.

[170] Y. Han, C. Kim, U. Paek, and Y. Chung. Performance enhancement of long period fiber gratings for strain and temperature sensing. IEICE Transactions on Electronics E83C(3): 282-286, 2000.

[171] Y.P. Wang, J.P. Chen, and Y.J. Rao. Torsion characteristics of long-period fiber gratings induced by high-frequency CO2 laser pulses. Journal of the Optical Society of America BOptical Physics 22(6):1167-1172, 2005.

[172] G.M. Rego, J.L. Santos, and H.M. Salgado. Refractive index measurement with long-period gratings arc-induced in pure-silica-core fibres. Optics Communications 259(2): 598-602, 2006.

[173] T. Allsop, D.J. Webb, and I. Bennion. A comparison of the sensing characteristics of long period gratings written in three different types of fiber. Optical Fiber Technology 9(4): 210-223, 2003.

[174] R P Murphy, S W James, and R P Tatam. Multiplexing of fiber-optic longperiod grating-based interferometric sensors. Journal of Lightwave Technology, 25(3),825-829, 2007.

[175] X. Chen, K. Zhou, L. Zhang, and I. Bennion. Optical chemsensors utilizing long-period fiber gratings UV-Inscribed in D-Fiber with enhanced sensitivity through cladding etching. IEEE Photonics Technology Letters 16(5): 1352-1354, 2004.

[176] R. Falciai, A. Mignani, and A. Vannini. Long period gratings as solution concentration sensors. Sensors and Actuators B-Chemical 74(1-3): 74-77, 2001.

[177] X.F. Chen, K.M. Zhou, L. Zhang, and I. Bennion. High sensitivity biosensor based on dualpeak LPG sensitised by light cladding etching. in 17th International Conference On Optical Fibre Sensors, Pts 1 And 2: 383-386, 2005.

[178] J.P. Dankers, J.L. Lenhart, K.S. R., J.H. van Zanten, S.G. Advani, and R. Parnas. Fibre optic flow and and cure sensing for liquid composite molding. Optics Lasers Engineering 35: 91-104, 2001.

[179] S M Topliss, S W James, F Davis, S P J Higson, and R P Tatam. Optical fibre long period grating based selective vapour sensing of volatile organic compounds. Sensors and Actuators B: Chemical, 143(2),629-634, 2010.

[180] M Yan, S Luo, L Zhan, Y Wang, Y Xia, and Z Zhang. Step-changed period chirped long-period fiber gratings fabricated by CO2 laser. Optics Communications, 281(10):2784-2788, 2008.

[181] R Wu, Y Liu, N Chen, F Pang, and T Wang. Fabrication and sensing characteristics of tilted long-period

ber gratings. Proceedings of the SPIE, Advanced Sensor Systems and Applications V,8561:85610G1-85610G7, 2012.

[182] H Ke, K S Chiang, and J H Peng. Analysis of phase-shifted long-period fiber gratings. IEEE Photonics Technology Letters, 10(11),1596-1598, 1998.

[183] B A L Gwandu, X Shu, T D P Allsop, W Zhang, L Zhang, D J Webb, and I Bennion. Simultaneous refractive index and temperature measurement using a cascaded long-period grating device. Proceedings of IEEE Sensors, 3(2),1032-1035, 2002.

[184] Y G Han, B H Lee, W T Han, U C Paek, and Y J Chung. Fibre-optic sensing applications of a pair of long-period fibre gratings. Measurement Science and Technology, 12(7),778-781, 2001.

[185] O Duhem, J F Henninot, and M Douay. Study of in fiber Mach-Zehnder interferometer based on two spaced 3-dB long period gratings surrounded

by a refractive index higher than that of silica. Optics Communications, 180(46),255-262, 2000.

[186] X. Zhang, M. Tomes, and T. Carmon, Opt. Express 19, 9066 (2011).

[187] D. Farnesi, G. C. Righini, A. Barucci, S. Berneschi, F. Chiavaioli, F. Cosi, S. Pelli, S. Soria, C. Trono, D. Ristic, M. Ferrari, and G. Nunzi Conti, Proc. SPIE 9133, 913314 (2014).

[188] Y. Panitchob, G. Senthil Murugan, M. N. Zervas, P. Horak, S. Berneschi, S. Pelli, G. Nunzi Conti, and J. S. Wilkinson, Opt. Express 16, 11066 (2008).

[189] G. Nunzi Conti, S. Berneschi, F. Cosi, S. Pelli, S. Soria, G. C. Righini, M. Dispenza, and A. Secchi, Opt. Express 19, 3651 (2011).

[190] J. C. Knight, G. Cheung, F. Jacques, and T. A. Birks, Opt. Lett. 22, 1129 (1997).

[191] D. Farnesi, A. Barucci, G. C. Righini, S. Berneschi, S. Soria, and G. Nunzi Conti, Phys. Rev. Lett. 112, 093901 (2014).

[192] T. Herr, V. Brasch, J. D. Jost, C. Y. Wang, N. M. Kondratiev, M. L. Gorodetsky, and T. J. Kippenberg, Nat. Photonics 8, 145 (2014).

[193] M. Cai, G. Hunziker, and K. Vahala, IEEE Photon. Tech. 11, 686 (1999).

[194] G. Nunzi Conti, S. Berneschi, A. Barucci, F. Cosi, S. Soria, and C. Trono, Opt. Lett. 37, 2697 (2012).

[195] C. Trono, F. Baldini, M. Brenci, F. Chiavaioli, and M. Mugnaini, Meas. Sci. Technol. 22, 075204 (2011).

[196] A. Luo, K. Gao, F. Liu, R. Qu, and Z. Fang, Opt. Commun. 240, 69 (2004).

[197] M. J. Kim, Y. M. Jung, B. H. Kim, W.-T. Han, and B. H. Lee, Opt. Express 15, 10855 (2007).

[198] LP mode solver, Optiwave Systems Inc.

[199] S. I. Shopova, R. Rajmangal, S. Holler, and S. Arnold, Appl. Phys. Lett. 98, 243104 (2011).

[200] G. Bahl, K. H. Kim, W. Lee, J. Liu, X. G. Fan, and T. Carmon, Nat. Commun. 4, 1994 (2013).

[201] Y. Yang, J. Ward, and S. N. Chormaic, Opt. Express 22, 6881 (2014).

[202] D. A. Krohn, Fiber Optical Sensors: Fundamentals and Applications (Instrument Society of America, Research Triangle Park, 2000).

[203] J. Ward and O. Benson, "WGM microresonators: sensing, lasing and fundamental optics with microspheres," Laser Photonics Rev. 5(4), 553–570 (2011).

[204] D. Farnesi, F. Chiavaioli, G. C. Righini, S. Soria, C. Trono, P. Jorge, and G. N. Conti, "Long period gratingbased fiber coupler to whispering gallery mode resonators," Opt. Lett. 39(22), 6525–6528 (2014).

[205] D. Farnesi, F. Chiavaioli, F. Cosi, G. C. Righini, S. Soria, C. Trono, and G. Nunzi Conti, "Cladding modes fiber coupling to silica micro-resonators based on long period gratings," Proc. SPIE 9343, 934318 (2015).

[206] T. Erdogan, "Fiber grating spectra," J. Lightwave Technol. 15(8), 1277–1294 (1997).

sensors," J. Lightwave Technol. 25(3), 825–829 (2007).

[207] M. L. Gorodetsky and V. S. Ilchenko, "Optical microsphere resonators: optimal coupling to high-Q whisperinggallery modes," J. Opt. Soc. Am. B 16(1), 147–154 (1999).

[208] Y. Sun and X. Fan, "Optical ring resonators for biochemical and chemical sensing," Anal. Bioanal. Chem. 399(1), 205–211 (2011).

[209] Shen Y. R., Bloembergen N. "Theory of stimulated Brillouin and Raman scattering" Phys. Rev. 137, A1787–A1805 (1965).

[210] S. L. McCall, A. F. J. Levi, R. E. Slusher, S. J. Pearton, and R. A. Logan. Whispering gallery mode microdisk lasers. Appl. Phys. Lett., 60:289,291, 1992.

[211] A. J. Campillo, J. D. Eversole, and H. B. Lin. Cavity quantum electrodynamic enhancement of stimulated- emission in microdroplets. Physical Review Letters, 67(4):437—440, 1991.

[212] S. M. Spillane, T. J. Kippenberg and K. J. Vahala, Ultralow-threshold Raman laser using a spherical dielectric microcavity, Nature 415, 621-623 (2002).

[213] P. A. Roos, L. S. Meng, S. K. Murphy, and J. L. Carlsten, Journal of the Optical Society of America B Vol. 21, Issue 2, pp. 357-363 (2004).

[214] Garmire, E., Pandarese, F., Townes, C.H., "Coherently driven molecular vibrations and light modulation" Phys. Rev. Lett. 11, 160 (1963).

[215] E.T. Jaynes and F. W. Cummings, "Comparison of quantum and semiclassical radiation theories with application to the beam maser" IEEE 51, 89 (1963).

[216] T. Erdogan, "Cladding-mode resonances in short- and long-period fiber grating filters," Journal of the Optical Society of America, 14, pp. 1760-1773, 1997.

[217] Vladimir S. Ilchenko, Anatoliy A. Savchenkov, Andrey B. Matsko, and Lute Maleki, Nonlinear Optics and Crystalline Whispering Gallery Mode Cavities, Phys. Rev. Lett. 92, 043903, 2004.